ABSTRACT

Title of Dissertation:	DEVELOPMENT OF GALLIUM NITRIDE AND INDIUM GALLIUM PHOSPHIDE BETAVOLTAIC AND ALPHAVOLTAIC DEVICES FOR CONTINUOUS POWER GENERATION
	Muhammad Raziuddin A. Khan, Doctor of Philosophy, 2023
Dissertation directed by:	Professor Agis Iliadis, Department of Electrical and Computer Engineering

Betavoltaic devices are p-n/p-i-n junction diodes that use the kinetic energy of beta (electron) particles emitted by beta isotopes to create electron-hole pairs and generate electrical power in a similar way as photovoltaic devices use photons energy to generate electrical power. Unlike photovoltaic devices (solar cells), betavoltaic devices can generate electrical power day and night continuously for decades (12 years with ^{3}H (tritium) and 100 years with Ni^{63} (nickel-63)), enabling new capabilities that are not possible with photovoltaic devices or current state of the art chemical batteries. New capabilities include decade-long continuous power for unattended sensor, tagging/tracking devices, and other electronics placed in remote areas (underwater, polar region, space, etc) where change/charge of batteries is highly inconvenient or impossible.

It is expected that wide band gap semiconductors like GaN with an energy gap of 3.4 eV may provide a better performance in terms of output power and stability under beta radiations. However, GaN semiconductor technology is still maturing in terms of growth and fabrication

techniques. InGaP has a moderately wide bandgap of 1.86 eV, but it is well advanced in terms of crystal growth and fabrication techniques. Therefore, our study and research focused on the development (design, fabrication, evaluation) and comparison of a wide band gap (GaN) and a moderately high band gap InGaP, that are considered very promising in betavoltaic applications.

Betavoltaic devices were fabricated on three GaN p-i-n structures with different i-layer thicknesses (600 nm, 700 nm and 1 μm). Two GaN p-i-n structures were grown on top of a sapphire substrate and the third GaN structure was grown on top of a bulk GaN substrate. InGaP devices were fabricated on an InGaP n-i-p structure grown on top of a gallium arsenide (GaAs) substrate. Devices were characterized using current - voltage (IV) measurements in the dark, using a UV light source, and under an electron beam stimulus to mimic their performance under real beta isotopes. Dark IV measurements confirmed good quality diodes with low leakage currents, and IV curves under the UV light (365nm, 3.40 eV) source showed a clear photo-response. IV curves under the electron beam irradiation at 16 KeV (average energy emission of Ni^{63} beta source at 250 mCi/cm^2) resulted in the output powers of 3.01 $\mu W/cm^2$ with an efficiency of 12.63 % for the InGaP device, and 3.32 $\mu W/cm^2$ with an efficiency of 13.2% for the GaN device.

InGaP and GaN devices were also exposed under a 4.5 MeV alpha beam to determine their suitability for an alphavoltaic power source (Direct energy conversion). Both InGaP and GaN devices showed degradation in their MPPs under the direct alpha beam exposure. We also investigated an indirect alphaphotovoltaic (APV) power source by employing ZnS phosphor as an intermediate layer to limit this degradation. This ZnS layer absorbs all the alpha energy and converts it into photons to create EHPs in the semiconductor device to generate electrical output power via indirect energy conversion. We determined that even though APV approach prevented

radiation damage in the semiconductor device but the degradation rate of ZnS phosphor is faster compared to the degradation rate of GaN and InGaP devices under direct alpha beam exposure.

DEVELOPMENT OF GALLIUM NITRIDE AND INDIUM GALLIUM PHOSPHIDE BETAVOLTAIC AND ALPHAVOLTAIC DEVICES FOR CONTINOUS POWER GENERATION

by

Muhammad Raziuddin A. Khan

Dissertation submitted to the Faculty of the Graduate School of the
University of Maryland, College Park, in partial fulfillment
of the requirements for the degree of
Doctor of Philosophy
2023

Advisory Committee:
Professor Agis Iliadis, Chair
Professor Kevin Daniels
Professor Robert Newcomb
Professor Aris Christou
Marc Litz, PhD

Dedication

To my wife Momina

To my Parents Kala Khan and Atisha Begum

To my brothers (5): Zaheer, Rafi, Azhar, Amad and Shiju.

Acknowledgements

First and foremost, I would like to thank the Almighty Allah for the countless blessings, hope, and strength to complete this dissertation work.

This dissertation would not have been possible without the support of many people. Special acknowledge and thanks to ARL folks: Marc Litz for his direction, enthusiasm, knowledge and pushing me to get this done. Randy Tompkins for sharing his knowledge on GaN devices and answering all my questions on device physics. Derek Demare for making the alpha-beam measurements. Stephen Kelley and Mohammad Doumbiya for providing guidance on EBIC measurements.

At UMD, I am thankful to my dissertation advisor Dr. Agis A. Iliadis for his supervision, encouragement, and support over the years. His insight and enjoyment of solid-state physics, which was apparent in his classes, persuaded me to choose a career in the solid-state arena. A special thanks to all my committee members: Robert W. Newcomb, Kevin Daniels, Aris Christou, and Marc Litz for gracefully accepting to be on my dissertation committee.

At the US. Naval Surface Warfare Center Indian Head Division (NSWC-IHD), special thanks to Dr. Kerry Clark and her team for funding this project under NISE 219. My branch (E36) manager, Alexander Sweeney, for allowing me the freedom to work on my dissertation. Oliver Barham for his guidance and motivation. I have learned a lot from Oliver for which I am thankful. I am also thankful to my previous manager, Mike Deeds from the E33 branch, for encouraging me to enroll in the PhD program. To all my colleagues in E36/E33 branch, thank you for all the support, love, and friendship.

I would also like to thank all my family and friends for their unconditional support, love, and encouragement.

Table of Contents

This Table of Contents is automatically generated by MS Word, linked to the Heading formats used within the Chapter text.

List of Tables

List of Figures

List of Abbreviations

GaN	*Gallium nitride*
InGaP	*Indium gallium phosphide*
I-layer	*Intrinsic layer (n minus layer in GaN)*
Bq	*Becquerel*
MEMS	*Microelectromechanical Systems*
Ci	*Curie*
RTG	*Thermoelectric generator*
ZnS	*Zinc sulphide*
EPD	*Electrophoretic deposition*
Am-241	*Americium-241*
^{3}H	*Tritium*
Ni^{63}	*Nickel-63*
Ti	*Titanium*
Al	*Aluminum*
Ni	*Nickel*
Au	*Gold*
V_{oc}	*Open circuit voltage*
I_{sc}	*Short circuit current*
FF	*Fill factor*
MPP	*Maximum power point*
R_s	*Series resistance*
R_{sh}	*Shunt resistance*
V_{th}	*Threshold voltage*
I_s	*Saturation current*
MCNP	*Monte Carlo N-paricle*
TCAD	*Technology computer Aided Design*
MOCVD	*Metal Oxide Chemical Vapor Deposition*
SEM	*Scanning electron microscopy*
TEM	*Transmission electron microscopy*
TDD	*Threading dislocation density*
CTLM	*Circular Transmission Line Method*
IV	*Current -Voltage*
SGS	*SUNY GaN on Sapphire*
AGS	*Adroit GaN on Sapphire*
AGG	*Adroit GaN on GaN*
BSF	*Back Surface Field*
I_{beam}	*Electron beam current*
V_{beam}	*Electron beam voltage*
BOL	*Beginning of life - used to define nuclear power source.*
EOL	*End of life – used to define nuclear power source.*
APV	*Alpha-photovoltaic*

Objectives

1. Compare GaN/GaN, GaN/Sapphire, and InGaP/GaAs betavoltaic devices for their output powers and efficiencies when subjected to monoenergetic electron beam representing average energy of two beta emitters: Nickel-63 and Tritium.
    a. How do betavoltaic devices fabricated on wide bandgap semiconductors like GaN compare with intermediate bandgap semiconductors like InGaP at present?
    b. How does GaN grown on different epi-layers and different i-layer thicknesses effect device output power and efficiency?
2. Examine the performance of GaN and InGaP devices for an alphavoltaic power source
    a. Alpha-isotopes have 1000 x higher energy density than beta-isotopes. Could they be used to generate output power in mW/cm^2 with current state of the art semiconductors?
3. Investigate and demonstrate the alpha-photovoltaic approach using ZnS phosphor as an intermediate layer to prevent radiation damage under direct alpha exposure.
    a. Alpha isotopes cause radiation damage in the semiconductor by displacing atoms in its crystal structure. Could alpha-photovoltaics be used to limit this radiation damage and generate higher output power than betavoltaic devices?

Contributions

1. Developed the design, modelling, and fabrication protocol for optimal betavoltaic performance based on i-layer thickness and minority carrier diffusion length.
2. First determination that InGaP betavoltaics provide better performance than the GaN betavoltaics despite its lower band gap due to better material quality.
3. Proposed and modelled a multijunction structure to increase the charge collection volume in GaN devices for better betavoltaic performance.
4. Developed a process to determine the energy conversion rate of degradation in GaN and InGaP devices for a direct alphavoltaic device. First determination of the damage effect in these materials.
5. Demonstrated an indirect alpha-photovoltaic device using ZnS phosphor intermediate layer.

1. Publications:
    a. Khan, et, al. Design, Fabrication and Characterization of GaN p-i-n Devices for Betavoltaic Power Sources, Solid State Electronics 136 (2017) 24-29.
    b. Khan, et, al. Alpha-photovoltaic Devices for Milli-Watt Applications, IDETC conference proceeding paper, 2022.
    c. Development, Comparison and Evaluation of InGaP and GaN p-i-n devices utilizing Electron Beam for Average Energy Emission for Tritium and Nickel-63 Beta sources – In preparation.

d. Study of Energy Conversion Rate of Degradation in GaN, InGaP and ZnS (phosphor) under the Alpha Beam for an Alphavoltaic/Alpha-photovoltaic Power Source – In preparation.

Chapter 1: Introduction

1.1 Motivation of the Research

Due to the emergence of smart dust devices, the need for micrometer-size batteries has never been greater. Smart dust devices are wireless micro-electro-mechanical systems (MEMS) that can detect everything from light to sound, movement, and vibrations [1]. Designing these small devices is a challenge itself but available technologies, such as etching and deposition, are quite successful in creating microelectronic devices based on semiconductor technology [1]. However, making micrometer-size batteries to power these devices remains a challenge so far due to the low energy density of chemical batteries. Reducing the battery size reduces the capacity of chemical batteries, which hinders this emerging field. Unattended sensors placed in remote locations (underwater, dessert, polar regions), infrastructure embedded sensors, planetary space missions where resupply of power is highly constrained or unavailable, implantable medical devices such as a cardiac pacemaker, all need power sources that are required to last the lifetime of the mission. In addition to long lifetimes, sensing applications also require functionality in extreme (hot/cold/shock) environments. Current energy storage approaches are dominated by chemical battery technologies. Wide availability of chemical components and materials in the commercial marketplace as well as flexibility in manufacturing has supported the extensive utilization of chemical batteries. However, chemical batteries have limitations such as short lifespan (application dependent), low energy density, sensitivity to temperature (chemical reactions are influenced by temperature), material decomposition from surrounding environment, charge leakage, and finite charge cycles for rechargeable

batteries. Therefore, chemical batteries are not well suited for unattended sensors placed in remote locations where long lifetimes and operation in extreme environments is needed, and MEMS technology where micro-size is required.

With their high energy density, long lifetime, and durability in extreme environments, radioisotope-based power sources such as betavoltaics, which convert radioisotope emissions directly into electrical energy, can overcome the limitations of chemical batteries [2, 3]. Figure 1.1 shows the Ragone chart which compares energy density of different batteries and energy storage devices [4]

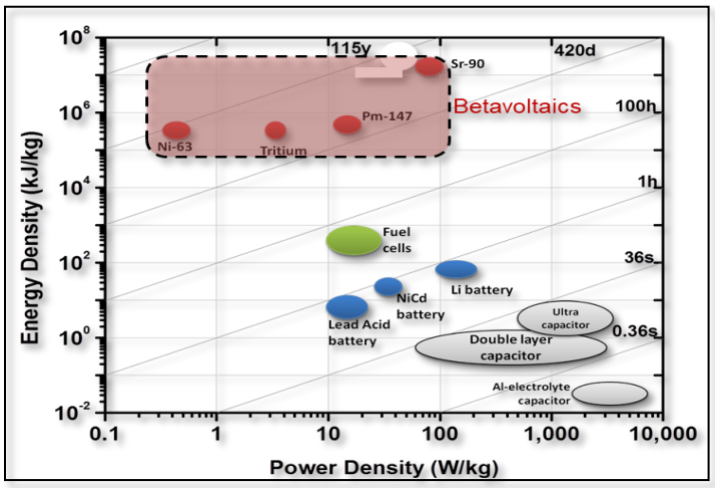

Figure 1.1: Ragone Chart comparing energy density of different battery technologies [4].

The energy density of radioisotope power source is at least 10^3 times greater than the energy density of chemical batteries, and they can produce power for decades to hundreds of years without the need for a recharge [5]. Energy density is the measure of total energy stored in each volume/footprint of a device, and with higher energy dense materials, reducing the footprint of the device does not reduce the battery capacity. On the other hand, a radioisotope power source tends to have low power density compared to other types of batteries [6]. Power density is the rate at which it can output power at a given size. As a result, radioisotope power sources cannot

compete with chemical batteries for applications that require high output power in moderate temperatures [7]. Therefore, the goal of the radioisotope power source is not to replace the chemical batteries but to support them in hybrid configurations and find applications where chemical batteries are not feasible such as unattended sensors, tagging/tracking devices and other miniature low power applications placed in extreme environments.

1.2 Radioisotope Decay and Different Types of Radioisotope Emissions

Radioactive decay is the process in which an unstable nucleus of an atom stabilizes itself by emitting energy in the form of ionizing particles and electromagnetic radiations [8]. All radioisotopes decay at a rate obeying the universal law of radioactivity given by:

$$A = \frac{dN}{dt} = -\lambda N \qquad (1.1)$$

Where A is the total number of nuclei decaying for a given time, also known as radioisotope activity. N is the number of radioactive atoms at time t, and λ is the radioactive decay constant.

The rate at which a radioisotope decays can also be written as:

$$N = N_0 e^{-\lambda t} \qquad (1.2)$$

$$\tau^{1}/_{2} = \frac{\ln(2)}{\lambda} \qquad (1.3)$$

Where N_o is the initial number of radioactive atoms at t = 0. The time at which half of the nuclei decay occurs is referred to as the half-life ($t^{1/2}$) of the material, an important

characteristic of a given radioisotope [8]. The standard international (SI) unit of radioisotope activity is Becquerel (Bq), which stands for 1 decay/second. A commonly used unit is Curie (Ci), which is equal to 3.7×10^{10} Bq [8].

There are three main types of radioisotope decays: Alpha, Beta and Gamma. A brief discussion is provided for each below.

1.2.1 Alpha Decay

Alpha decay is a process where an unstable nucleus changes to another element by shooting out a particle composed of two protons and two neutrons. This nuclear reaction can be represented as:

$$ {}^{A}_{Z}X \rightarrow {}^{A-2}_{Z-2}Y + {}^{4}_{2}He \qquad (1.4) $$

Where ${}^{A}_{Z}X$ is the parent nucleus, A is the total number of nucleons, Z is the total number of protons, ${}^{A-2}_{Z-2}Y$ is the daughter nucleus and ${}^{4}_{2}He$ is the released alpha particle. The alpha particles are typically emitted with a discrete kinetic energy of 4–9 MeV depending on the radionuclide and may be accompanied by electromagnetic radiation as the daughter nucleus transitions from excited states to its ground state [8]. There are many alpha emitters, some are naturally occurring, and others are artificially made in the laboratory. The most common alpha-emitter is americium-241 (Am-241) which is widely used in smoke detectors.

1.2.2 Beta Decay

Beta decay is a process where an unstable nucleus of an atom balances itself by changing a proton into a neutron (or vice versa) inside the nucleus of an atom. Two particles are created during the beta decay process, a beta particle (electron or a

positron) and a chargeless particle (neutrino or an antineutrino) which has a zero to negligible rest mass [8-9]. The process in which a neutron in the nucleus of an unstable atom is converted into a proton is called the β^- (beta minus) decay. During this conversion, an electron and an antineutrino are ejected by the nucleus and its reaction [8-9] is given by:

$$ {}^{A}_{Z}P \rightarrow [{}^{A}_{Z+1}D]^{+} + {}^{0}_{-1}e + \overline{ve} \qquad (1.5) $$

$$ n \rightarrow p + e^{-} + v^{-} \qquad (1.6) $$

Where ${}^{A}P$ is the parent nuclei, ${}^{A}D$ is the daughter nuclei, Z is the number of protons, e^- and $\overline{ve}$ represent the ejected electron and anti-neutrino, respectively. The above reaction shows that a neutron rich radioactive nuclide decays by changing a neutron in the parent (P) nucleus into a proton. The daughter atom denoted by $[{}^{A}_{Z+1}D]^{+}$ gains a proton, initially lacks one orbital electron, and thus it is a singly charged positive ion [8-10].

The β^+ (beta plus) decay, also known as positron emission, is the exact opposite of a β^- decay process. In this process, a proton in the nucleus of an unstable atom is converted into a neutron. This process yields an emission of a positron (e^+) and a particle, neutrino (v). Its reaction is given by:

$$ {}^{A}_{Z}P \rightarrow [{}^{A}_{Z-1}D]^{-} + {}^{0}_{+1}e + ve \qquad (1.7) $$

$$ p \rightarrow n + e^{+} + v \qquad (1.8) $$

Several hundred beta sources are known; some are naturally occurring, and others are artificially made in the laboratory. The energies of the beta sources range from a few KeV to more than 15 MeV, and their half-life from about a second to hundreds of years [11].

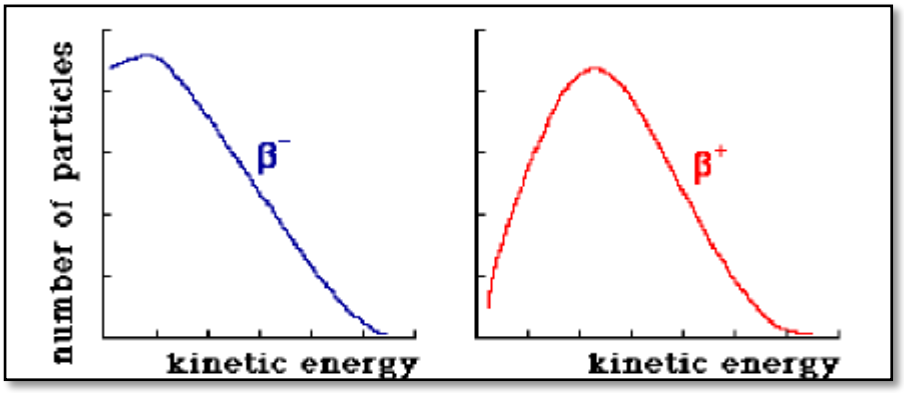

Figure 1.2: Energy spectrum of Beta minus (left) and Beta plus (right) decay.

1.2.3 Gamma Decay

Gamma decay is a process where an unstable nucleus gives away excess energy in the form of electromagnetic radiation. If any radioactive decay results in a daughter nucleus formed in an excited state, then the transition of the nucleus from the excited state to the ground state is followed by the emission of gamma (γ) rays with discrete energies represented as:

$$ {}^{A}_{Z}N * \rightarrow {}^{A}_{Z}N + \gamma \quad (1.9) $$

Here, "$*$" means that the nucleus is in an excited state. Since γ rays have no charge or mass, the nucleus does not change its atomic number (Z) or mass (M). The energy of γ quanta accompanying an alpha decay can reach 0.5 MeV, and the energy of γ quanta accompanying a beta decay can reach 2.5 MeV [8]. Due to their high energy, they are extremely penetrating and are very dangerous to biological life forms [8].

1.3 Different Types of Radioisotope Power Conversion Devices

Radioisotope energy can be converted into electrical energy using different methods, as shown in figure 1.3. A brief description is provided for each method.

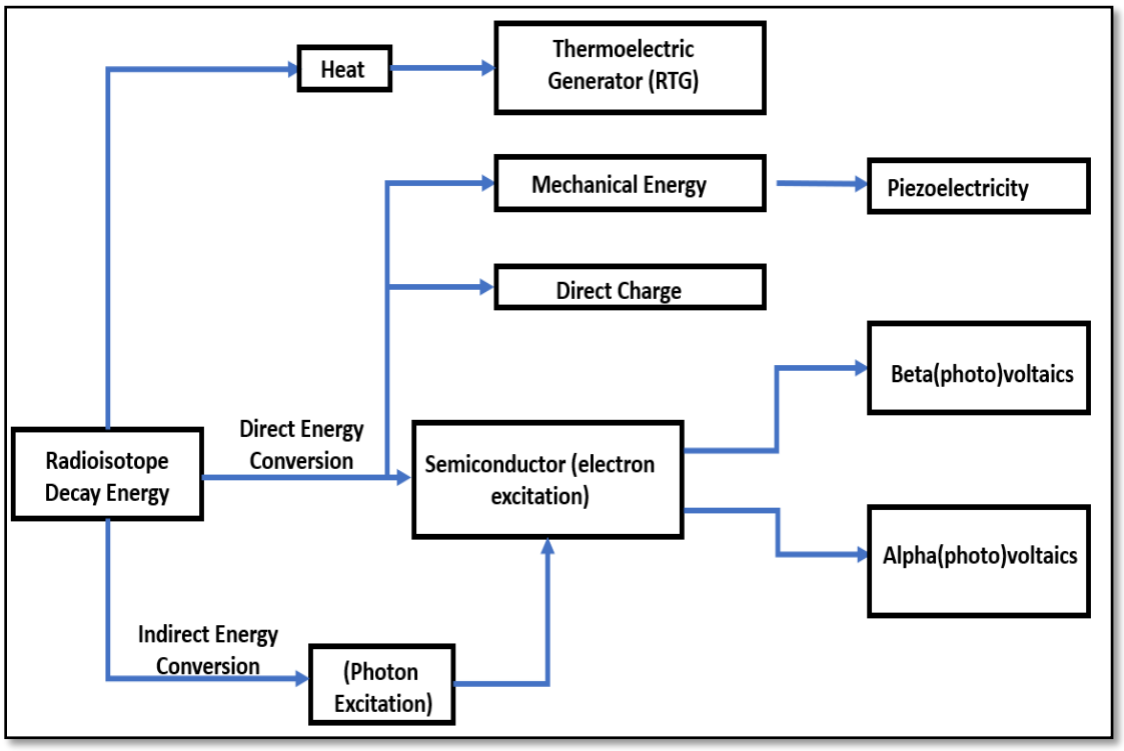

Figure 1.3: Different methods of converting radioisotopes energy into electrical energy.

Thermoelectric generator (RTG) uses decay energy to produce heat first and then transforms the heat into electricity. RTG's can produce power in 100's of Watts (W) and NASA has deployed many RTG's for space mission over the years [13]. The most used radioactive source for this battery type is plutonium-238 (Pu-238) which emits alpha particles with an average energy of 5.6 MeV, along with some amount of gamma rays and neutron radiation [13]. The Multi-Mission Radioisotope Thermoelectric Generator (MMRTG) utilizes Pu-238 and is NASAs most advanced RTG, with a beginning-of-life specific power of 2.8 W/kg and system efficiency of 6% under a 30

V load voltage. The MMRTG emits 110 W electrical power which decreases nominally to 72 W after 17 years (end-of-design-life), along with 2,000 W of thermal power. The Mars Curiosity rover, Mars Perseverance rover, and eventual Dragonfly rotorcraft are all powered by the MMRTG systems [13]. However, this type of power source is not very efficient on the micro-scale level because it is difficult to realize high temperatures on a micro-scale level [8].

A direct charge radioisotope power source generates electricity by collecting charge emitted by radioisotopes in a capacitor geometry to achieve high output voltages [10 – 100 kV). This type of battery provides a very high open circuit voltage (10 – 100 kV), and the efficiency of the battery is comparatively high [7]. For example, 2.6 Ci of Pm-147 in a vacuum generated an open circuit voltage of 60 kV and a short circuit current of 6 nA with an efficiency of 14% [14]. This type of battery has applications for electrostatic motors, but it is not applicable on a micro-scale level.

A piezoelectric energy conversion method uses the electrostatic force developed between the cantilever and a radioisotope to oscillate the cantilever beam to generate power [8]. This self-reciprocating motion can be used as an electromechanical sensor but does not produce sufficient power to power sensors/electronics. For example, 1 mCi of Ni-63 with a Cu cantilever beam (5 cm × 4 mm × 60 μm) generated 0.4 pW of power with an efficiency of 0.0004% [15].

Betavoltaics and alphavoltiacs use the decay energy directly to create electron hole pairs in the semiconductor junction, resulting in electrical energy. They operate on principles similar to those of solar cells [16-17] and differ only in that by using the much more energetic beta/alpha particles instead of photons energy to convert to

electrical energy. Betavoltaic devices utilizing low emitting beta particles energy are preferred over alphavoltaic devices, because high energy alpha particles cause radiation damage in the semiconductor material by displacing atoms in the crystal structure, thus degrading its performance [18-19]. High energy beta sources (> 300 KeV) are also not considered for the same reason. However, alpha isotopes have ~ 1000 X higher energies (4.5 – 5.6 MeV in case of Americium-241) compared to low emitting beta isotopes (~ 5.6 KeV for Tritium) and can be used to produce output power in mW range but require radiation tolerant ultra-wide-bandgap semiconductor junctions, which are not available yet. Therefore, there is a need for alternate approaches to harvest alpha decay energy using existing semiconductor technology. Alpha/Beta-photovoltaics is one such approach which utilizes an intermediate phosphor layer placed between high energy alpha/beta source and a semiconductor junction [20-21]. This phosphor layer acts as a stopping layer to high energy alpha/beta particles to prevent radiation damage in the semiconductor and generates photons which are directed towards the semiconductor device to generate electrical power via indirect energy conversion. Apha/beta-photovoltaics are generally less efficient and less reliable than betavoltaics because the energy conversion in them is a two-step process, and luminescent material itself can degrade over time generating fewer photons to convert to electrical energy. For indirect energy conversion, alpha-photovoltaics are preferred over beta-photovoltaics because high energy alpha particles are easier to shield/package and do not cause any biocompatibility issues, whereas opposite is true for high energy beta particles such as Strontium-90.

Among all the different methods of radioisotope energy conversion, the most

fitting for applications mentioned above are betavoltaic and alphavoltaic power sources. In this dissertation, our discussion is mainly focused on the development of betavotalic devices on GaN (gallium nitride) and InGaP (indium gallium phosphide) semiconductors for betavoltaic power sources. An extension of this work is focused on the examination of the radiation damage in InGaP and GaN devices under the direct alpha beam exposure, as well as demonstration and investigation of an alpha-photovoltaic device using an intermediate ZnS phosphor layer.

1.4 Betavoltaic Cells Brief History and Literature Survey

The first report on betavoltaic (electron – voltaic) effect dates to 1951 by Ehrenberg when he observed that a selenium photocell was sensitive to electrons when bombarded with an electron beam [22]. However, Paul Rapport was the first scientist who suggested the use of a *pn* diode for the conversion of beta radiation into electrical energy in 1953 [23]. A selenium photocell (alloy doped silicon) exposed to a high radiation dose of $^{90}Sr^{90}Y$ resulted in an overall efficiency of 0.4 %. The following year, similar experiments using silicon and germanium were reported [24-25], but the efficiencies were well below 1%. During the period between the 1960s through the 1990s [20-24], numerous laboratories extensively developed and tested betavoltaics, especially Donald W. Douglas laboratories (1968-1974). A device, the Betacell model 400, showed an overall efficiency of approximately 1.7 % by using 77 mCi of promethium-147 (half-life 2.6 years) as a beta emitter. It also found application as a cardiac pacemaker, which was expected to last for 10 years [26-28]. In 1975, the highest overall efficiency (2.2 %) of a betavoltaic device was reported with a silicon n/p diode and promethium dioxide [29-30]. From the investigations during that period,

not only the overall efficiencies of the devices were poor, but researchers also found that beta radiation caused damage to the rectifying junction, thus degrading the performance, and shortening the lifetime of betavoltaic devices fabricated on silicon.

Since the 1990s, researchers have investigated different ways to improve the performance of betavoltaic devices. An increase in the surface area of a rectifying junction was introduced in 2003 [31]. The bulk micro-machined silicon *pn* junction was employed to increase the surface-to-volume ratio by 55% and showed a total efficiency of 0.23% with ^{63}Ni. In order to reduce the radiation damage to the rectifying junction, radiation tolerant materials such as silicon carbide (SiC) and indium gallium phosphide (InGaP) were explored. In 2006, a SiC *p-i-n* junction betavoltaic cell was fabricated using chemical vapor deposition on a low resistivity *n*-type 4H-SiC substrate and tested with phosphorus-33 (^{33}P). It produced a conversion efficiency of ~ 4.5% [32]. The device had an output power density of 2.1 μW/cm^2 and no device degradation effect was observed over 3 months (four half-lives of the source). In the same year, Chandrasekhar investigated a 4H-SiC *pn* structure under a 1 mCi ^{63}Ni source and obtained an overall efficiency of ~6% [33]. However, the output power of the device was low (current density of 16.8 nA/cm^2 and open circuit voltage of 0.72 V) [33]. These results showed that the higher output power obtained in [26] was due to the high energy density of the radioactive source ^{33}P (E_{ave} = 76.9 KeV) compared to ^{63}Ni (E_{ave} = 17.4 KeV) in [33]. Since 2006, several companies have developed betavoltaic batteries, including Qynergy, Widetronix and City Labs [34-36], with City Labs claiming that their Nano-Tritium battery has the license from NRC (nuclear regulatory commission) to sell it to any user.

In recent years, 4H-SiC has become the semiconductor of choice for most researchers followed by GaN and Diamond. The availability of high-quality substrates leading to low leakage current [37], and the fact that SiC is an indirect semiconductor has contributed to its success for betavoltaic energy conversion. In indirect bandgap semiconductors, generated carriers have more time to diffuse into the depletion region, where they can be drifted to contacts for output power. Widetronix has reported on the most efficient (18.8 %) betavoltaic device so far using 4HSiC p-n and 14.97 mCi/cm^2 of titanium tirade (TiH3 x) foil, generating an output power of ~ 157.73 nW/cm^2 [37]. However, the output power of 4H-SiC betavoltaic devices reported in the literature is low for any practical applications.

Diamond with a bandgap of 5.5 eV is of great interest to researchers for betavoltaic and alphavoltaic energy conversion because it is one of the most radiation tolerant materials out there [38]. There are several reports on schottky betavoltaics devices fabricated from diamond [38-39], with limited success so far. It is hard to achieve n-type doping in diamond, therefore it is hard to form a pn/pin junction for a betavoltaic device at this point. Until high-quality diamond films can be successfully grown with both p and n-type dopants, diamond devices for betavoltaics and alphavoltaics are not well suited.

There are several experimental [40-43] and theoretical [44-47] reports on GaN p-i-n/pn and schottky junction betavoltaic devices over the last decade. Some researchers have utilized the monochromatic energy beam from the scanning electron microscopy (SEM) instead of working with real isotopes to evaluate their performance [48-50]. The monochromatic energy beam from the SEM can simulate the energies

and currents found within the beta-decay spectrum for the isotopes. Table 2 lists the output power and efficiency of some of the GaN betavoltaics reported in the literature so far.

Table 1.1: Results reported on GaN betavoltaic devices.

Semiconductor Junction	Isotope Source	Voc (V)	Isc	Power output	Overall Efficiency
GaN (Schottky) [39]	Ni-63 (3mCi/cm^2)	0.1	1.2 nA/cm2	0.12 nW/cm^2	0.32%
GaN (p-n) [40]	Ni-63 (11mCi/cm^2)	0.025	2 nA/cm2	0.05 nW/cm2	1%
GaN (p-i-n) [41]	Ni-63 (11mCi/cm2)	0.47	nA/cm2	2.72 nW/cm2	0.21%
GaN (p-i-n) [42]	Ni-63 (12.5mCi/cm2)	1.65	12 nA/cm2	10.69 nW/cm2	0.82%
GaN (p-i-n) [48]	Monoenergetic electron beam (60.7 µW input power)	2.23	1.86 µA/cm2	2.75 µW/cm2	4.45%
GaN p-i-n [49]	Monoenergetic electron beam (80 µW input power)	1.3	4.03 µA/cm2	2.33 µW/cm2	2.91%
GaN p-i-n [50]	Monoenergetic electron beam (25.5 µW input power)	Not reported	Not reported	255 nW/cm2	1%

The experimental results on GaN betavoltaic devices yielded poor output powers and efficiencies so far. The poor results can be attributed to poor quality of epitaxial GaN films and poor fabrication methods, especially the ohmic contacts to p-GaN layer. Also, all the reports in the literature have been on GaN films grown on top of foreign substrates (the film and the substrate are different materials, which results in formation of misfit dislocations). With the advancements made in growth of GaN semiconductor, GaN films grown on top of GaN substrate are now available, which promises great potential for them to be used for betavoltaic devices compared to SiC betavoltaic devices.

1.5 Scope of this Work

In this study, we developed and evaluated betavotaic devices fabricated from InGaP and GaN semiconductors. Figure 1.4 shows the theoretical efficiency of GaN (26 %) and InGaP (18 %) betavoltaic devices as well as some of the other semiconductors investigated for betavoltaic energy conversion so far [51].

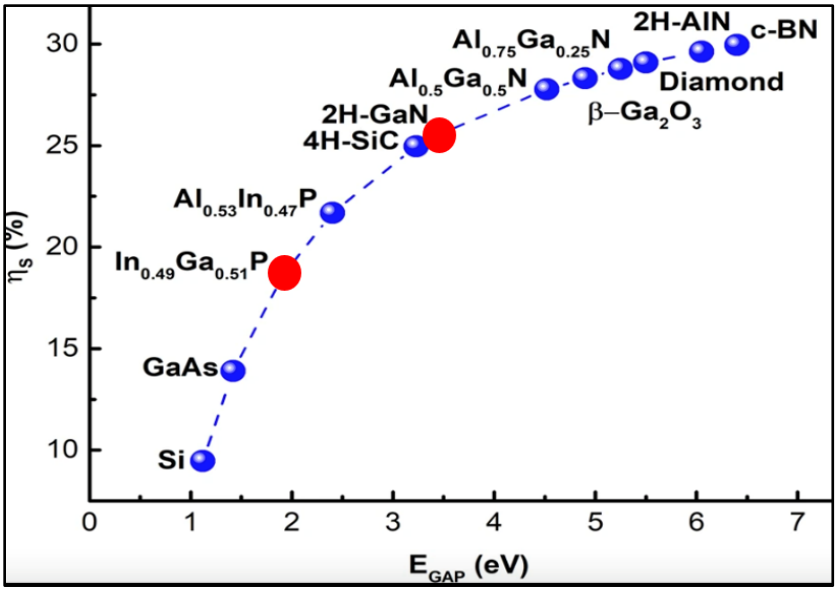

Figure 1.4: The maximum overall efficiency (theoretical) of a betavoltaic devices on different semiconductors [51].

1.5.1 Motivation for GaN Semiconductor for Betavoltaic Devices:

Theoretical analysis shows that the efficiency of betavoltaic device increases with the energy bandgap (E_g) of a semiconductor [51]. In this regard, gallium nitride (GaN) has an electronic bandgap of 3.4 eV, giving GaN a theoretical advantage in terms of betavoltaic efficiency and radiation resistance over common semiconductors such as Si (E_g = 1.12 eV) and 4H-SiC (E_g = 3.21 eV). Even though GaN is a direct bandgap semiconductor, it has regularly been used as a photovoltaic device when alloyed with other group III elements with efficiencies measured above 50 % [52]. In addition, GaN has the potential advantage of increasing the electron bandgap by adding aluminum

during growth to form an AlGaN solid solution, thus allowing for more output power and improved device efficiency. Another potential advantage of using GaN for a betavoltaic device is its non-centrosymmetric nature of the wurtzite crystal structure and intrinsic presence of polarization charge, which permits the growth of three-dimensional structures to increase the surface area of the device.

As mentioned above, most of the experimental results reported on GaN betavoltaic devices were on GaN films grown on top of a sapphire substrate. The lattice mismatch between the substrate and the GaN films results in misfit dislocations which could be attributed to the poor results. In this study, we investigated GaN films grown on top of sapphire substrates as well as free standing GaN films.

1.5.2 Motivation for InGaP Semiconductor for Betavoltaic Devices

InGaP is a moderate wide bandgap semiconductor with an electronic bandgap of ~ 1.86 eV. It is not as efficient and radiation hardened as GaN semiconductor, but it's maturity in terms of crystal growth and fabrication processes are well advanced compared to GaN semiconductor. Therefore, its cost is 10X cheaper than GaN wafer. Also, it is widely used for multi-junction solar cells in space which gives us confidence that InGaP semiconductors can withstand radiation emitted by beta sources without degradation.

1.6 Overview of the Chapters

Chapter 1 discusses the motivation for radioisotope power sources, their decay fundamentals, and different forms of radioisotope energy conversion. The scope of the work and motivation for selected semiconductors is also discussed in this chapter.

Chapter 2 covers the physics of betavoltaic power sources from device structure and operation to radioisotope selection criteria and their activity.

Chapter 3 covers the modeling and simulation approach using MCNP and Synopsys TCAD. Chapter 4 covers the fabrication process for GaN betavoltaic devices and chapter 5 covers the characterization and results/discussion of GaN betavoltaic devices. Chapter 6 is focused on characterization and evaluation of InGaP devices for betavoltaic power sources.

In chapter 7, an extension of this work on direct alphavoltaics and indirect alpha-photovoltaics is presented. Chapter 8 summarizes the study performed in this dissertation and includes a future work section.

Chapter 2: Physics of Betavoltaic Power Source

A betavoltaic power source has two main components: a beta emitting source, and a semiconductor junction in a form of pn/p-i-n diode. Figure 2.1 shows the schematic of a betavoltaic power source.

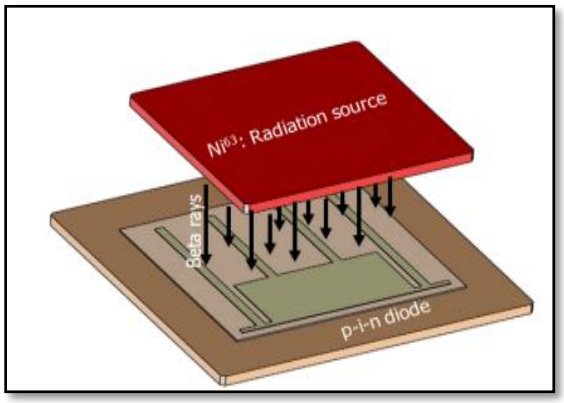

Figure 2.1: Schematic of Betavoltaic Power Source.

A semiconductor junction is the key component of a betavoltaic power source which harvests and converts the kinetic energy of beta particles into electrical energy. In order to understand the operation of a betavoltaic device, it is important to first look at the behavior of semiconductors and semiconductor junctions. In the next sections, basic semiconductor physics is discussed, followed by a discussion about the principal design and operation of betavoltaic devices.

2.1 Basic Semiconductor Physics

Semiconductor is a material that has a conductivity in between of a metal and an insulator. Two types of semiconductors exist: elemental semiconductors that are composed of single species of atoms such as silicon (Si) and germanium (Ge), mostly found in group IV of the periodic table, and compound semiconductors which are composed of two or more elements [53-54]. GaN (binary compound with gallium from

group III and nitrogen from group V) and InGaP (ternary compound with Indium from group II, gallium from group III, and phosphor from group V) are examples of compound semiconductors. An intrinsic semiconductor refers to a pure semiconductor material with no impurities in the crystal lattice. The process of adding impurity atoms by diffusion/ion implantation is called doping. Doping is a controlled method to create excessive electrons or hole concentration in a semiconductor to change its electrical properties. An example of doping process in silicon is shown in figure 2.2.

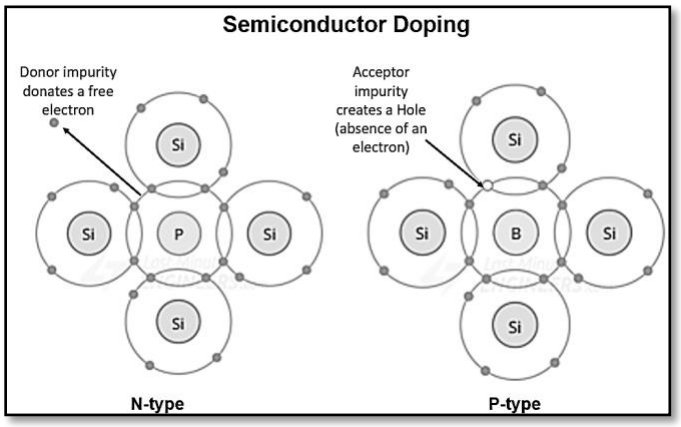

Figure 2.2: P-type and N-type levels in a semiconductor [55]

In the case of silicon, boron atoms are added to silicon to create excess concentration of holes. Boron is a trivalent atom (group III), and it has 3 electrons in its valence band (the outermost shell). It accepts an electron from silicon which leaves behind a vacancy (also known as hole) in silicon. The region of a semiconductor which have excessive holes is called a p-type. Similarly, if silicon is doped with a pentavalent atom such as phosphorous with five valence electrons, it will gain an electron. An extra electron will make silicon more conductive, and we call this an n-type semiconductor. Both electrons and holes contribute to a current. A doped or undoped semiconductor by itself is not a useful device - it behaves more like a resistor (dielectric layer).

However, when a single crystal of a semiconductor is doped with either an n or p-type impurities and a metal contact is deposited on it, it forms a schottky junction. Similarly, when a single crystal semiconductor is doped with both n and p-type impurities, it forms a pn junction. Both pn and schottky junctions are the building blocks for most electronics used today including diodes, transistors, integrated electronics, among others. For direct energy conversion devices such as a betavoltaic power source, creation of depletion region and width of it is the key performance parameter because only electron hole pairs (EHPs) that are generated in the depletion region or vicinity of it contribute to the output power, rest of them recombine and contribute to losses in the device. A pn junction is preferred over a schottky junction for a betavoltaic power source because of the larger depletion region width compared to a schottky junction.

A pn junction is formed when a single crystal semiconductor is doped with p-type impurities in one region, and with n-type impurities in the adjacent region. The interface separating the two regions is called the metallurgical region. Figure 2.3 shows the schematic of a pn junction formation.

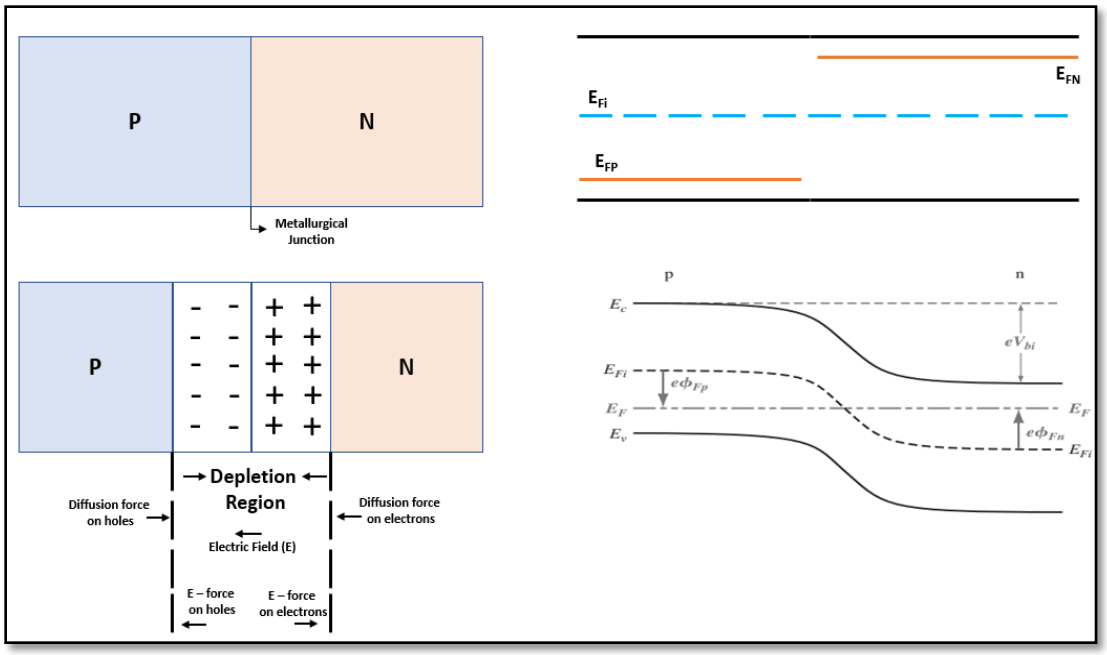

Figure 2.3: Formation of a pn junction and its band diagram (top left & right). b). Formation of a depletion region in a pn junction and its representative band diagram (bottom left & right).

Initially, at the metallurgical region, there is a very large density gradient in both electron and hole concentrations. The majority carriers (electrons) in the n-region will begin diffusing into the p-region, leaving behind negatively charged ions (acceptor atoms). Similarly, majority carrier holes in the p-region will begin diffusing into the n-region and they leave behind positive charge ions (donor atoms). These charges (positive and negative ions) are fixed, and the region containing these fixed charges is called the depletion region. Due to these fixed charges in the depletion region, there is an electric field which works against the diffusion of carriers, wants to keep holes in the p-side and electrons in the n-side. Due to this electric field, drift current originates in the depletion region, which drifts the holes in the n-side back to p-side and electrons from the p-side back to n-side. The electrons created thermally in the *p*-material and the holes created thermally in the *n*-material behave in the same way, and they create a

current density, $-J_s$, often called the reverse saturation current density. It is negative because the holes are drifting towards the *p*-side and electrons are drifting towards the *n*-side.

A width of the depletion region is given by:

$$x_n = \sqrt{\frac{2\varepsilon}{q} Vbi[\frac{N_a}{N_d}] * \frac{1}{N_a+N_d}} \qquad (2.1)$$

$$x_p = \sqrt{\frac{2\varepsilon}{q} Vbi[\frac{N_d}{N_a}] * \frac{1}{N_a+N_d}} \qquad (2.2)$$

$$W = x_n + x_p = \sqrt{\frac{2\varepsilon Vbi}{q} * \frac{N_a+N_d}{N_a N_d}} \qquad (2.3)$$

Where x_p and x_n are the width of the depletion region (W) in the *p*- and *n*-type material, respectively. W is the total width of the depletion region. Na and Nd are the donor and acceptor concentrations, V_{bi} is the built-in potential barrier, and ε is the electrical permittivity of the semiconductor. In a schottky junction, the depletion region width is only on one side of the n-type or p-type material because the other side is a thin metal layer. That is the reason for a small depletion region width in schottky junctions.

For an abrupt junction where both sides of the junction are uniformly doped, the electric field is given by:

$$E\text{max} = \frac{-qN_d x_n}{\varepsilon} = \frac{-qN_a x_p}{\varepsilon} \qquad (2.4)$$

At thermal equilibrium, no net current flows through the pn junction because the drift current is equal to the diffusion current, and the fermi energy levels of n and p type materials line up causing band bending, as shown in figure 2.3. The band bending creates a potential barrier at the junction. The potential barrier is created by electrons

flowing over to the *p*-side and ionizing the acceptors with negative charge, while leaving positively charged donors on the *n*-side.

If we make the assumption that $n = N_d$ in the *n*-type material, and $n = N_a$ in the *p*-type material, where N_d and N_a are respectively, the donor and acceptor concentrations – then the built-in potential barrier, V_{bi}, is given by:

$$qVbi = E_{Fn} - E_{Fp} = kTln\left(\frac{N_A N_D}{ni^2}\right) \quad (2.5)$$

The Fermi energy levels: E_{Fn}, is a measure of concentration of electrons in the conduction band and E_{Fp} is a measure of concentration of holes in the valance band. In n-type material, E_{Fn} lies closer to the conduction band and the thermal-equilibrium electron concentration is given by:

$$n = n_i * \exp\left[\frac{E_F - E_{Fi}}{KT}\right] \quad (2.6)$$

where n_i and E_{Fi} are the carrier concentration (electrons in the conduction and holes in the valence band) and Fermi energy level of an intrinsic (undoped) material, respectively. E_{Fi} lies at the middle of the energy gap in an intrinsic material.

In *p*-type material, E_{Fp} lies closer to the valence band and the hole concentration is given by:

$$p = n_i * \exp\left[\frac{-(E_F - E_{Fi})}{KT}\right] \quad (2.7)$$

The built-in potential barrier to the diffusion current can be altered by applying external stimulus such as voltage, photon, or beta excitation. A positive stimulus (voltage, photons, or beta particles) will lower the barrier, while a reverse bias (negative voltage) will raise it. Since the probability that a carrier can diffuse over the potential barrier depends exponentially on the height of the barrier, the diffusion current can be written as

$$J_{diff} = J_s * \exp\left(\frac{qVbi}{kT}\right) \quad (2.8)$$

Where k is Boltzmann's constant, V_{bi} is the built-in voltage (barrier height) and T is the temperature.

The drift current is not affected by the applied voltage so the total current density when the diode is not exposed to light or betas is,

$$J = J_s * [\exp\left(\frac{qVbi}{kT}\right) - 1)] \quad (2.9)$$

Equation 2.9 is the ideal diode equation which gives an expression of current through a diode as a function of voltage where J is the net current flowing through the diode, J_s is the dark saturation current or the diode leakage current density in the absence of beta/photons, V_{bi} is the applied voltage across the pn junction, $\frac{KT}{q}$ is the thermal voltage and it equals ~ 25.9 mV at 300 K.

The "dark saturation current" (J_s) is an extremely important parameter. It is a measure of the recombination (electrons and holes) in a device. A diode with a larger recombination will have a larger J_s. J_s increases as temperature increases; and J_s decreases as material quality increases [53, 55].

2.2 Device Structure of Betavoltaic Devices

Betavoltaic devices are mostly made by creating a *p-i-n* junction in the semiconductor as shown in figure 2.4.

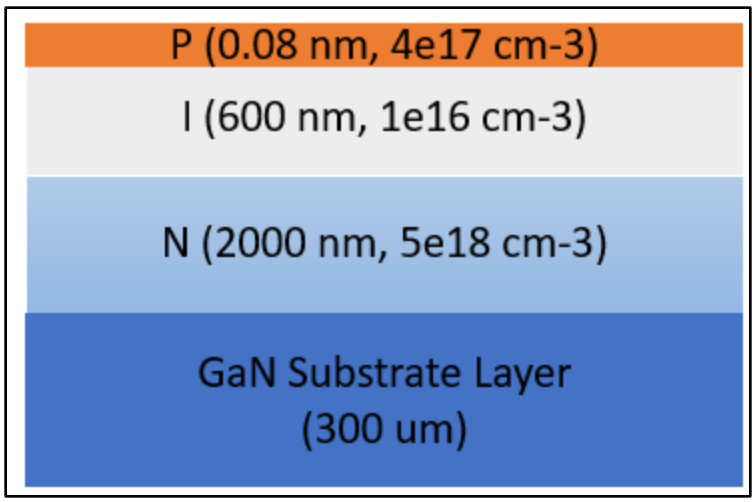

Figure 2.4: Structure of a GaN Betavoltaic structure with epilayer thicknesses and doping levels.

The *i* (intrinsic) layer is added to the *pn* junction to increase the width of the depletion region. A wider depletion region enables the capture of more electron hole pairs (EHPs) created by the collision of the beta particle with the lattice, thus increasing the output power and efficiency of the device. The layer that is illuminated first is the top p-layer. It is usually made very thin so that most of the beta particles can penetrate through it and generate the maximum number of EHPs in the depletion region where they are quickly separated and drifted to the contacts by the electric field. Because the p-layer is made thin, it must be heavily doped so that it will not be completely ionized by the depletion layer destroying its ability to act as an effective *pn* junction; this phenomenon is called punch through. The base layer (n-layer) is also heavily doped because this reduces the on-resistance, R_{on}. The middle *i*-layer is not intrinsic as suggested by the name. The intrinsic case – doping in the range of $<10^{10}$ - would not only be difficult to attain, but extremely low doping would cause the device to have a large R_{on} [56-57]. Hence, the so-called intrinsic layer is actually an n^- (n minus) layer with a doping concentration of a few orders of magnitude lower than the n^+ layer. The

low doping creates a wider depletion region where virtually all of the EHPs generated in it are captured by its electric field. It also increases the probability that the carriers created outside of the depletion layer, but close to it, will be captured by the E-field in the depletion region by diffusing into it before recombining. The lower doping in the intrinsic region also ensures higher minority carrier lifetime and higher diffusion coefficients, which in turn increases the carrier diffusion length.

The average distance the minority carrier can diffuse before it recombines is the minority carrier diffusion length (L_n or L_p), which depends on the average time it takes to recombine, the minority carrier lifetime (τ_n or τ_p), the rate at which it diffuses, and the minority carrier diffusion coefficient (D_n or D_p). The relationship is given [58] by:

$$L = \sqrt{D\tau} \qquad (2.10)$$

$$\frac{D}{\mu} = \frac{kT}{q} \qquad (2.11)$$

Where μ is the carrier mobility.

2.3 Operation of Betavoltaic Devices

The semiconductor junction part of a betavoltaic device is at thermal equilibrium before a beta source is placed on top of the device. The depletion region exists in the device structure and there is an electric field present. Now when a beta source is placed on top of semiconductor junction, beta particles penetrate the semiconductor device and create EHPs as they collide with the lattice. This is analogous to how a photovoltaic device operates: photons with energies higher than the band-gap energy of the semiconductor material get absorbed and generate EHPs. An absorbed photon usually generates only one EHP. On the other hand, beta particles have much higher energies, and a single beta particle can generate many EHPs [58-59].

As beta particles penetrate into the semiconductor junction, they undergo many inelastic collisions. A part of their energy is used to excite electrons from the valence band into the conduction band creating EHPs, and the rest of the energy is lost as heat through phonon interactions in the semiconductor [59]. Essentially all the EHPs generated in the depletion region contribute to the *beta*-current density, J_β, because they are swept out by the electric field in it. Some of the EHPs generated near the depletion region diffuse into it before they recombine and are swept out by the electric field in the same manner. They are the *beta*-induced electrons in the *p*-material and the *beta*-induced holes in the *n*-material. Only EHPs generated within a diffusion length from the depletion region or inside the depletion region are collected and produce current. This process is shown in figure 2.5.

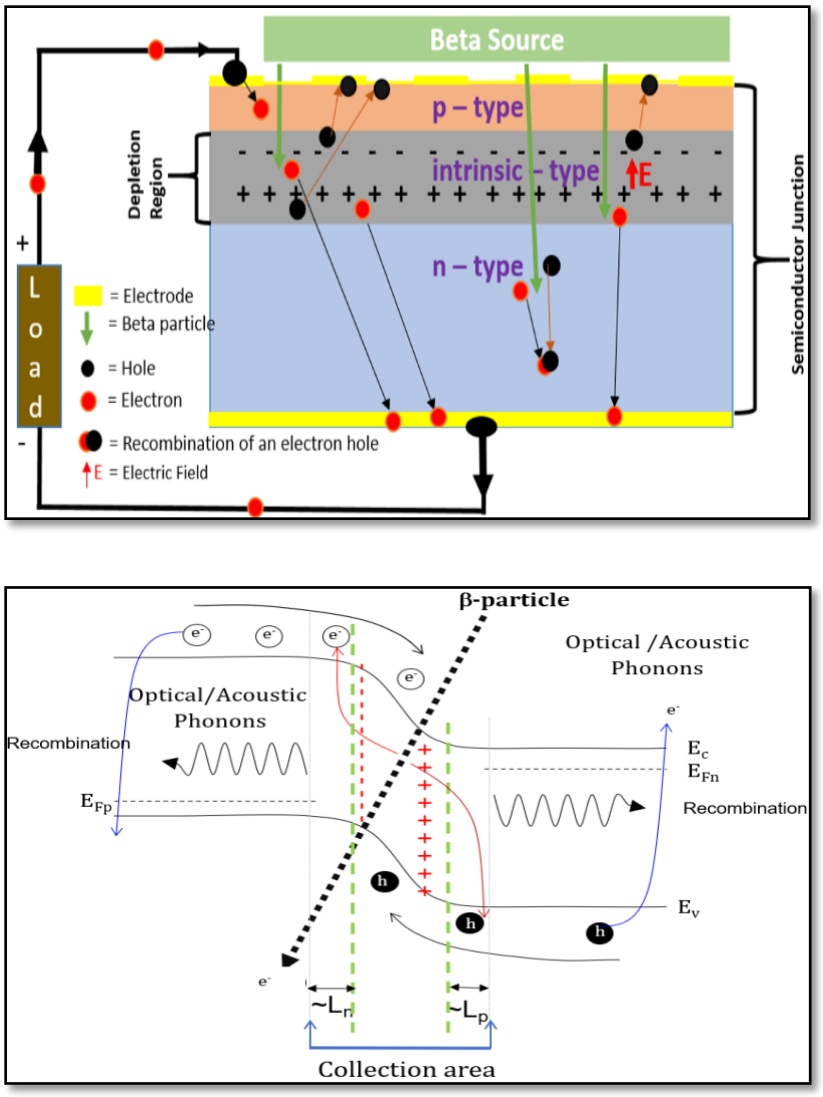

Figure 2.5: Betavoltaic device under beta illumination: a) side view of a device structure and b) band diagram representation.

The current density in a betavoltaic device is described by the equation.

$$J = Js * [\exp(\frac{qV}{kT}) - 1)] - J\beta \qquad (2.12)$$

If the diode is not connected to an external load, charge will build up on either side of the junction with the *p*-side becoming positively charged by the injection of the *beta*-excited holes, and the *n*-side becoming negatively charged by the injection of the *beta*-excited electrons. This charge creates a positive voltage, which will lower the

barrier height, which will increase the diffusion current. A new thermal equilibrium will be reached when there is no net current flow because the diffusion and drift currents are now equal but opposite. One can easily show the voltage across the junction when this occurs, the open circuit voltage, V_{oc} by:

$$V_{oc} = \left(\frac{kT}{q}\right) * \ln\left[1 + \left(\frac{J_\beta}{Js}\right)\right] \qquad (2.13)$$

It can be seen from the above equation that V_{oc} will be larger when J_s is smaller. J_s is smaller in wider band gap semiconductors because fewer thermal electrons and holes can be created because they are formed by electrons jumping over the energy gap, E_G. It can, in fact, be shown that J_s is proportional to $e^{-E_G/kT}$. Due to this reason, wider band gap semiconductors always have higher V_{oc} and it goes up as the energy gap of a material is increased. Since, the Fermi energies in the *p* and *n* material are further apart for the same doping levels in wider band gap semiconductors, V_{oc} will also be larger.

Under beta irradiation, the generation of EHPs does not significantly increase the majority carrier concentration. However, the minority carrier concentration is significantly increased and hence, the diffusion current dominates due to the concentration gradient developed in the quasi-neutral region. As noted above, the flow of generated minority carriers essentially defines the direction of the beta-induced current density flowing from the *n*-terminal to *p*-terminal. Collection of all the negative charges on the *n* side and positive charges on the *p* side creates a beta-induced forward bias to the betavoltaic cell. As a result of this forward bias in the presence of an external load, diode current begins to flow in the opposite direction to the beta-generated current and is typically referred to as diode dark current, J_{dark}. J_{dark} is same as J_s discussed above. It is important to minimize the dark current as it reduces the beta-generated current.

When the diode is shorted so that no voltage is applied across the junction; there is no diffusion current to offset J_β, so now the current density is $-J_\beta$. This is also called the short circuit current density, J_{sc}.

The current density given by eq. 2.9 is for an ideal diode. In a real diode there are point defects in the depletion region called traps/dislocations which can trap some of the carriers in the depletion region. Trap states decrease the current density and are accounted phenomenologically by inserting a number, *n*, called the ideality factor, into the exponent, as illustrated in eq. 2.14:

$$J = J_s\left(e^{\frac{qv}{nkT}} - 1\right) \qquad (2.14)$$

When the traps have a dominant effect, the value of $n \approx 2$, and when their effects are small, $n \approx 1$ are observed [*2*].

For a device under beta illumination, eq. 2.14 for the current density is modified by J_β so,

$$J = J_s\left(e^{\frac{qv}{knT}} - 1\right) - J_\beta \qquad (2.15)$$

As noted in the discussion above, J_s decreases exponentially with the energy gap, so it is very small for the larger band gap semiconductors and is therefore more sensitive to the increases caused by defects. It is therefore even more important for the wider band gap semiconductors to have very high quality *pn* junctions.

Since β-generated current density is negative, the IV curve drops down into the 4th quadrant, which indicates the device is generating, as opposed to consuming, power. The current-voltage (IV) characteristics of a betavoltaic device under beta irradiation and under no irradiation (Dark) are represented in figure 2.6.

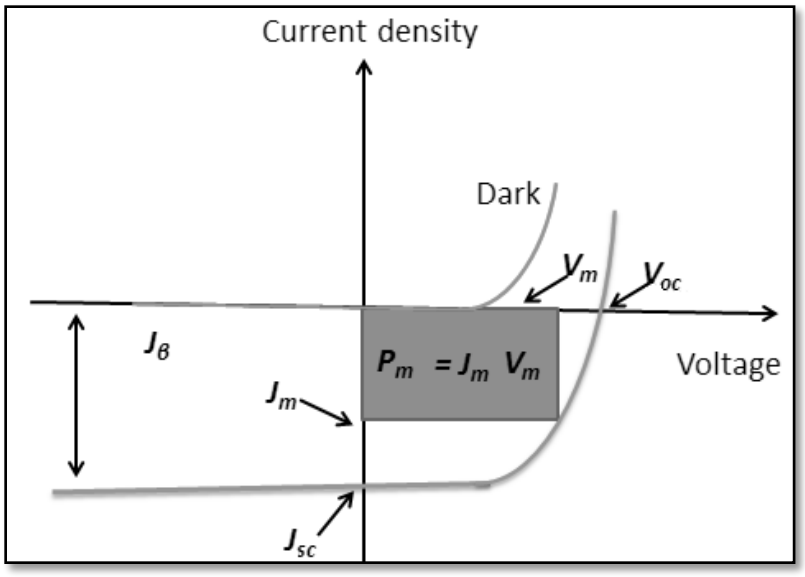

Figure 2.6: IV characteristics of a device in the dark and under beta illumination.

In order to deliver real power to the load, the betavoltaic cell does not operate in open circuit voltage or short circuit configurations. Instead, it operates under the illuminated IV characteristics between the two extremes as shown in figure 2.6. The maximum power from the betavoltaic cell is obtained when the resistance of the load is selected such that it allows the current-voltage product to be maximized. The point at which this output power is maximized is called the maximum power point, P_m and can be expressed as:

$$P_m = J_m V_m \qquad (2.16)$$

Where J_m and V_m are the peak current density and peak voltage points, respectively. The efficiency of a betavoltaic device (η) describes its ability to efficiently convert incident beta particles into output electrical power. It can be described as the amount of maximum power density delivered (P_m) as a fraction of the incident beta power density from the radioactive source and can be expressed as:

$$\eta = \mathrm{FF}\frac{V_{oc} * J_{sc}}{E_\beta * J_\beta} \qquad (2.17)$$

Where E_β is the mean incident energy of beta radiation and J_β is the incident flux of beta-particles. Claude Klein showed empirically that when a beta particle creates an EHP, the average energy it gives up is $2.8\,E_g + 0.5\,eV$, with $1.8\,E_g$ of that energy is lost to optical phonons and 0.5 eV is lost to acoustic phonons. This accounts for 65% of the total beta energy not used in creating EHPs, which caps the betavoltaic conversion efficiency to only 35% [59]. This means that a planar betavoltaic device cannot be more than 35% efficient.

Figure 2.7 shows the equivalent circuit model of a betavoltaic device that considers the series resistance (R_s), shunt resistance (R_{sh}) and dark current.

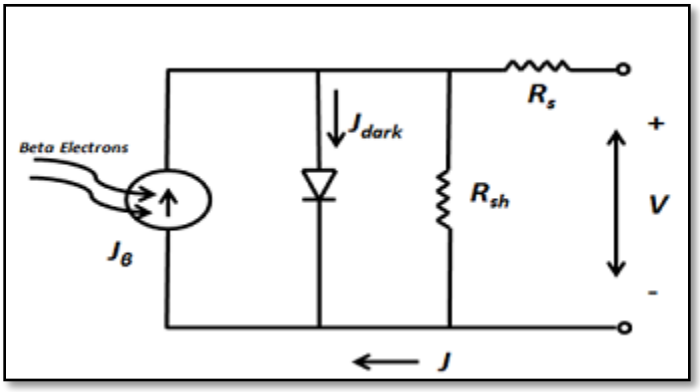

Figure 2.7: Example of an equivalent circuit considering series and shunt resistances.

The current density taking into account the influence of series resistance (R_s) and shunt resistance (R_{sh}) is given by equation 27:

$$J = J_\beta - Js\ (\exp\left[\frac{V+J_{RS}}{\frac{nKt}{q}}\right] - \frac{V+J_{Rs}}{R_{sh}}) \qquad (2.18)$$

R_s and R_{sh} to some extents are dictated by the thickness of the *i*-layer. If it is too thin, the depletion layer will punch through, and the resistance will be negligible. If it is too thick, it will increase the resistance, since it has a much lower doping level. A good estimate of the ideal thickness of the intrinsic layer in a p-i-n device is the

thickness of the depletion layer plus the minority carriers' diffusion length of carriers in that semiconductor.

2.4 Selection of a Radioisotope for a Betavoltaic Power Source

The choice of a radioisotope is an important design parameter because it determines the lifetime (half-life), output power and reliability of the betavoltaic device. Selection of half-life depends on the service life requirement of the power source. Other important parameters to consider include cost/availability, safety, and maximum energy. Some beta emitters also emit gamma radiation along with the beta particles, requiring a large amount of shielding in order to use them for a power source. Therefore, those beta emitters are also not considered such as strontium-90.

Table 2.1 shows two beta emitters which are selected based on their superior half-life time (> 10 years), availability/cost, safety, and maximum energy emission that is below the threshold damage of semiconductor junction.

Table 2.2: Properties of Tritium and Nickel-63 beta sources. The average specific power (mW/g) is directly proportional to the average energy of the beta particles emitted, but inversely proportional to the half-life of the radioisotope.

Radioisotope	Half life (T1/2) Years	Average Energy Emission (KeV)	Maximum Energy Emission (KeV)	Specific Activity (Ci/g)	Average Specific Power (mW/g)	Cost ($ per Ci)
Tritium	12.3	5.7	18.6	9800	325.00	3.5
Nickel-63	100.2	17.42	66.95	60	5.80	4000.00

2.4.1 Tritium (^{3}H)

^{3}H is a radioactive isotope of hydrogen that contains one proton and two neutrons. ^{3}H is a pure *(naturally found)* beta emitter which has a specific power of 325

mW/g with a half-life of 12.3 years, an average energy of 5.7 keV and a maximum energy of 18.6 keV. ^{3}H can be used in a gas phase and it can be combined with a metal to form a metal hydride or incorporated into a solid organic metal such as plastic [60].

2.4.2 Nickel-63 (Ni-63)

Ni-63 is the most widely used radioisotope for betavoltaic energy conversion and is a pure beta emitter. However, it has a low average specific power of 5.8 mW/g compared to the other beta emitters [61]. The specific power of Ni-63 is low because of its long half-life. It has a half-life of ~ 100 years, average beta energy of 17.4 keV and a maximum energy of 67 keV. Ni^{63} can be evaporated on films just like other metal as well as be deposited using an electrodeless technique with an aqueous solution of nickel salt and hypophosphite [62-64].

2.5 Isotope Activity for Betavoltaic Energy Conversion

The actual activity of a radioisotope determines how much energy the radioisotope has, and it is the inherent characteristics of a radioisotope depending on its specific activity and mass. Not all the actual activity a radioisotope has makes it to the semiconductor junction due to self-absorption effect in the isotope itself before radiation can exit. Apparent activity is the effective activity that is emitted by the source and would be measured by a radiation detector [65]. Apparent activity is always less than the actual activity, and it is given by:

$$\phi = \frac{c}{\mu m}(1 - e^{-\mu m * tm}) \qquad (2.19)$$

$$\mu m = \frac{0.017}{E_{max}^{1.43}} \qquad (2.20)$$

Where C is the specific activity in mCi/mg, μm is the mass attenuation coefficient (cm^2/mg) of the radioactive source material, t_m is the mass thickness of the radioactive source, and E_{max} is the maximum energy of the radioisotope in MeV [65]. Figure 2.8 shows the actual activity vs. apparent activity of Ni-63 and ^3H beta sources.

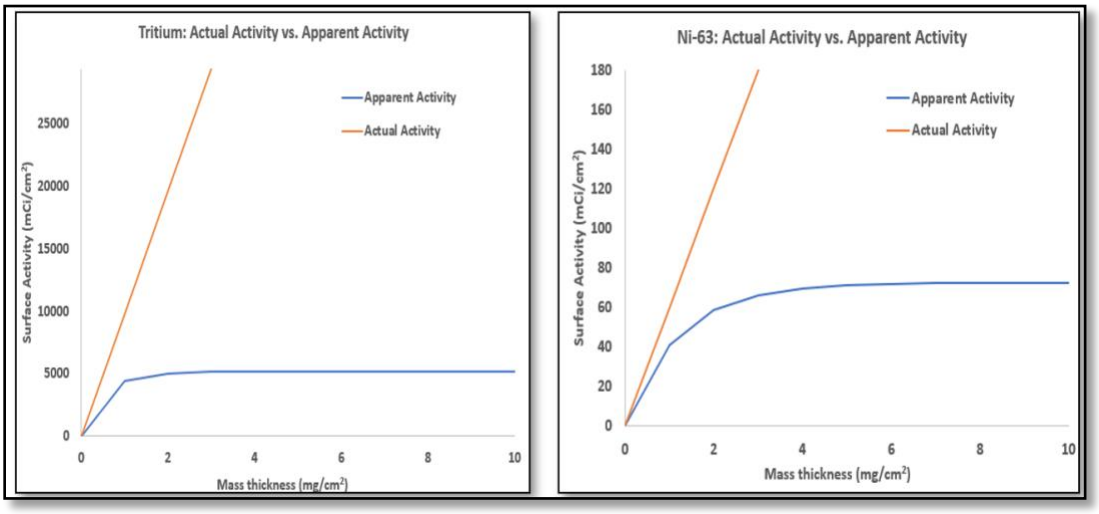

Figure 2.8: Actual and Apparent activity vs. mass thicknesses of beta isotopes: a) Tritium, b) Ni-63.

As shown in figure 2.8, the surface activity (mCi/cm^2) of a radioisotope initially increases with an increase in the mass thickness (g/cm^2), but then saturates due to self absorption effect. Ni-63 source fully saturates at the thickness of 4 mg/cm^3, which means any thickness of the source over 4 mg/cm^3 will produce the same surface activity of ~75 mCi/cm^2. This analysis is useful for designing a betavoltaic power source with the maximum utilization of the radioisotope activity for reduced cost.

The electrical output power density can be determined by [66-67]:

$$P_{radioisotope} = 3.7\ x\ 10^{10} q \phi E_{ave} \qquad (2.21)$$

Where q = 1.602 x 10^{-19} is the electron charge, ϕ is the effective activity (beta flux) and E_{ave} is the average energy emission of a radioisotope material.

Using equations above , we can estimate the power density of Ni-63 and ^{3}H beta sources at a thickness when the surface activity (mCi/cm^2) starts to saturate. This takes place at ~ 4 mg/cm^3 for both beta sources, representing surface activities of ~ 75 mCi/cm^2 with a power density of 7.6 $\mu W/cm^2$ for Ni-63, and 5156.5 mCi/cm^2 with a power density of 170 $\mu W/cm^2$ for Tritium. The nuclear regulatory commisson (NRC) regulates how much activity of a radioisotope can be put in a single package for transportation/handling for Type A package [68]. A1 is the maximum activity allowed in a type A package for special form material; A2 is the non-special form material allowed in a type A package[68]. For Tritium, the maximum activity allowed in type A1 and A2 packages are 1100 Ci. For Ni^{63}, the maximum activity allowed is 1100 Ci for type A1 package, and 8100 Ci for type A2 package[68].

Chapter 3: Modeling and Simulation of GaN P-I-N Devices for Betavoltaic Energy Conversion

In this chapter, modeling and simulation tools are utilized to optimally design betavoltaic devices to support experimental results. Two types of simulations methods are utilized: Monte Carlo N-Particle (MCNP) modeling to determine the energy profile of beta particles into semiconductor material, and Physics-based technology computer aided design (TCAD) to estimate the width of the effective charge collection area. As discussed in chapter 2, incident beta particles deposit their energy into a semiconductor along their path. About 35 % of that energy is used to create electron hole pairs (EHPs), and rest of that energy is used for phonon creation and other mechanisms. EHPs that are created in the charge collection area (width of depletion region plus the minority carrier diffusion length) contribute to output power, rest of them recombine and contribute to losses. In designing betavoltaic devices, the goal is to maximize EHPs generation in the depletion region because EHPs are separated and drifted to their respective terminals by the electric field. MCNP code is utilized to model the energy deposited (# of EHPs created) by beta particles as a function of penetration depth into the semiconductor material and TCAD model utilizes this information to estimate how many of these EHPs contribute to the output power. The combinations of these two simulation methods provide a feedback loop with experimental work to intentionally improve betavoltaic devices performance.

3.1 MCNP Modeling

Monte Carlo N-Particle (MCNP) is a general-purpose continuous energy transport code to track particle energies over a broad range. It is widely used to model neutrons,

photon, and electron transport and their interaction with matter for the purpose of determining energy deposition/dose in the material, shielding and other quantities of interest [69-70]. MCNP code is utilized in betavoltaics to model the penetration range of beta particles in different semiconductor structures. The likelihood of specific emission energy is dictated by a probability spectrum defined by the user.

We utilized MCNP code to model the energy deposited into GaN semiconductor for monoenergetic electron beam at various energies. Electron beam energies of 6 KeV and 17 KeV represent the average energy emission of ^{3}H, and Ni-63, respectively. Since we can experimentally test devices from 1 KeV up to 16 KeV utilizing the EBIC (electron beam induced current) system located in our facility, we modelled the energy deposition profile of monoenergetic electron beam in 3 KeV increments up to 18 KeV to get more data points to compare with the experimental results.

Figures 3.1a shows the energy distribution profile of monoenergetic electron beam of various energies into GaN semiconductor. Initially, we see an increase in the deposited energy with the increase in depth, and then it decreases as the penetration depth increases. Figure 3.1b shows the energy deposited normalized for 99% of the total energy deposited. Table 3.1 shows the penetration depth values for each monoenergetic electron beam where 99 % of the total energy is deposited.

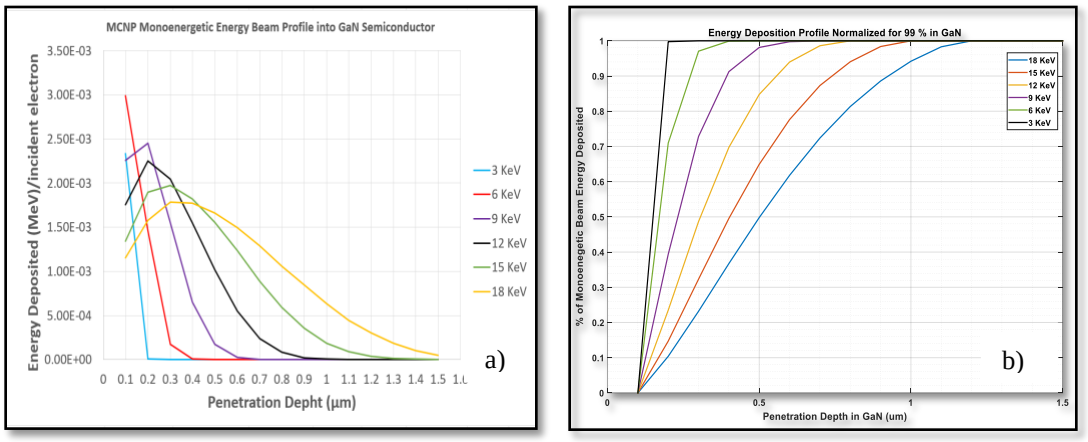

Figure 3.1: a) Energy deposition profile of monoenergetic electron beam into GaN material, b) the energy deposition profile normalized for 99% of the total energy deposited.

Table 3.3: Penetration depth (µm) in GaN where the deposition energy is normalized for 99 % of the total energy deposited.

Monoenergetic Electron Beam	Penetration Depth (um)
3 KeV	0.2
6 KeV	0.35
9 KeV	0.55
12 KeV	0.75
15 KeV	0.95
18 KeV	1.15

The energy deposition profile is needed to determine the # of electron–hole (EHPs) pairs created as a function of penetration depth. According to reference [71], ~ 8.9 eV of ionization energy (ε) is required to create one EHP in GaN. By using equation 3.1, we can calculate the number of EHPs created in the GaN device at each penetration depth, as depicted in figure 3.2.

$$\#\ of\ EHPs = \frac{Edep}{\varepsilon} \qquad (3.1)$$

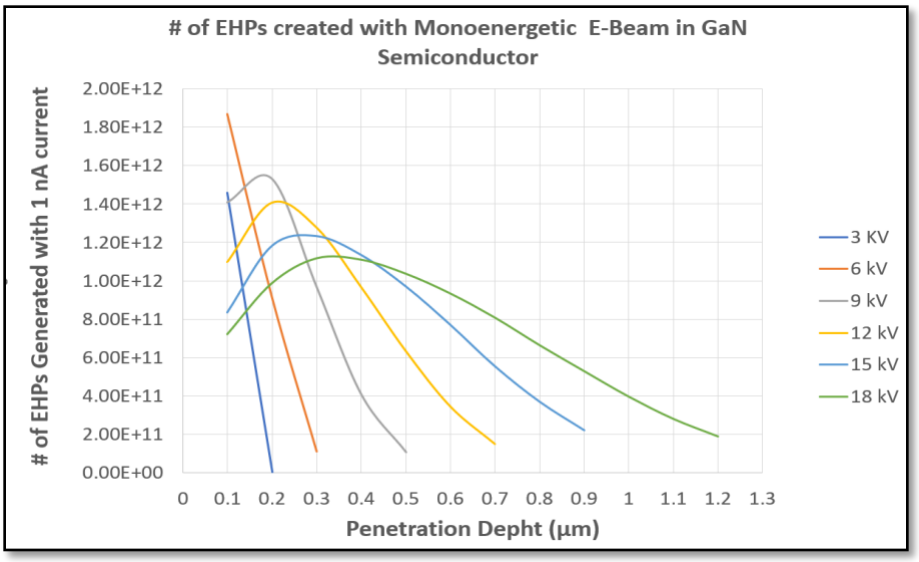

Figure 3.2: EHP generation profile as a function of penetration depth in GaN semiconductor. It shows that higher energies of the beam penetrate deeper into the material.

3.2 Sentaurus TCAD

Sentaurus TCAD is a suite of tools developed by Synopsys which are used in the semiconductor industry for a wide range of applications from fabrication process optimization to fine tuning semiconductor device structures. Generally, it solves the poisson equation simultaneously with the drift-diffusion equations for both electrons and holes by using numerical methods such as finite-difference and finite-element. It incorporates an extensive set of physical models and material parameters, and simulates 1D, 2D and 3D geometries over a wide range of analysis modes, such as DC, AC, transient and harmonic balance. The main tools within the Sentaurus TCAD suite are Structure Editor/Mesh, Device, Workbench, and Visual. Within Structure Editor, the 2-D or 3-D device structure dimensions can be defined along with material type, doping profiles, meshing strategies, and contact placement. Default material properties (for example, GaN and Si) are provided by Sentaurus, it is possible to adjust the material properties using a user defined parameter (.par) file. For example, the bandgap, density

of states, thermal conductivity can all be customized. Once the structure is defined, Sentaurus Device takes the structure and meshing profile to compute the electrostatic potential, electron and hole concentrations and currents present within the device based on physics models solved at each mesh point. Solving at a discrete number of mesh points provides an approximation to a real device, so it is preferred that the meshing be laid out such that a higher resolution can be obtained within areas where a change in current density, electric field, and charge generation is expected. All device definitions can be scripted using the scheme scripting language. Lastly, Sentaurus Workbench and Visual are GUIs that provide a means to interact with simulation for analysis and visualization [72].

We used Synopsys TCAD to simulate three different GaN p-i-n structures. The details of epi-layer thicknesses and doping concentrations are listed in table 3.2.

Table 3.4: Epilayer details (layer thicknesses and doping concentrations) for three GaN p-i-n structures for this study.

P-i-N Structure	P		I		N	
	Thickness (um)	Doping Concentration	Thickness (um)	Doping Concentration	Thickness (um)	Doping Concentration
Adroit GaN/GaN	0.05	5e17 cm^{-3}	0.6	1e16 cm^{-3}	1	1e19 cm^{-3}
Adroit GaN/Sapphire	0.05	5e17 cm^{-3}	0.7	1e16 cm^{-3}	1	5e18 cm^{-3}
SUNY GaN/Sapphire	0.08	4e17 cm^{-3}	1	1e16 cm^{-3}	2	3e18 cm^{-3}

The doping concentration in each of these layers is realistic of what our collaborators could grow for us. The doping concentration of i-layer and thickness of it are the most critical parameters in defining the charge collection area in p-i-n devices. In all three structures, the doping concentration of i-layer is 1e16 cm^{-3} because it is hard

to grow a low doped intrinsic GaN layer without compensation [73]. However, we varied the thickness of i-layers: 0.6 µm, 0.7 µm, and 1 µm. The thickness of the p-layer is also critical as it determines how many of the beta particles can penetrate through it and create EHPs in the depletion region. If the p layer is made too thick, a lot of the generated carriers would not make it to the collection area. We simulated two structures with a p layer thickness of 50 nm (doping concentrations 4e17 cm^{-3}) and the third structure with a thickness of 80 nm (5e17 cm^{-3}). The thickness of n layer is not critical, but it is important to have high doping concentration in the n layer to reduce series resistance in the device. We used n layer doping concentrations of 3e18 cm^{-3}, 5e18 cm^{-3} and 1e19 cm^{-3}.

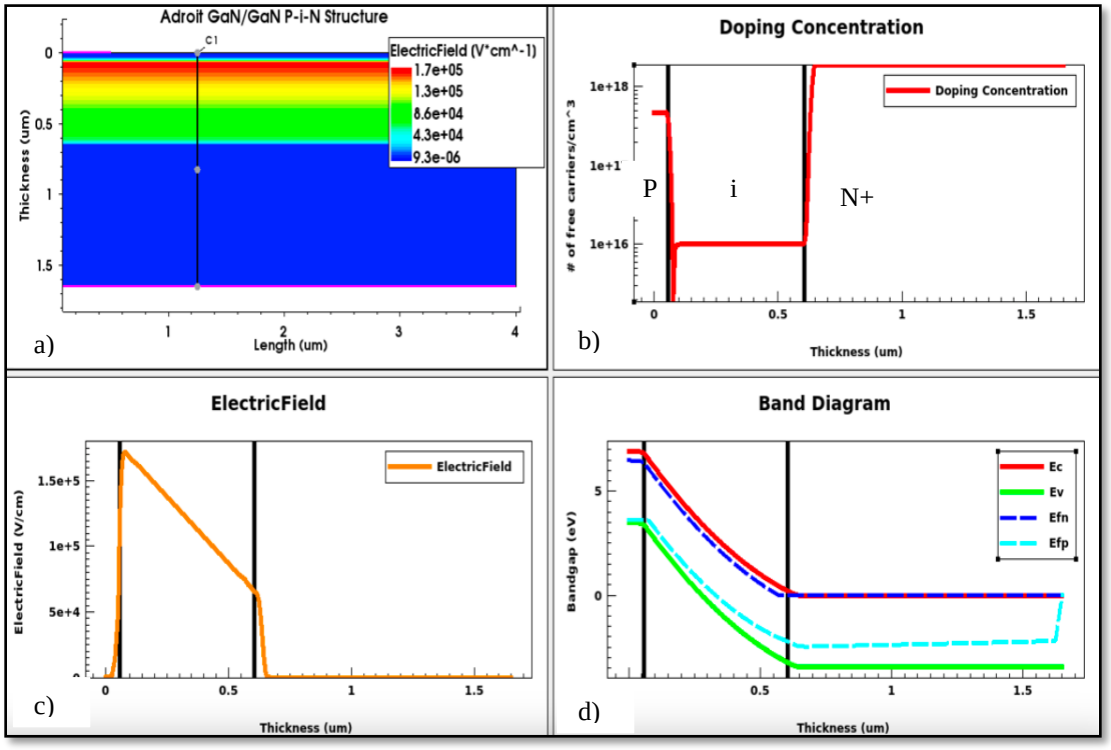

Figure 3.3: Electric field, doping concentration and band diagram of Adroit GaN/GaN p-i-n structure.

Figure 3.3 shows the Adroit GaN/GaN (AGG) p-i-n structure with an i-layer thickness of 0.6 µm. The i-layer is fully depleted and there is a continous electric field starting from the p-region and ending at the edge of i/n junction, as shown by figure 3.4c. The depletion region is represented by two vertical black lines and it is 0.6 µm thick (same as the thickness of i-layer). However, the charge collection area in this structure is 0.65 µm because there is an electric field extending to 0.65 µm as illustrated by figure 3.3c.

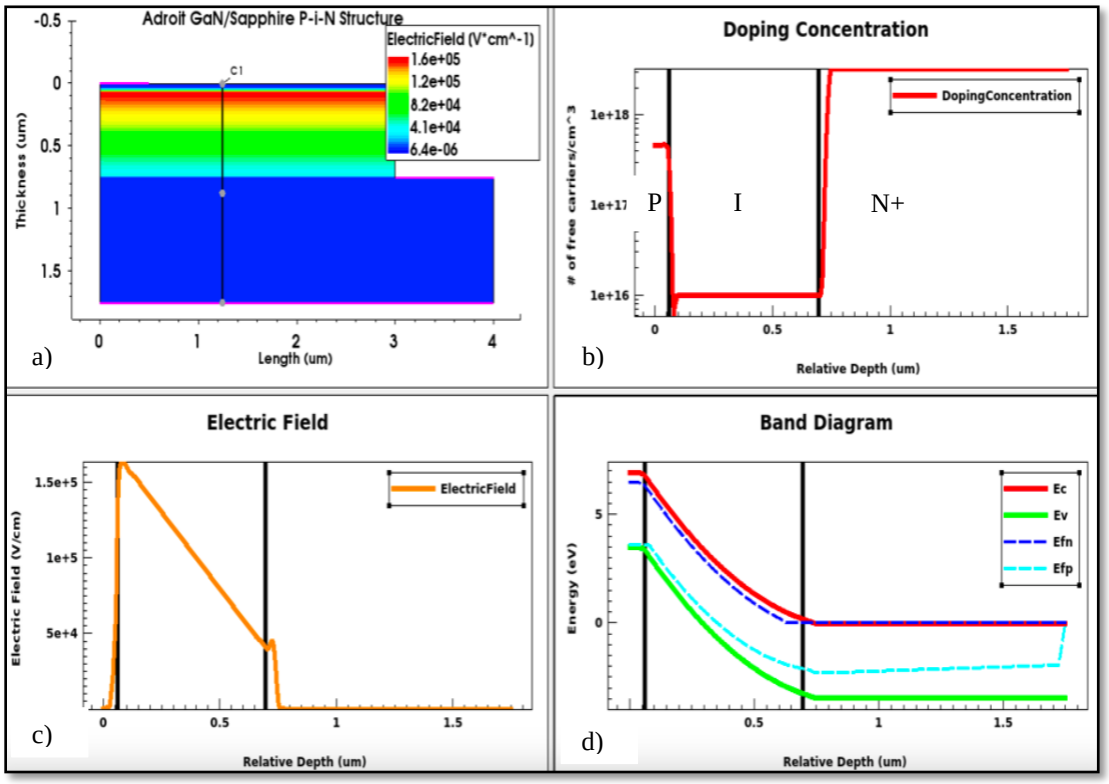

Figure 3.4: Electric Field, doping concentration and Band diagram of Adroit GaN/Sapphire p-i-n structure.

Figure 3.4 shows the Adroit GaN/Sapphire (AGS) p-i-n structure with an i-layer thickness of 0.7 µm. This structure also has a fully depleted i-layer and there is a continous electric field up until 0.75 µm. Therefore, the charge collection area in this structure is 0.75 µm as illustrated by figure 3.4c.

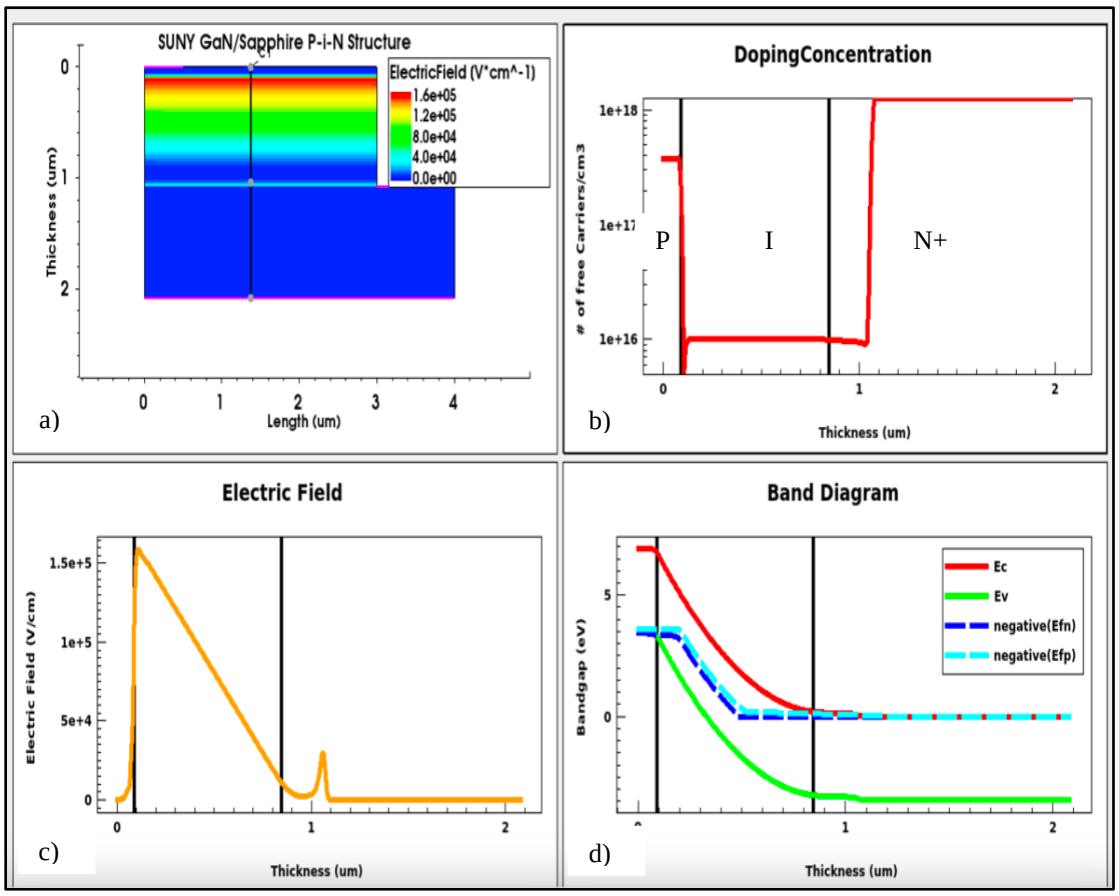

Figure 3.5: Electric Field, doping concentration and Band diagram of Suny grown GaN/Sapphire p-i-n structure.

Figure 3.5 shows the SUNY GaN/Sapphire (SGS) p-i-n structure with an i-layer thickness of 1 µm. In this case, an i-layer is not fully depleted as shown in figure 3.5a and 3.5c. The thickness of the depletion region is ~ 0.90 µm and the electric field goes to zero at the penetration depth of ~ 0.90 µm and stays zero untill the depth of 1 µm. However, at the junction of i and n layers, the electric field increases again from 1 µm to 1.08 µm due to difference in the doping concentrations of two n (i-layer and n layer) layers, as shown by figure 3.5c.

The effective charge collection area in this case is ~ 1.08 µm because the minority carrier diffusion length of holes is greater than 0.1 µm in the low doped n-layer (i-layer) [74-76]. Also, the electric field created at the 2nd junction plays a critical

role in diffusing the minority carriers created in the un-depleted region and drifts them into the depletion region where the probability of collection is almost 100%.

As shown in the simulation of three GaN p-i-n structures, the depletion region area is mostly made up by the thickness of the i-layer. However, the thickness of the i-layer is defined by its doping concentration (low doping concentration increases its width whereas high doping concentration reduces it). If an i-layer is made thick without reducing its doping concentration, it will result in an un-depleted i-region where electric field is zero, as illustrated in figure 3.5. If this un-depleted region is less than the minority carrier diffusion length, this charge collection area is continuous and extends the whole of i-layer. If this un-depleted region is greater than the minority carrier diffusion length, then this un-depleted region adds series resistance to the device, thus reducing its efficiency. Currently, controllable doping levels of less than 1e16 cm^{-3} are not possible for GaN semiconductors without compensation [73]. Figure 3.6 shows the maximum thickness of i-layer that is possible for each doping concentration that results in a fully depleted i-layer (optimal designs). The thickness of the collection area outside of the depletion region depends on the minority carrier diffusion length which is heavily impacted by the presence of point defects, traps and other defects presented in the semiconductor material.

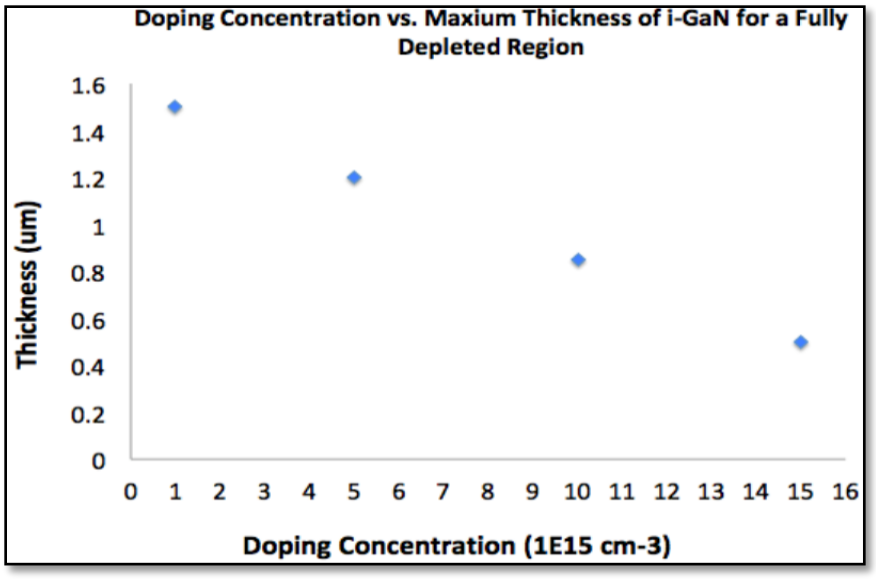

Figure 3.6: I-layer maximum thickness as a function of doping concentration that results in a fully depleted region. From this figure, we can estimate the charge collection area by including the minority carrier diffusion length of electrons and holes.

From figure 3.6, we can see that the depletion region increases to ~ 1.5 µm by lowering the doping concentration of i-layer to 1e15 cm^{-3}.

Chapter 4: Fabrication, Characterization and Evaluation of GaN/Sapphire and GaN/GaN P-I-N Devices

For this study, all three GaN p-i-n structures were grown epitaxially by metal organic chemical vapor deposition (MOCVD). Devices were fabricated using standard photolithography, plasma etching, and metallization techniques. A mask set with multiple diagnostic structures was designed to investigate the device performance and determine pathways for improvement. CLTM (circular line transmission method) diagnostics structures were also characterized to determine the specific contact resistivity of the ohmic contacts to both n-GaN and p-GaN layers.

4.1 Growth of GaN Structures

We collaborated with SUNY-Albany and Adroit for the growth of GaN p-i-n structures. Figure 4.1 shows the epi-layer structure details for all three GaN wafers.

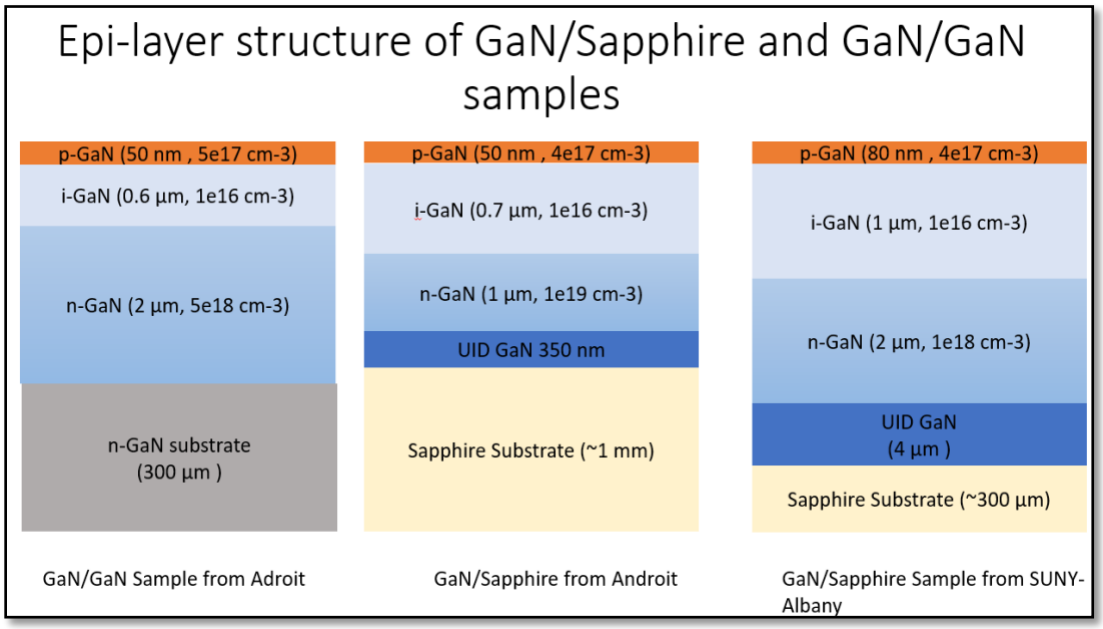

Figure 4.1: Epi-layer structure of three GaN wafers. Higher doping concentration in P and N layers reduce series resistance in the device. Low doping concentration is desired for the i-GaN layer to maximize charge collection area (depletion region).

All three samples were grown using a MOCVD reactor. Two samples consisted of active GaN films grown on top of a 2-inch sapphire (Al_2O_3) substrate and a third sample consisted of active GaN films grown on top of a 1-inch bulk GaN substrate. GaN films grown on top of a sapphire substrate provide a cheaper alternative to growing them on bulk GaN substrates, but due to thermal and lattice mismatch, epitaxial GaN films grown on sapphire usually result in a high density of threading dislocations, V-shaped defects, and stacking faults as illustrated in figure 4.2. These crystalline defects can act as shunt pathways [77] that increase leakage current and non-radiative recombination centers [78] that degrade minority carrier lifetimes. The high dislocation density is moderated by growing a thick GaN buffer layer (UID n-GaN template) on top of sapphire substrate before growing the active GaN films.

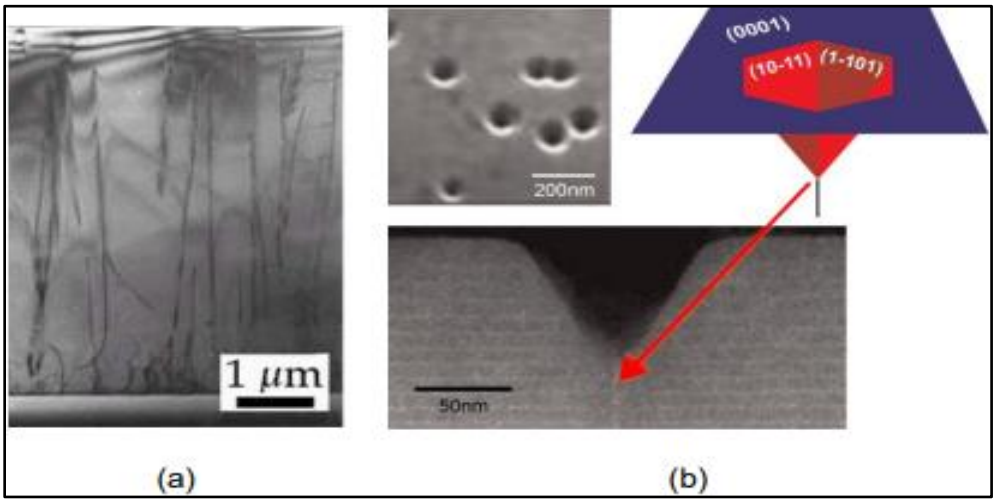

Figure 4.2: a) Cross-section TEM image of GaN film grown on sapphire substrate displaying threading dislocations [1], b) planar scanning electron microscopy (SEM) view, cross-section TEM image, and schematic structure of V defect [78]

All three samples were doped similarly to achieve p-type and n-type carrier concentrations. The unintentionally doped GaN was doped with magnesium to achieve the p-type carrier concentrations, and with silicon for n-type carrier concentrations. An intrinsic layer with a doping concentration of 1e16 cm^{-3} was grown on all three GaN

wafers. The p-type dopants were activated using a rapid thermal anneal at 600 ºC for 10 minutes to remove the H atoms that were weakly bonded to the Mg atoms in all three samples.

4.2 Fabrication Process Sequence

A mask set was designed to fabricate devices on all three GaN wafers. The mask set was designed using the AutoCAD software and was printed on a 5"x5" quartz photomask blank coated with chromium and photoresist (PR). The total pattern dimension was designed to pattern $1/4^{th}$ of a 1-inch diameter sample because our most expensive sample (GaN/GaN) was only 1 inch in diameter, and we wanted to utilize every bit of the real estate on that by making two cuts to get 4 quadrant pieces. The designed mask set included 25 devices with various sizes (.09 mm^2, .16 mm^2, .25 mm^2, 1 mm^2, 4 mm^2, 9 mm^2 and 16 mm^2) and grid-spacing values ranging from 100 to 290 μm. Figure 4.4 shows the mask layout.

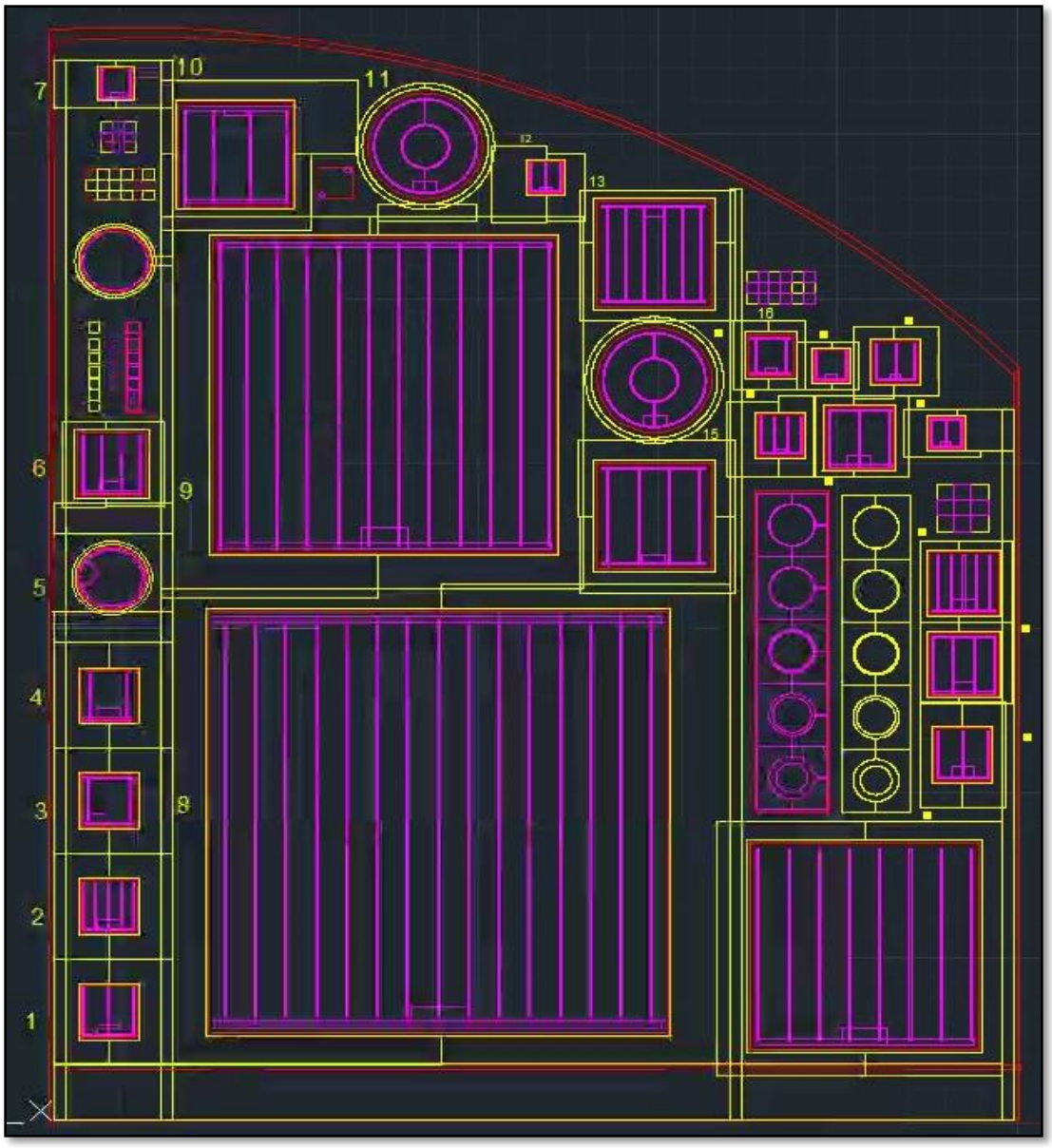

Figure 4.3: Mask Layout design for the fabrication GaN p-i-n devices.

The red features represent the mesa structure, the pink features represent the p-type metal, and the yellow features represent the n-type contact. The mask layout also contains various diagnostic structures including circular transmission line method (CTLM), metal-resistance measurement and schottky diodes for capacitance-voltage

measurements. The devices with different sizes and geometries were designed to determine the best performing devices.

The two GaN/Sapphire samples were diced into 1 cm^2 pieces and a 1-inch GaN/GaN sample was diced into 1/4th of an inch pieces using an automated dicing saw. The samples were cleaned with three baths of acetone/IPA before fabrication in a class 100 cleanroom using standard photolithography, dry etching, metal deposition, and lift-off techniques. Figure 4.4 illustrates our fabrication process sequence.

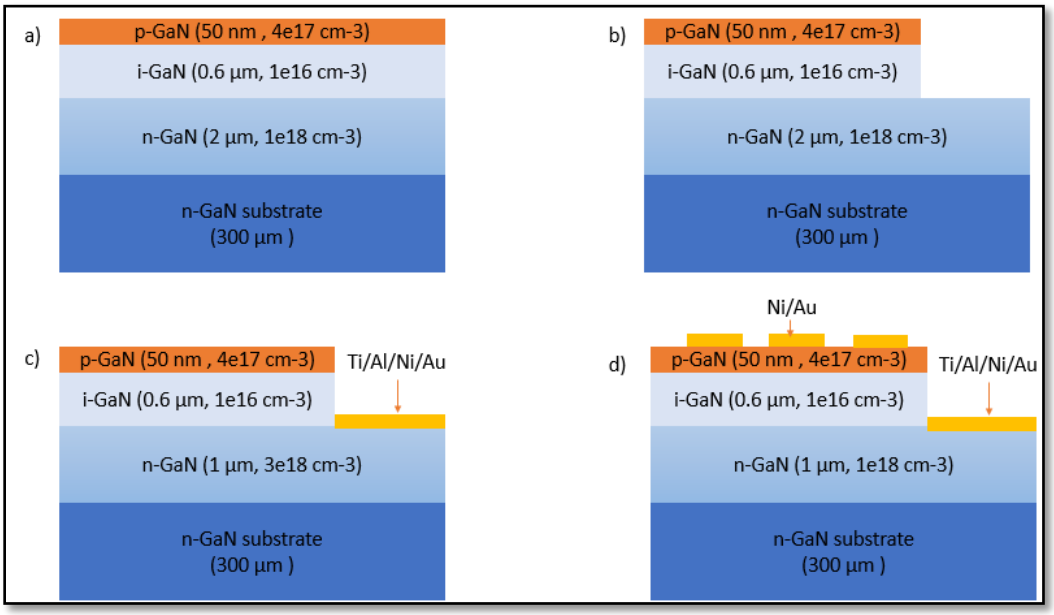

Figure 4.4: Schematic of the fabrication process: a) As-grown GaN p-i-n structure, b) mesa etch, c) n-type metal deposition, d) p-type metal deposition.

First, a mesa pattern is formed by photolithography on the p-i-n structure to define the mesa. The photoresist (PR) layer, cured at 80°C for 5 minutes to harden it, serves as a mask for the pattern transfer. The mesa structure is transferred via inductively coupled plasma (ICP) etching using a BCl_3 /Cl_2 plasma chemistry to expose the n layer (Figure 4.4(b)). The pattern transfer requires dry etching due to the high chemical stability and the high bond strength of nitride semiconductors. Next, the n-

ohmic contact, which consists of titanium/aluminum/nickel/gold (Ti/Al/Ni/Au 30/100/30/50 nm), is formed by photolithography and electron-beam evaporation (Figure 4.4(c)). Prior to the metallization, the sample is dipped in Hydrochloric acid (HCl) for 30 s to etch native oxides. After another photolithography step and a hydrochloric acid (HCl) treatment, a layer consisting of nickel/gold (Ni/Au 5/50 nm) is deposited on the p layer to form p-contact metal schemes by electron-beam evaporation (Figure 4.4(d)).

Figure 4.5 shows a top-view image of a fabricated 4x4 mm device. Next, these devices were wire bonded to a package with thin Au wires using a wire bonder. Figure 4.5b shows the image of the wire-bonded and packaged device. All the n-type contacts are shorted with each other and then connected to one of the pads on the package. All the p-type contacts are wire bonded directly to a unique pin on the package.

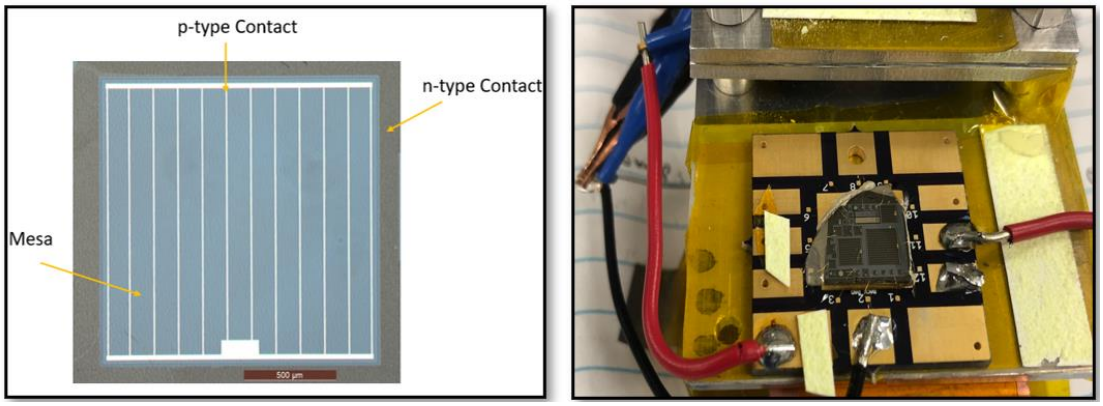

Figure 4.5: Optical Microscope Image of a fabricated Device (left), Wire-bonded and packaged device (right).

4.3 CTLM Characterization of Ohmic Contacts on GaN

Ohmic-contact formation to n-type and p-type GaN films is a critical step for the fabrication of GaN p-i-n devices. Both n and p-type contact resistances need to be minimized for optimal performance of GaN devices. While n-type ohmic contacts with suitable resistances < 10^{-5} Ω-cm^2 have been successfully achieved [79], satisfactory p-type contacts are challenging. This is because it is difficult to increase the doping of p-GaN layer (> $5x10^{-17}$) [80-81], and the work function (~ 6.6 eV) [79] of p-GaN is higher than the work function of any pure metals. Due to these two reasons, it is a challenge to form ohmic contacts to p-GaN layer with minimum resistances.

The metal-semiconductor contact can be characterized using the circular transmission line model (CTLM), as shown in Figure 4.6a. CTLM pattern consists of a conductive (metal) inner region of radius r, a gap of width d (semiconductor), and a conducting outer region of radius R. The test structure is designed with a constant outer radius R = 200 μm and gap d = 4, 8, 16, 32, and 64 μm. The total resistance R_t between the internal and the external contacts is given by

$$R_t = \frac{V}{I} = \frac{R_{sh}}{2\pi}\left[ln\left(\frac{R}{r}\right) + L_t\left(\frac{1}{R} + \frac{1}{r}\right)\right] \quad r >> 4\ L_t \qquad (4.1)$$

where R_{sh} is the sheet resistance (Ω/cm^2) of the semiconductor layer and L_t is the transfer length (cm) [82-83]. Equation 5.1 is only valid for r >> 4 Lt. Figure 4.6b shows the plot of the total resistance measured for various gap values as a function of ln(R/r). The data can then be fitted to obtain a straight-line plot of R_t vs. ln(R/r). The slope of the linear regression leads to R_{sh} and the intercept at ln(R/r) = 0 (corresponding to R =

r) is $R_{sh} \cdot L_t / R\pi$, giving Lt. The specific contact resistivity, ρc ($\Omega \cdot cm^2$), can be obtained using the following equation:

$$L_t = \sqrt{\frac{\rho c}{R_{sh}}} \qquad (4.2)$$

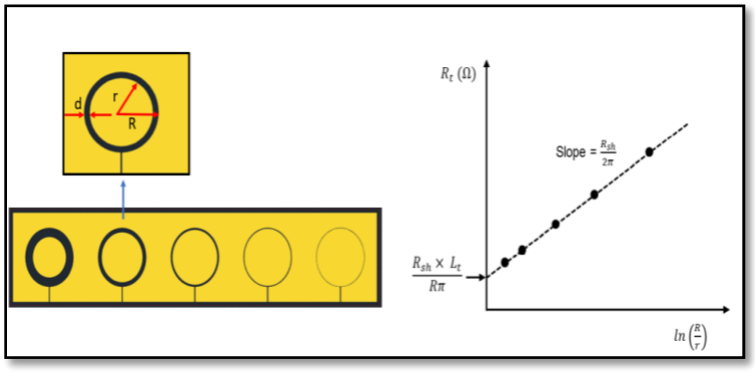

Figure 4.6: (a) Circular contact resistance patterns with various gap (d) values. The yellow regions represent metallic regions. (b) plot of the total resistance as a function of ln(R/r) [5].

4.3.1 Ohmic Contacts to n-GaN:

A metal stack layer consisting of Ti/Al/Ni/Au was deposited followed by anneal under N_2 gas at 750°C for 30 s to form ohmic contacts to n-GaN layer. The IV measurements were carried out on the CLTM structures to determine the specific contact resistivity ρc, transfer length L_t, and sheet resistance of the n-GaN layer.

The IV characteristics of the CTLM patterns on n-GaN, shown in Figure 4.7(a), exhibit a linear behavior, indicating that the metal contacts are ohmic. To calculate ρc, the total resistance R_t, extracted from the IV characteristics, is plotted as a function of ln(R/r) as illustrated in Figure 4.6(b) [82-83]. Using equations (4.1) and (4.2), ρc and L_t were determined to be ~2.13e-5 $\Omega \cdot cm^2$ and ~ 6 μm, respectively. The sheet resistance of the n-GaN epilayer was calculated to be ~59 Ω/cm^2. These low-resistance ohmic

contacts to n-GaN are in agreement with what is reported in the literature for MOCVD grown n-GaN films [84-85].

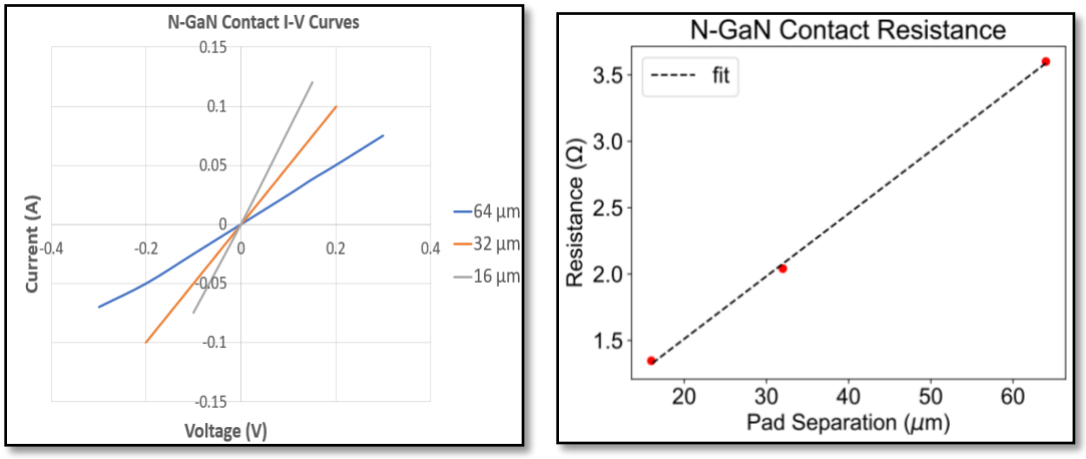

Figure 4.7: (a) CTLM I-V characteristics of annealed Ti/Al/Ni/Au) ohmic contacts to n-GaN. (b) Resistance as a function of pad separation distance (µm). The experimental data points are fitted using linear regression (dotted line) to determine the specific contact resistivity.

4.3.2 Ohmic Contacts to p-GaN:

A metal stack layer consisting of Ni/Au was deposited on the p-GaN layer followed by anneal in O_2 environment at 600 °C for 600 s to form ohmic contacts to p-GaN layer. The IV characteristics of the CTLM patterns, shown in Figure 4.8(a), exhibit a linear behavior, indicating that the metal contacts are ohmic. The ρc and Lt were determined to be ~ 0.64 Ω·cm2 and 3.60 µm, respectively. The p-contact resistance is a magnitude higher than what is reported in the literature for MOCVD grown p-GaN films [86-87]. While this contact resistivity is acceptable for betavoltaic device operation, a more detailed study is needed to optimize the annealing conditions to obtain low-resistance ohmic contact to p-GaN.

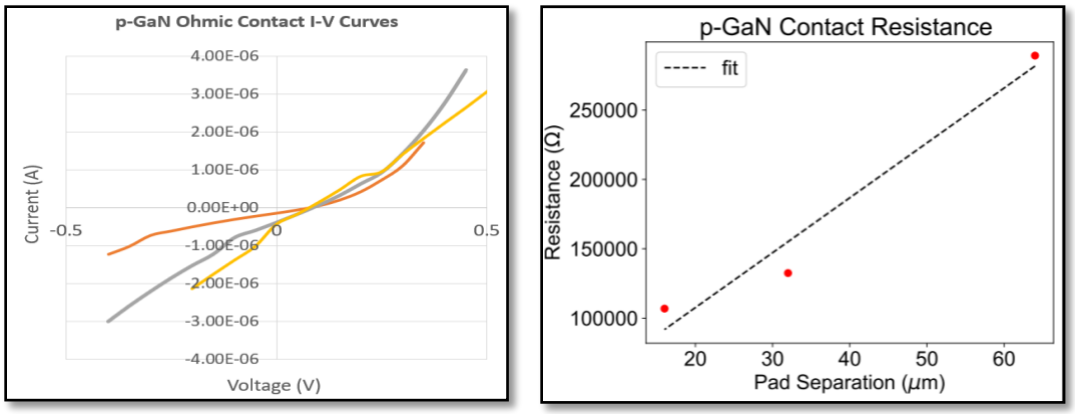

Figure 4.8: a) CTLM I-V characteristics of annealed Ni/Au ohmic contacts to p-GaN. (b) Resistance as a function of pad separation distance (μm). The experimental data points are fitted using linear regression (dotted line) to determine the specific contact resistivity.

Chapter 5: Characterization and Evaluation of GaN/Sapphire and GaN/GaN P-i-N Devices for Betavoltaic Energy Conversion

Both GaN/Sapphire and GaN/GaN p-i-n devices were characterized using current - voltage (IV) measurements in the dark (without any external beta, alpha or photon stimulus) and then under UV light source (365 nm, 180 mW/cm^2). These devices were tested under a monoenergetic electron to mimic their performance under ^{3}H and Ni-63 beta sources. With the help of monoenergetic electron beam, we were able to confirm the effective charge collection area in each of these wafers, as predicted by TCAD simulations.

5.1 Current-Voltage (I-V) Measurements in the Dark

The fundamental component of a betavoltaic device is the semiconductor diode which converts the kinetic energy of beta particles into electrical energy. The dark IV measurement at room temperature is one of the most straight forward methods to determine fundamental performance parameters of a device such as series resistance, shunt resistance, leakage current density among others. Dark I-V measurements inject carriers into the circuit with electrical means rather than with light/beta generated carriers. In most cases the two are equivalent, and the dark IV measurements are reproducible whereas small fluctuation in the intensity of photons/beta particles can add considerable noise to the system making it difficult to reproduce data. Therefore, dark IV measurements are preferred for examining the diode properties.

We performed current – voltage (IV) measurement using a Keithley semiconductor parameter analyzer. The devices were tested by sweeping the voltage from -5 V to 5 V to generate IV curves revealing their operation in both forward bias

and reverse bias. The current compliance was set at 50 mA to avoid destruction of devices through heating in the forward bias and destructive breakdown in the reverse bias. We extracted the following fundamental parameters from the IV curves: Turn on Voltage, Series Resistance, Shunt Resistance and Leakage (reverse saturation) current density. An example of how we extracted these parameters from the IV curves is shown in figure 5.1.

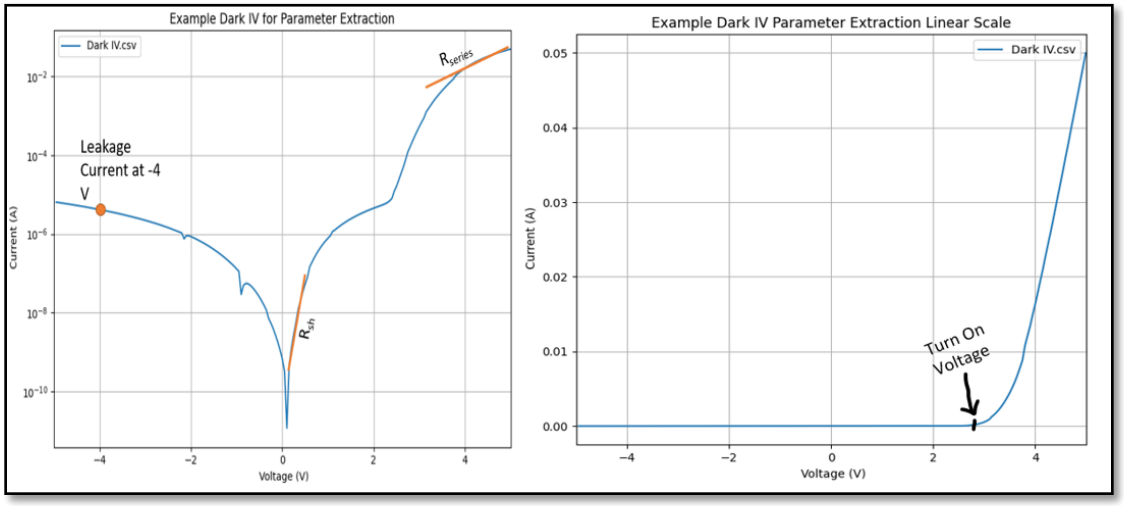

Figure 5.1: Demonstration of how we extracted parameters from the dark IV curves. Series and shunt resistances were calculating by finding the slope of the of the line in those regions in the semi-log IV (left). Turn on voltage was determined from IV curve (right). The current value at -4 V was used to find the leakage current density by considering the device area.

5.1.1 Turn on Voltage

The turn on voltage (also called threshold voltage (Vth)) is defined as the voltage at which the tangent to the IV curve in the "linear" region intercepts the voltage axis or simply the voltage at which the diode starts to conduct current in forward bias. In an ideal diode, a turn on voltage should match the electronic bandgap of a semiconductor (~ 3.4 V for GaN) but it is usually lower than the electronic bandgap due to series/shunt resistances present in the diode, recombination in the depletion

region, and due to an additional lower energy barrier (such as Schottky diode for non-ohmic contacts) in parallel with the p-i-n device.

5.1.2 Series Resistance

Series resistance is caused by three main mechanisms: 1) the contact resistance between the metal contact and the semiconductor; 2) the resistance of the semiconductor top surface; and 3) the resistance of the metal contacts to p and n-type layers (negligible in most cases). The main impact of series resistance is to reduce the fill factor by lowering the open circuit voltage, although excessively high values may also reduce the short-circuit current.

The simplest way to calculate series resistance (R_s) is to do a linear fit to the IV curve in the forward conduction mode as shown in figure 5.1, and the slope of that line is the R_s.

$$R_s = \frac{dV}{dI} \ @ \ V \gg Vth \qquad (5.1)$$

When $V \gg Vth$, high forward conduction occurs, and we can ignore other resistances except series resistance.

5.1.3 Shunt Resistance

Shunt resistance (also known as parallel resistance) is caused by the presence of unwanted current channels that are parallel to the diode junction. R_{sh} is caused by defects in the material or at the surface, rather than poor device design. It is desirable for a device to have high shunt resistances, so all the current can go through the junction while lowering the short circuit current. R_{sh} can be calculated by using the slope of a IV curve in the region $V \cong 0$, as shown in figure 5.1.

Equation 5.2 shows the relative regimes for calculating the shunt resistance.

$$R_{sh} = \frac{dV}{dI} \text{ @ V} \cong 0$$

The parallel resistance, or shunt resistance, will always be higher than the series resistance in the region $V \cong 0$ and therefore the series resistance can be ignored.

5.1.4 Leakage or Reverse Saturation Current Density

The leakage current is calculated when the diode is in the reverse bias. It is desirable for the diode to have low leakage current in the reverse bias before the junction breakdown. High leakage current can be caused by tunneling through defects in the p-n junction.

5.1.5 Dark IV Curves and Discussion on Results

Figure 5.2-5.4 shows the dark IV curves (both in linear and log scale) of the devices fabricated on SUNY grown GaN/Sapphire (SGS) structure, Adroit grown GaN/Sapphire (AGS) structure and Adroit grown GaN/GaN (AGG) structure, respectively. Table 5.1 – 5.3 shows their extracted parameters: turn on voltage, series resistance, shunt resistance, and reverse saturation current density.

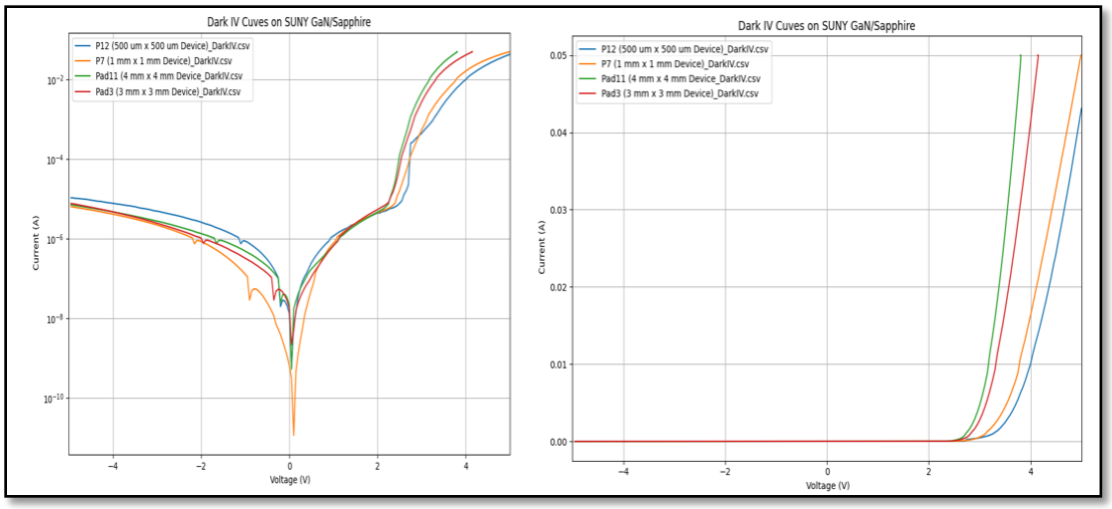

Figure 5.2: Dark IV curves on the SGS sample: log IV characteristics(left) and IV characteristics (right). Note: small peaks observed on the log IV in the reverse direction are due to instrument artifacts

Table 5.5: Parameters extracted from SGS device dark IV curves

SUNY GaN/Sapphire

Device #	Size (cm^2)	Shunt Resistance (ohm-cm^2)	Series Resistance (ohm-cm^2)	Leakage Current density at -4 V (Amps/cm2)	Turn on Voltage (V)
P12	0.00025	1.02E08	0.09	-1.70E+00	3.06
P7	0.01	3.36E+06	0.31	-3.97E-01	2.70
P3	0.09	3.49E+6	1.74	- 2.89E-02	2.52
P11	0.16	5.40E+6	2.76	-1.71E-02	2.46

SUNY GaN/Sapphire (SGS) devices have a turn on voltage between 2.46 V and 3.06 V which is reasonable for GaN p-i-n devices. The turn on voltage decreases in all devices as the device size increases. This happens because the series resistance is increasing with the increase in device size, thus lowering the turn on voltage. We also observed an increase in series resistance and decrease in shunt resistance with the increase in device size due to probability of higher density of defects (dislocations defects, nitrogen vacancies etc) in larger devices. All these devices have low series

resistance and high shunt resistance (10^6), exhibiting good quality wide bandgap diodes.

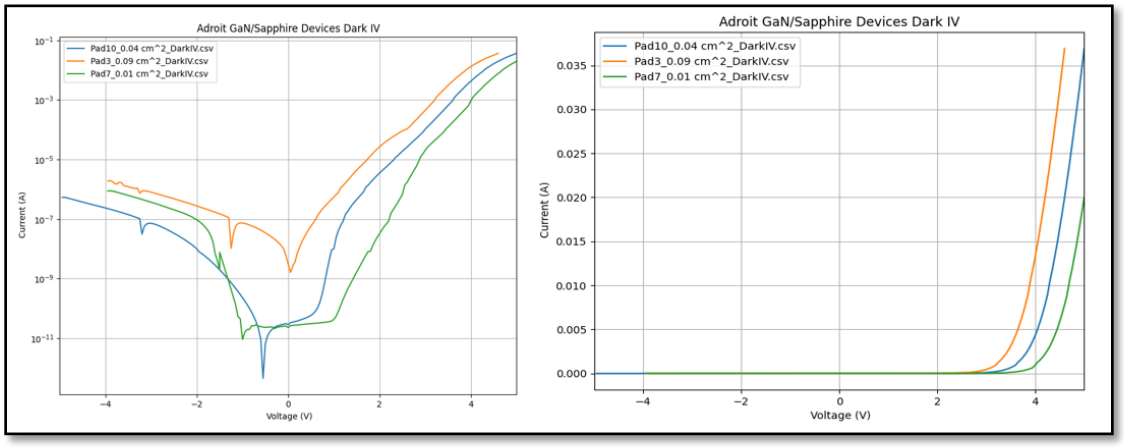

Figure 5.3: Dark IV curves on the AGS devices: semi-log IV characteristics (left) and IV characteristics (right). Small peaks in the reverse direction in the log IV are due to instrument artifacts.

Table 5.6: Parameters extracted from AGS device dark IV curves.

Dark IV Androit GaN/Sapphire Devices

Device #	Size (cm^2)	Shunt Resistance (ohm-cm^2)	Series Resistance (ohm-cm^2)	Leakage Current at -4 V (Amps/cm^2)	Turn on Voltage (V)
Pad 7	0.01	1.11E+07	2.55	-5.95E-02	3.19
Pad 10	0.04	9.80E+06	2.68	-3.69E-03	3.03
Pad 3	0.09	2.16E+06	3.32	-8.96E-03	2.87

Adroit GaN/Sapphire (AGS) devices have a turn on voltage (between 2.87 V and 3.19 V) which is even higher than SGS devices and it decreases as the device size increases. We believe the turn on voltage is higher in AGS devices due to lower series resistance because of higher doping concentrations in both p and n layers, compared to SGS devices. Similarly, we observe an increase in series resistance and decrease in the shunt resistance as the device size is increased for the same reasons mentioned above for the SGS devices.

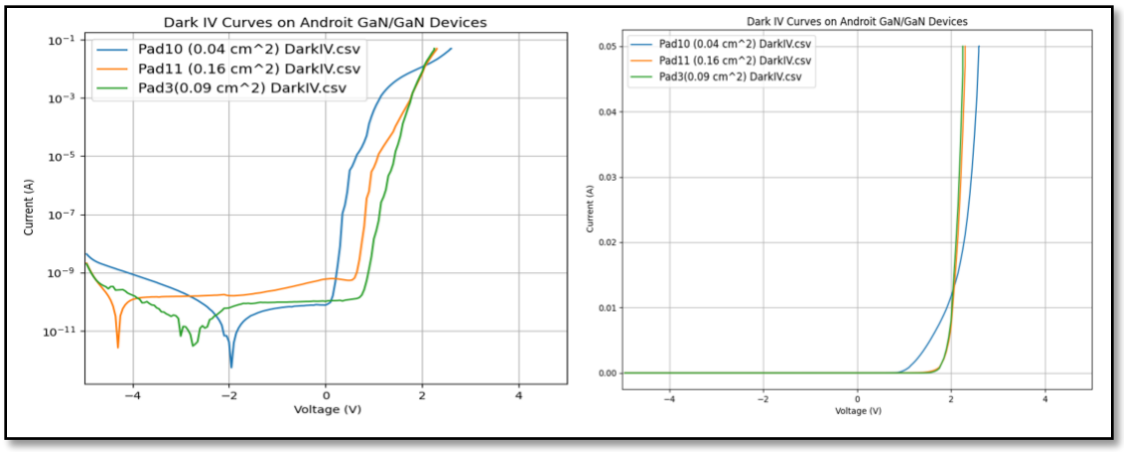

Figure 5.4: Dark IV curves on AGG devices: log IV characteristics (left) and IV (right). Small peaks in the reverse direction in the log IV are due to instrument artifacts. An extra annealing (600 °C) step increased the threshold voltage.

Table 5.3: Parameters extracted from AGG Device Dark I-V curves.

Androit GaN/GaN Devices

Device #	Size (cm^2)	Shunt Resistance (ohm-cm^2)	Series Resistance (ohm-cm^2)	Leakage Current at -4 V (Amps/cm^2)	Turn on Voltage (V)
Pad 10	0.04	5.22E+08	6.04	-2.17E-02	0.83
Pad 3	0.09	1.05E+10	1.032	-1.86E-03	1.50
Pad 11	0.16	3.33E+10	1.84	7.38E-04	1.40

Adroit GaN/GaN (AGG) devices have a low turn on voltage (between 0.83 V and 1.50 V) compared to AGS and SGS devices. We believe the lower turn on voltage could be associated with traps/point defects in the material. Initially when we fabricated AGG devices, their turn on voltage was even lower (pad 10), and after annealing it at 600 °C for 10 mins, the turn on voltage improved (pad 3 and pad 11). We further annealed the AGG sample at higher temperatures (700 °C and 750 °C) to anneal out more traps/defects in the material, but it did not improve the turn on voltage further. Both series and shunt resistances are reasonable for these devices and have a low leakage current density compared to SGS and AGS devices.

5.2 IV Measurements under the UV light Source (flashlight)

Since the working principle of a betavoltaic device is like a photovoltaic device, we selected one device each from the three GaN wafers and exposed them with a UV light source (365 nm) to see how well they respond to photons. These measurements were taken similarly to the dark IV measurements, but a UV light source was incident on the devices when the voltage sweep was performed. The data for the IV curves was generated using the automated Keithley semiconductor parameter analyzer.

Figure 5.5 shows the UV flashlight IV curves (both in linear and log scale) for one device from all three GaN wafers, and Table 4.4 shows the extracted parameters.

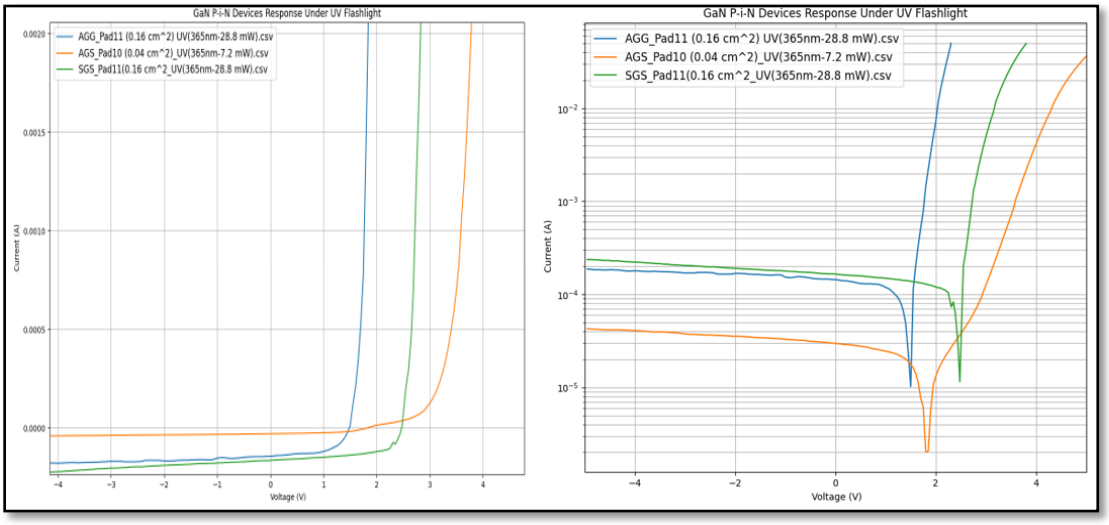

Figure 5.5: IV currents measured under the UV light source: log IV characteristics (right) and IV characteristics (left).

With the presence of photon stimulus from UV light, IV curves dropped down into the fourth quadrant indicating that the devices are generating power. When the current is plotted in log IV as shown in figure 5.5 (right), we can see a clear shift in the V_{oc} (up and to the right) of all three devices. The shift in V_{oc} is due to photon stimulating the device and generating the electrical power.

Table 5.7: Parameters extracted from UV light source (flash light) IV Curves.

GaN P-i-N Devices UV Flashlight Response

Wafer and Device #	Size (cm^2)	Voc	Isc	MPP	FF	Efficiency (%)
AGS_Pad 10	0.04	1.80	2.97E-05	7.00e-4/cm^2	0.53	0.39
AGG_Pad 11	0.16	1.5	1.44E-4	7.63e-4/cm^2	0.57	0.42
SGS_Pad 11	0.16	2.48	2.0E-4	1.54e-3/cm^2	0.600	0.85

Table 5.4 shows the extracted parameters from the IV curves under photon stimulus for all three devices. The input power of the UV light was fixed at 180 mW/cm^2 with a wavelength of 365 nm. The MPP (maximum power point) for each device was calculated using equations 5.3 and 5.4.

$$P_{max} = V_m * I_m \qquad (5.3)$$

$$\eta = \frac{P_{out}}{P_{in}} \qquad (5.4)$$

MPPs of 1.54 mW/cm^2, 0.763 mW/cm^2, and 0.7 mW/cm^2 with an overall efficiency of 0.85 %, 0.42 % and 0.39 % were calculated for SGS, AGG and AGS devices, respectively.

The fill factor (FF) of these devices was calculated using equation 5.5.

$$FF = \frac{V_m I_m}{V_{oc} I_{sc}} \qquad (5.5)$$

The fill factor (FF) of 0.60, 0.57 and 0.53 was calculated for SGS, AGG and AGS devices, respectively. FF is a parameter which, in conjunction with V_{oc} and I_{sc}, determines the maximum power from a photovoltaic device. V_m and I_m are the voltage and current at the maximum operating point of the device, respectively. SGS device has a higher V_{oc} compared to other two devices, thus its MPP and FF are greater than the other two devices as well. We expected the V_{oc} of the AGS device to be higher than 1.80 V shown here under photon stimulus because this device had a turn on voltage of

3.03 V in the dark mode. On the other hand, we see a higher V_{oc} in AGG device from the turn on voltage in the dark mode.

5.3 IV Measurements under the monoenergetic Electron Beam

We used a monoenergetic electron beam to test GaN devices to simulate their performance under real beta sources. The monochromatic electron beam's input current was fixed at 1 nA (500 mCi) and the voltage of it was varied from 3 kV up to 16 kV with a step size of 1 kV. These measurements were taken similarly to the UV light measurements, but an electron beam stimulus was used instead of a UV light source for device stimulation. An external semiconductor analyzer generated the IV curves as the electron beam was incident on the device. By doing this, we were able to simulate the behavior of these devices for ^{3}H and ^{63}Ni beta sources and validate the effective charge collection area in each of these three devices, as predicted by TCAD modeling.

Figures 5.6 – 5.8 show the IV curves generated, as the electron beam was incident on the SGS, AGS and AGG devices, respectively. Table 5.5 – 5.8 show the

parameters extracted from the IV curves such as V_{oc}, I_{sc}, MPP, FF, and overall efficiency of the devices.

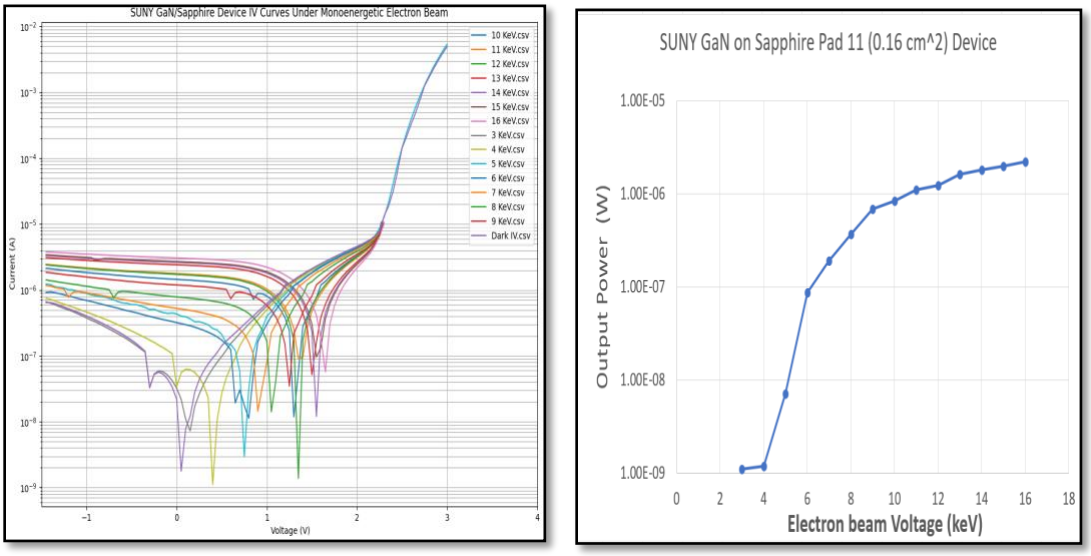

Figure 5.6: SGS device characterization under electron beam stimulus: log IV curves (left) and output power (right) as a function of incident beam energy of the electron beam

Table 5.8: Parameters extracted from the IV curves of SGS device under the monoenergetic electron beam stimulus.

SUNY GaN/Sapphire Pad 11 (0.16 cm^2)

E-Beam Energy (keV)	Voc (V)	Isc (A)	MPP (W)	FF	Pin (W)	Eff (%)
3	0.15	2.18E-08	1.09E-09	0.33394	3.00E-06	0.0364
4	0.4	3.40E-08	1.17E-09	0.36213	4.00E-06	0.0293
5	0.75002	3.99E-07	7.09E-09	0.37013	5.00E-06	0.142
6	0.79984	3.08E-07	8.73E-08	0.35417	6.00E-06	1.46
7	0.9	5.14E-07	1.91E-07	0.41375	7.00E-06	2.73
8	1.0499	7.73E-07	3.69E-07	0.45476	8.00E-06	4.61
9	1.25	1.18E-06	6.89E-07	0.46698	9.00E-06	7.65
10	1.3	1.43E-06	8.33E-07	0.44817	1.00E-05	8.33
11	1.35	1.76E-06	1.10E-06	0.46149	1.10E-05	9.97
12	1.43	1.81E-06	1.24E-06	0.44921	1.20E-05	10.3
13	1.5	2.39E-06	1.62E-06	0.45188	1.30E-05	12.5
14	1.55	2.60E-06	1.81E-06	0.44802	1.40E-05	12.9
15	1.58	2.68E-06	1.98E-06	0.45282	1.50E-05	13.2
16	1.65	3.04E-06	2.21E-06	0.45509	1.60E-05	13.8

Figure 5.6 (left) shows the IV curves from the SGS device under the monoenergetic electron beam stimulus. The MPP of the device is calculated at each

step size and is plotted in 5.6b. The efficiency, V_{oc} and I_{sc} were also calculated at each step size for all three devices. We observed that the V_{oc}, I_{sc}, MPP and efficiency of the device continuously increased as the electron-beam energy was increased. This is because more EHPs are created in the device as the input power of the electron beam is increased. EHPs are collected throughout the penetration depth of the electron beam, thus increasing the output power and efficiency of the device.

The MPP at 6 keV (87.3 nW with an efficiency of 1.46 %) and 16 keV (2.21 µW with an efficiency of 13.8 %) represents the average energy emission for beta sources ^{3}H and Ni^{63}, respectively. Our electron beam system has a maximum setting of 16 keV, and the output power and efficiency simulating Ni^{63} was calculated at the incident beam energy of 16 keV instead of 17 keV.

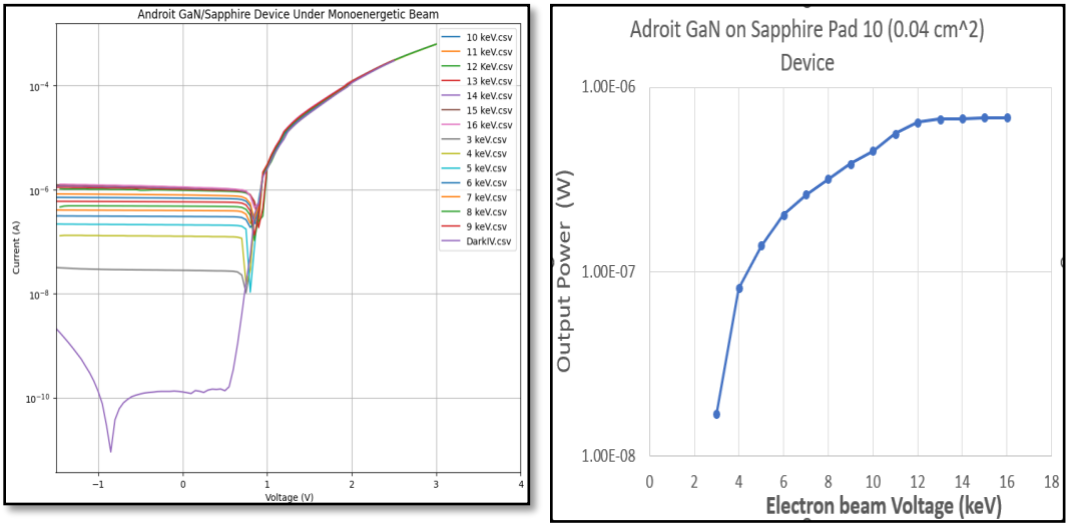

Figure 5.7: AGS device characterization under electron beam stimulus: log IV curves (left) and output power (right) as a function of incident beam energy of the electron beam

Table 5.9: Parameters extracted from the IV curves of AGS device under the monoenergetic electron beam stimulus.

Adroit GaN/GaN Pad 11 (0.16 cm^2)						
E-Beam Energy (keV)	Voc (V)	Isc (A)	MPP (W)	FF	Pin (µW)	Eff (%)
3	0.8	2.13E-07	1.21E-07	0.44921	3.00E-06	4.03
4	0.84	4.85E-07	1.64E-07	0.45282	4.00E-06	4.10
5	0.85	4.24E-07	2.02E-07	0.44059	5.00E-06	4.04
6	0.85	5.85E-07	2.58E-07	0.44802	6.00E-06	4.30
7	0.85	6.22E-07	3.08E-07	0.45188	7.00E-06	4.40
8	0.85	5.56E-07	3.50E-07	0.46149	8.00E-06	4.38
9	0.85	5.62E-07	3.97E-07	0.44817	9.00E-06	4.41
10	0.899	4.51E-07	4.10E-07	0.45476	1.00E-05	4.10
11	0.85	3.01E-07	4.23E-07	0.46698	1.10E-05	3.85
12	0.85	5.96E-07	4.50E-07	0.41375	1.20E-05	3.75
13	0.85	6.22E-07	4.70E-07	0.4103	1.30E-05	3.62
14	0.85	5.45E-07	4.80E-07	0.41213	1.40E-05	3.43
15	0.85	5.49E-07	4.83E-07	0.33394	1.50E-05	3.22
16	0.85	2.13E-07	4.86E-07	0.37013	1.60E-05	3.04

Figure 5.7 (left) shows the IV curves from the AGS device under the monoenergetic electron beam, and MPP calculated at each step size is shown in figure 5.7b. We observed that the V_{oc}, I_{sc}, MPP and efficiency of the device continuously increased until 12 keV and then reached saturation. This is because more EHPs are created in the device as the input power of the electron beam is increased beyond 12

KeV, but they are created outside the charge collection region where they are not collected.

The MPP at 6 keV (139 nW with an efficiency of 3.40 %) and 16 keV (686 nW with an efficiency of 4.29 %) represents the average energy emission for beta sources ^{3}H and Ni^{63}, respectively.

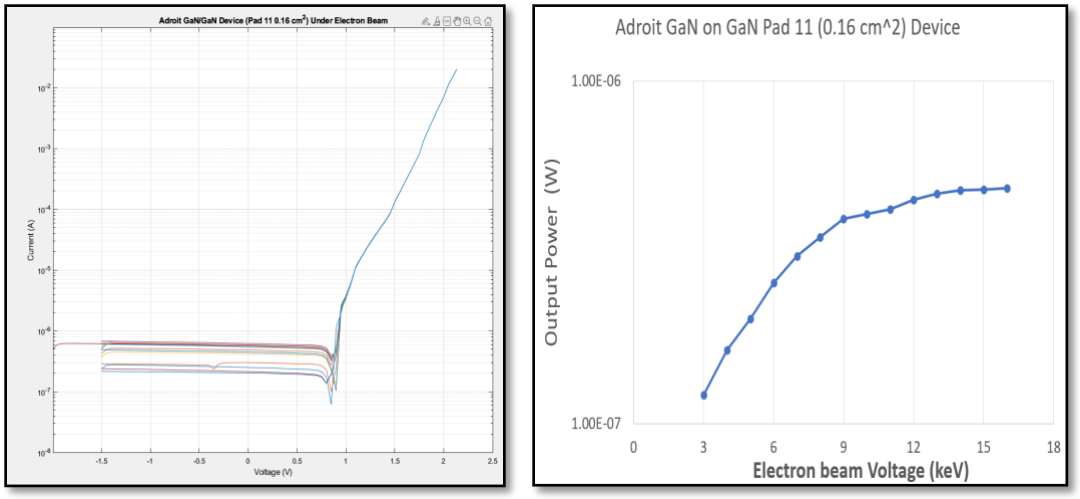

Figure 5.8: AGG device characterization under electron beam stimulus: log IV curves (left) and output power (right) as a function of incident beam energy of the electron beam

Table 5.7: Parameters extracted from the IV curves of AGG device under the monoenergetic electron beam stimulus.

Adroit GaN/GaN Pad 11 (0.16 cm^2)						
E-Beam Energy (keV)	Voc (V)	Isc (A)	MPP (W)	FF	Pin (μW)	Eff (%)
3	0.8	2.13E-07	1.21E-07	0.44921	3	4.03
4	0.84	4.85E-07	1.64E-07	0.45282	4	4.10
5	0.85	4.24E-07	2.02E-07	0.44059	5	4.04
6	0.85	5.85E-07	2.58E-07	0.44802	6	4.30
7	0.85	6.22E-07	3.12E-07	0.45188	7	4.46
8	0.85	5.56E-07	3.50E-07	0.46149	8	4.38
9	0.85	5.62E-07	3.97E-07	0.44817	9	4.41
10	0.899	4.51E-07	4.10E-07	0.45476	10	4.10
11	0.85	3.01E-07	4.23E-07	0.46698	11	3.85
12	0.85	5.96E-07	4.50E-07	0.41375	12	3.75
13	0.85	6.22E-07	4.70E-07	0.41030	13	3.62
14	0.85	5.45E-07	4.80E-07	0.41213	14	3.43
15	0.85	5.49E-07	4.83E-07	0.33394	15	3.22
16	0.85	2.13E-07	4.86E-07	0.37013	16	3.04

Figure 5.8 (left) shows the IV curves from the AGG device under the monoenergetic electron beam stimulus, and MPP calculated at each step size is shown in figure 5.8b. In this device, we see a continuous increase in the V_{oc}, I_{sc}, MPP and efficiency of the device until ~ 9 keV and then the efficiency starts to slowly decline.

The MPP at 6 keV (258 nW with an efficiency of 4.30 %) and 16 keV (486 nW with an efficiency of 3.04 %) represents the average energy emission for beta sources ^{3}H and Ni^{63}, respectively.

5.3.1 Discussion on the Electron Beam Results

Figure 5.9 shows the MPP and efficiency of all three GaN devices as a function of input energy of the electron beam. The effective charge collection area in each device is marked by the arrows, predicted by TCAD modeling results in chapter 3.

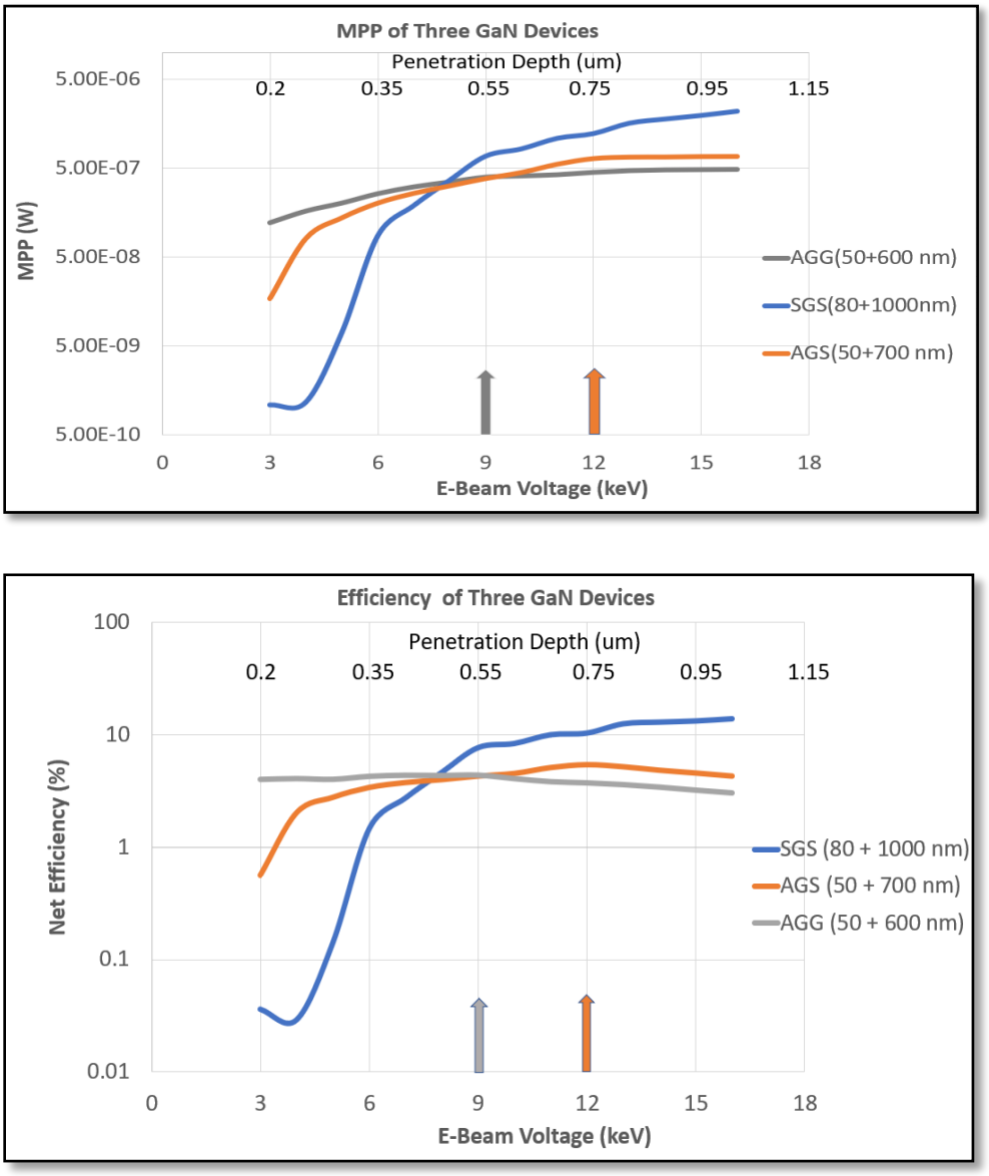

Figure 5.9: Comparison of MPP (top) and Efficiency (bottom) of three GaN p-i-n structures.

AGG has a smaller effective charge collection area of 650 nm compared to AGS (750 nm) and SGS (1.08 µm) devices. Based on our MCNP modeling results, a 9 keV

monoenergetic beam is confined within 650 nm in GaN semiconductor, that is why AGG device has a maximum efficiency taking place at 9 keV. When energy of the electron beam is increased above 9 keV, we observe a slight decrease in efficiency because EHPs created outside the charge collection area are not collected, but output power increases because more EHPs are created within the collection area. Similarly, AGS device has a maximum efficiency taking place at 12 keV because monoenergetic electron beam up to 12 keV is well contained within the collection area of 750 nm. The output power increases for the same reason mentioned above for the AGG device.
For SGS device, the collection area is 1.08 μm and even a 16 keV electron beam does not penetrate deeper than the collection area of this device. This is why we see an increase in efficiency up to the maximum setting of our electron beam at 16 keV. Also, this device has an un-depleted i-region which is less than the minority carrier diffusion length of holes. In addition to that, the difference in the doping concentration of two n layers (n minus layer and n+ layers) create an electric field (back surface field), which helps the collection of minority carriers by pushing them into the depletion region.

Figure 5.10 shows the charge collection efficiency as a function of depth in all three GaN devices. We observe that the charge collection is higher in the i-layer in all three devices and the charge collection percentage drops off after the electron beam penetrates beyond the i-layer thickness in the AGG (0.60 μm) and AGS (0.70 μm). We do not see the charge collection efficiency drop off in the SGS device because even a 16 keV electron beam does not penetrate beyond the i-layer thickness (1 μm) in that device.

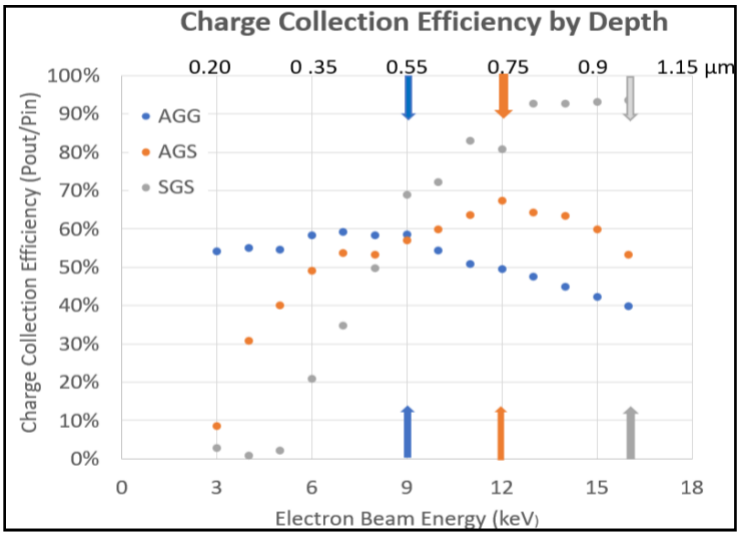

Figure 5.10: Charge Collection Efficiency (CCE) based on MCNP, TCAD and Experimental results. CCE percentage is calculated by determining the # of EHPs created as a function of penetration depth and then diving by the total current measured at that depth using the electron beam.

5.4 Challenges in the Optimization of GaN Betavoltaic Devices

To enhance the performance of GaN based betavoltaic devices, a method must be found to increase the charge collection area. One possibility could be to controllably dope the *i*-layer less than 1 x 10^{16} cm^{-3} but as of today, high quality UID GaN layers still cannot be doped less than 1e16 cm^{-3} without compensation (impurities). Since GaN is a direct bandgap semiconductor, the minority carrier diffusion lengths of electrons (Le) and holes (L_h) do not increase the charge collection area significantly due to shorter Le and L_h. It is reported that L_h is only ~ 100 nm in MOCVD grown Si doped 3e18 cm^{-3} N+ layer.

We proposed a multijunction structure consisting of p-i-n-i-p-i-n GaN layers (n is the bottom layer grown on top of substrate and p is the top layer), as shown in figure 5.11, to increase the charge collection area for high energy beta sources depositing their energy at a depth greater than 1 µm. Figure 5.11c shows the electric field present in the

structure and the width of the charge collection area is ~ 2.4 µm. The electric field is zero in the N+ layer (~0.8 µm to 1~ µm) and at P layer (1.5 µm to 1.65 µm) but since the minority carrier diffusion length of L_h and L_e is greater than the thickness of these layers, the charge collection area is continuous throughout the full 2.4 µm length. Also, the electric field increasing at the junctions helps with the minority carriers' diffusion by pushing them into depletion regions where they are drifted to their respective terminals for collection.

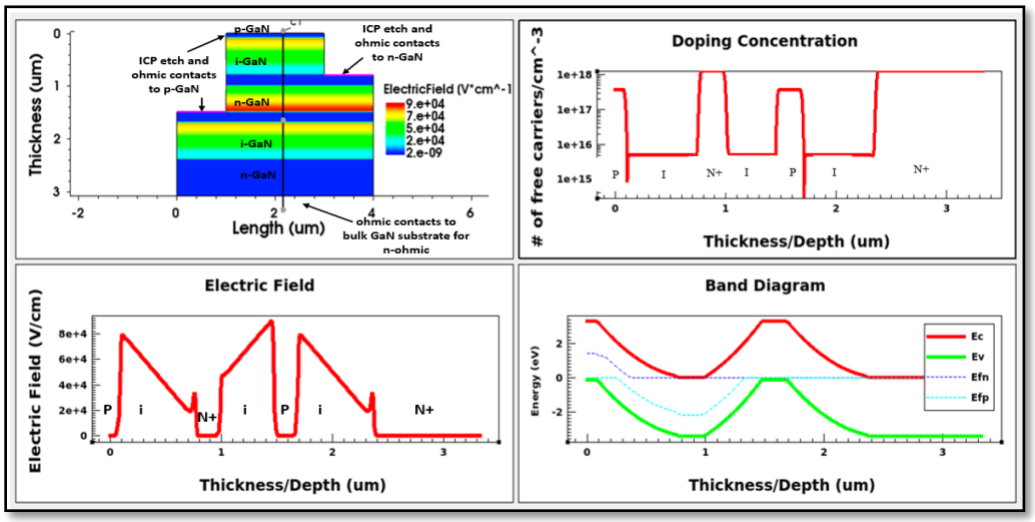

Figure 5.11: Multijunction structure proposed for optimal performance of GaN betavoltaic devices: a) shows the structure grown and fabricated with p-contact and n-contacts. b) doping levels of each layer. c) Electric field throughout the structure. d) Band diagram representation of the structure.

This proposed structure could pose challenges in the fabrication process. For example, it would be a challenge to precisely etch down to p-GaN and n-GaN layers for ohmic contact formation. However, this challenge could be overcome with fine tuning of ICP etch process.

Chapter 6: Characterization and Evaluation of InGaP Devices for Betavoltaic Energy Conversion

In this chapter, we characterized and evaluated InGaP n-i-p devices for a betavoltaic power source. InGaP wafers were grown and fabricated by Microlink. InGaP devices were characterized using current - voltage (IV) measurements in the dark (without any external beta, alpha or photon stimulus) and then under UV light source (365 nm, 180 mW/cm^2). Finally, these devices were tested under monoenergetic energy beams at various energies to simulate their performance under real beta sources.

6.1 Growth and Fabrication Process for InGaP Devices

The InGaP structure, as shown in figure 6.1, was grown on a 6-inch gallium arsenide (GaAs) substrate using a 3×2" Aixtron close-couple showerhead metal organic vapor phase epitaxy (CCS-MOVPE). A buffer layer of 200 nm lightly doped p layer was grown on top of the substrate before growing the InGaP film structure. For InGaP film structure, first a 50 nm p-type (2e18 cm^{-3}) layer was grown. The purpose of this layer is to induce BSF (back surface field) to reduce surface recombination (minority carriers). Next, a p-type base of 1500 nm (5e16 cm^{-3}) was grown, followed by an intrinsic (1e16 cm^{-3}) layer of 10 nm to improve the charge separation at the junction. Finally, a 100 nm si-doped (1.6×10^{18} cm^{-3}) n-layer was grown to complete the InGaP n-i-p structure.

To fabricate these devices, a 20 nm Indium Aluminum Phosphide (InAlP) front window layer was grown to reflect minority holes in the emitter and passivate the device. For p-contact formation, a highly doped GaAs contact layer was used. A double

layer ZnS (56 nm)/MgF (110 nm) was incorporated to minimize the reflection between 400-700 nm [88].

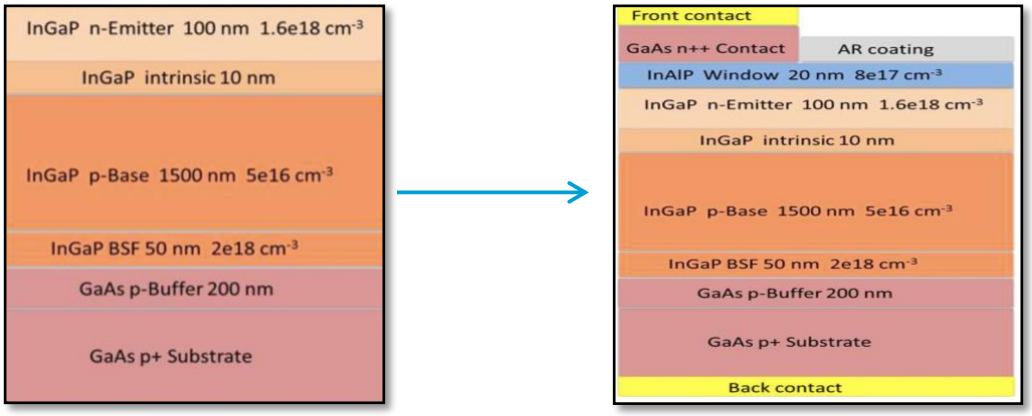

Figure 6.1: Epi-layer structure of grown InGaP n-i-p wafer (left) and after fabrication (right)

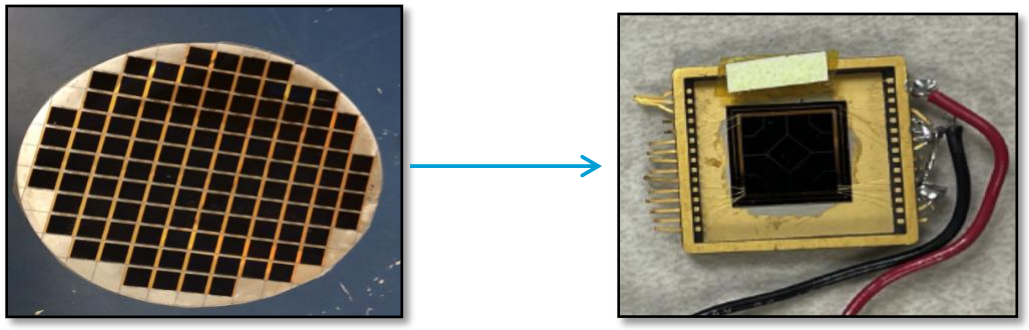

Figure 6.2: Image of a 6-inch fabricated InGaP wafer (left), Wire-bonded and packaged InGaP device ready for characterization (right).

6.2 Characterization

The InGaP devices were characterized by performing I-V measurements in the dark (without the presence of photons/electrons), in the presence of photons from UV light source and then under a monoenergetic electron beam to simulate their performance under real beta sources.

6.2.1 IV Measurements in the Dark and under UV Light Source

Figure 6.3 shows the IV curves (both in linear and log scale) for an InGaP device in the dark and under a UV light source. In the dark mode, the V_{oc} is close to 0 V as expected, and the leakage current density at -4 V is -2.98E-02 Amps/cm^2. With the presence of photon stimulus from UV flashlight, the IV curve drops down into the fourth quadrant (linear scale) indicating that the device is generating power. When the current is plotted in a log scale as shown in figure 6.3b, we can see a clear shift (~ 0 V to 1.24 V) in the V_{oc}. The shift in V_{oc} is due to photon stimulating the device and turning it on. Tables 6.1 – 6.2 show the extracted parameters from the dark IV and UV light source IV curves.

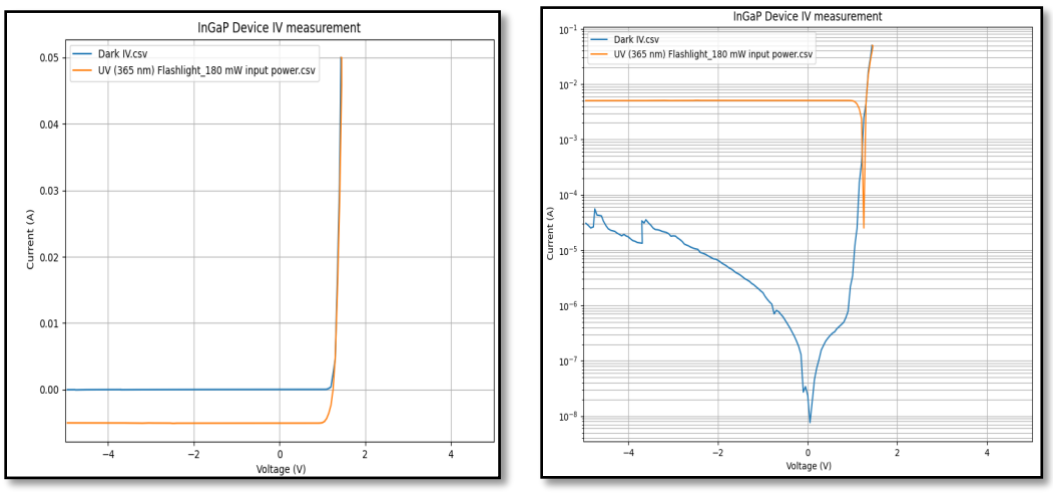

Figure 6.3: a) I-V measurement in the Dark mode and under UV flashlight. b) log I-V curve.

Table 6.10: Parameters extracted from the IV curves of InGaP device in Dark mode.

InGaP Device	Size (cm^2)	Shunt Resistance (ohm-cm^2)	Series Resistance (ohm-cm^2)	Leakage Current at -4 V (Amps/cm^2)	Turn on Voltage (V)
Dark IV	1	2.08E+06	0.97	-2.98E-02	1.1

The turn on voltage for the InGaP device is ~ 1.1 V. In an ideal diode, the turn on voltage should match its bandgap energy of ~ 1.86 eV but due to parasitic and series

resistances present in fabricated diodes, turn on voltage is always less than the bandgap energy of the semiconductor. These InGaP devices have low series resistance (0.97 ohms-cm^2), high shunt resistance (2.08E+06) and low leakage current density, which indicates that these are good diodes.

Table 6.11: Parameters extracted from the IV curves of InGaP device under UV Light Source (flashlight)

InGaP Device	Size (cm^2)	Voc (V)	Isc (A)	MPP (W)	Fill Factor	Efficiency (%)
UV (365 nm, 180 mW/cm^2)	1	1.244	5.06E-3	5.05E-3	0.7985	2.8

Table 6.2 shows the extracted parameters from the IV curve under photon stimulus. The input power of the flashlight was fixed at 180 mW/cm^2 with a wavelength of 365 nm. The MPP (maximum power point) of 5.05 mW was calculated with an efficiency of 2.8 % using equations 6.1 and 6.2, respectively.

$$P_{max} = V_m * I_m \qquad (6.1)$$

$$\eta = \frac{P_{out}}{P_{in}} \qquad (6.2)$$

The fill factor (FF) of this device was calculated using equation 6.3:

$$FF = \frac{V_m I_m}{V_{oc} I_{sc}} \qquad (6.3)$$

FF is a parameter which, in conjunction with V_{oc} and I_{sc}, determines the maximum power from a solar device. V_m and I_m are the voltage and current at the maximum operating point of the device, respectively. V_{oc} is the open circuit voltage and I_{sc} is the short circuit current of a device. The fill factor of 0.7985 shows that our device is a reasonable photovoltaic device.

6.2.2 IV Measurements under the monoenergetic Electron Beam

We used a monoenergetic electron beam to mimic InGaP device performance under ^{3}H and ^{63}Ni beta sources. The monoenergetic electron beam's input current was fixed at 300 pA (165 mCi) and the voltage of it was varied from 3 kV up to 16 kV with a step size of 3 kV. These measurements were taken similarly as to the photo-response measurements, but an electron beam was used instead of a light source for device stimulation. An external semiconductor analyzer generated the IV curves as the electron beam was incident on the device. Figure 5.4a shows the IV curves generated, as the electron beam was incident on the device. The V_{oc} continuously increased as the electron-beam energy was increased. The maximum output power of the device was calculated at each step size by using equation 6.1. We observed that the output power of a device increased as the input energy of the electron beam increased. This is because more EHPs are created in the device as the input power of the electron beam increases, thus increasing the output power of the device.

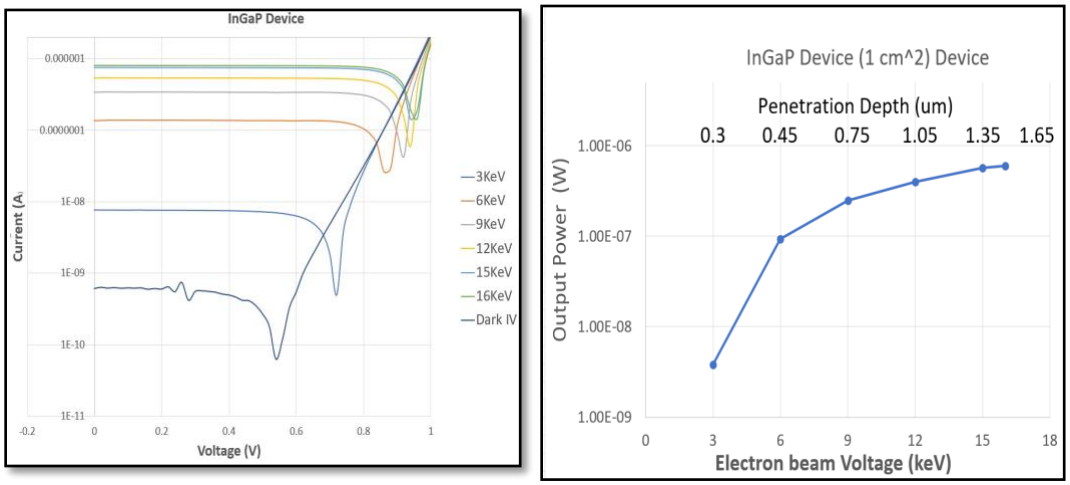

Figure 6.4: a) log I-V curves as a function of beam voltage. B) the output power as a function of incident beam energy. MCNP results showing penetration depths of monoenergetic electron beam into InGaP are also listed here.

Table 6.3: Parameters extracted from the IV curves of InGaP device under monoenergetic electron beam stimulus.

InGaP Device (1 cm^2)

E-Beam Energy (keV)	Voc (V)	Isc (A)	MPP (W)	FF	Pin (µW)	Eff (%)
3	0.72	7.71E-07	3.84E-09	0.69	0.9	0.43
6	0.86	1.35E-07	9.31E-08	0.81	1.8	5.25
9	92	3.39E-07	2.48E-07	0.80	2.7	9.20
12	0.85	5.42E-07	4.02E-07	0.79	3.6	11.15
15	0.94	7.51E-07	5.66E-07	0.80	4.5	12.58
16	0.96	7.99E-07	6.02E-07	0.79	4.8	12.63

Figure 6.4b shows the output power as a function of incident beam energy at each step size. From this plot, the MPP at 6 keV (93 nW with an efficiency of 5.25 %) and 16 keV (606 nW with an efficiency of 12.63 %) represents the average energy emission for beta sources ^{3}H and Ni^{63}, respectively. Our electron beam system has maximum electron energy of 16 keV and the output power and efficiency simulating Ni^{63} was calculated at the incident beam energy of 16 keV instead of 17 keV.

6.3 Discussion of the EBIC Results on InGaP

We observed that even though the intrinsic layer is only 10 nm thick in the InGaP wafer, the efficiency of the InGaP device kept increasing with the electron beam energy as shown in figure 6.5.

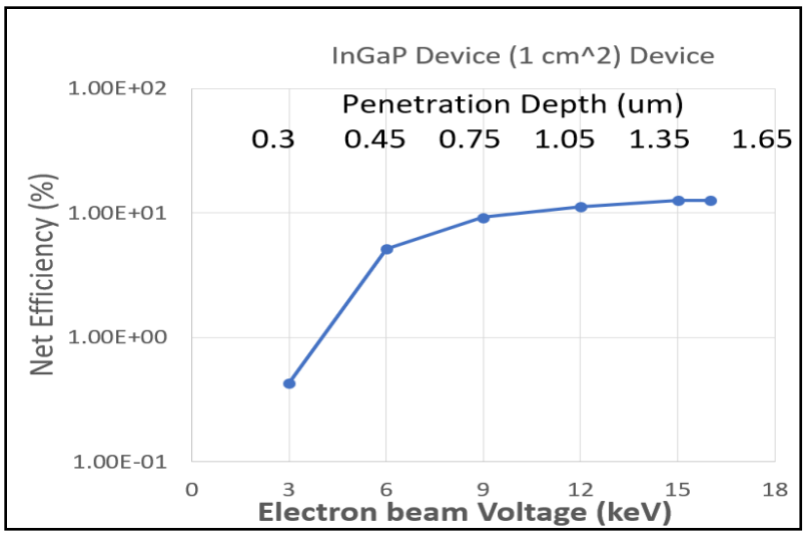

Figure 6.5: Efficiency of the InGaP device as a function of electron beam voltage.

As seen in figure 6.5, a 15 keV monoenergetic electron beam penetrates ~ 1.35 µm into InGaP, which is well beyond the depletion region width of 110 nm. Yet the efficiency of the device increased as the electron beam penetrated further into the device. This happens because of two main reasons:

1. $In_{0.49}Ga_{0.51}P$ films grown on top of GaAs are epitaxially matched (their lattices are matched), therefore the threading dislocations are only on the order of $10^3/cm^2$ with a minority carrier diffusion length of > 1.5 µm [7]. Also, in this InGaP structure, we have a thin n-layer on top and a wide (1.5 µm) p-layer on the bottom. Most of the EHPs that are generated due to beta particles are generated in this p-layer and thus electrons are the minority carriers. Since electrons have higher mobility and greater diffusion lengths compared to holes, they are able to diffuse into the depletion region even from a distance of 1.5 µm.
2. Another junction forms between the p-base layer and heavily doped p+ layer of 50 nm. This junction has its own electric field called back surface

field (BSF), which prevents minority carrier (electrons) from falling into the heavily doped p+ layer. The probability of minority carriers recombining in heavily doped p+ layer is very high and BSF prevents them from falling into heavily doped p+ layer. Instead, it helps in the diffusion of minority carrier (electrons) by pushing them towards the depletion region.

Chapter 7: Characterization of InGaP and GaN Devices for an Alphavoltaic Power Source and ZnS-InGaP for an Alpha-photovoltaic Power Source

In this study, we investigated the energy conversion rate of degradation in InGaP and GaN p-i-n devices for an alphavoltaic power source by exposing them under a 4.5 MeV alpha beam (linear accelerator of He2+ ions), simulating Am-241 alpha isotope. The purpose of this experiment was to understand the radiation damage in GAN and InGaP devices by examining their MPPs (maximum power point) and efficiencies over the interval of the alpha beam exposure at different beam currents (higher beam current represent accelerated exposure). The energy rate of degradation of ZnS phosphor which is utilized in alpha-photovoltaic power source for indirectly converting alpha particles energy into electrical energy via photons is also examined.

7.1 Introduction

Alphavoltaic power sources are direct energy conversion devices that convert the emission (alpha particles) of alpha-isotopes directly into electrical energy. Alpha isotopes such as Am-241 have 1000 times higher energy than beta isotopes such as Tritium (average energy emission of 5.6 KeV). Therefore, they can be used to generate output power in mW/cm^2 range, whereas state of the art betavotlaic devices can only generate output power in $\mu W/cm^2$ range. However, alphavoltaic power sources have not been technologically successful so far due to heavy nuclei alpha particles causing radiation damage in the semiconductor materials by displacing atoms in their crystal structure [89-92]. The key to future development of this technology resides in the ability to limit this radiation damage. Several approaches to solving this problem have

been investigated. One approach is to use pn/p-i-n devices fabricated from radiation tolerant ultra-wide-bandgap semiconductor materials, which are not available yet. The second approach (alpha-photovoltaics) is to use an intermediate photoluminescent layer to absorb the alpha particles energy and convert it into photons, preventing radiation damage in the semiconductor [93-94]. Then these photons are directed towards the semiconductor junction to generate electrical output power, just like photovoltaic devices. The experimental details and results from both approaches are presented here. In the first approach, we exposed InGaP and GaN devices directly under a 4.5 MeV alpha beam (simulating Am-241) and examined how the MPP and the efficiency in these devices degrades over an interval of the exposure at different beam currents. In the second approach, we deposited a ZnS layer (intermediate layer) on top of the InGaP device and analyzed the MPP and efficiency of the ZnS-InGaP device over the interval of the alpha beam exposure in a similar manner.

7.2 Experiment

A linear accelerator of He2+ ions located at the Aberdeen Proving Ground (APG) campus of the US. Army Research Laboratory was used to simulate the alpha particles from Am-241. For this setup, the voltage of the alpha beam was fixed at 4.5 MeV, only the beam current can be changed to represent different isotope activity (mCI). Equation 7.1 below is used to calculate the isotope activity from the beam current.

$$1\ mCi = 5.92 * 10^{-12}\ \text{Amps}$$

Figure 7.1: Alpha beam linear accelerator with a device package mounted in the vacuum chamber.

7.2.1 GaN Device

We exposed AGG device (size = 0.16 cm^2) under three different beam currents of the alpha beam and analyzed its MPPs and energy conversion efficiency over the interval of the exposure. We selected AGG structure for this experiment because GaN/GaN structure has a lower number of dislocation defects compared to lattice mismatched GaN/Sapphire structure. Our automated semiconductor analyzer took IV curves every 30 seconds during the whole interval of the exposure and the MPP was calculated from each of these IV curves. Figure 7.2 shows IV curves from a 1.40 nA beam current exposure, and figure 7.3 shows the MPP of the device at four different beam currents during the 10-minute exposure.

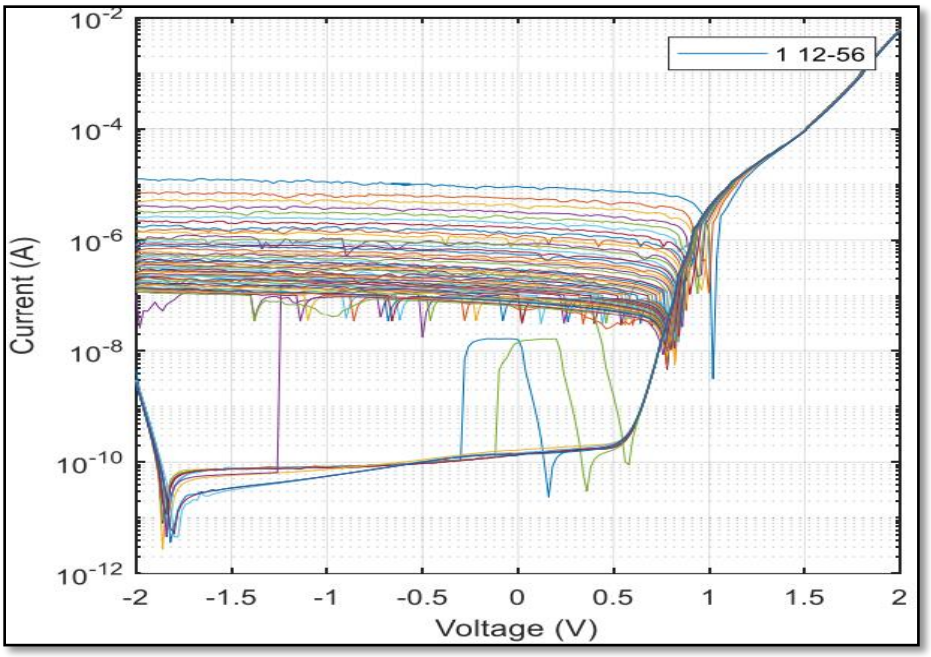

Figure 7.2: Example showing I-V curves generated under the alpha beam exposure on the AGG device using our automated semiconductor analyzer

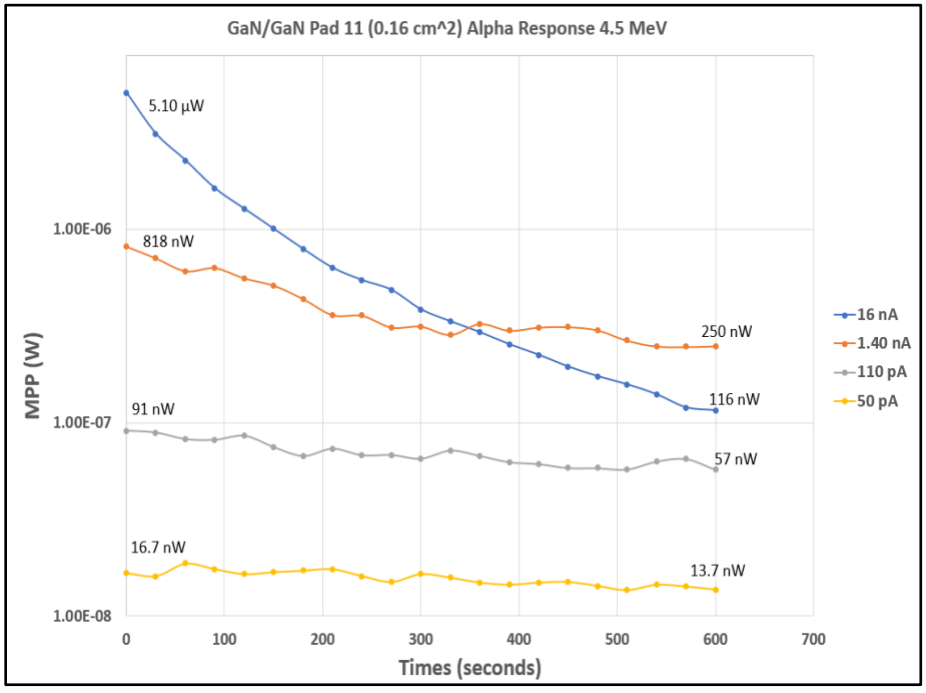

Figure 7.3: MPPs of the AGG device under four different beam currents for the first 600 s of the exposure

Table 7.12: Beam Conditions for the alpha beam exposure to GaN Device

Beam Conditions for GaN/GaN (0.16 cm^2) Exposure							
Time (s)	Beam Current (A)	Beam Voltage (MeV)	Beam size (cm^2)	Flux (He2+/s)	Activity (mCI)	Total Fluence (# of atoms or ions)	Activity Density (mCI/cm^2)
600	5.00E-11	4.5 MeV	3.00E-02	3.13E+08	8.45E+00	1.88E+11	2.82E+02
600	1.10E-10	4.5 MeV	3.00E-02	6.88E+08	1.86E+01	4.13E+11	6.19E+02
600	1.40E-09	4.5 MeV	3.00E-02	8.75E+09	2.36E+02	5.25E+12	7.88E+03
600	1.60E-08	4.5 MeV	3.00E-02	1.00E+11	2.70E+03	6.00E+13	9.01E+04

Figure 7.3 shows the degradation in the MPP of the device over the first 600 s of the exposure under four different beam currents. We observed that the degradation rate is much higher for 16 nA beam current (2700 mCi) as the MPP dropped from 5.10 µW to 116 nW in only 600 s. The rate of degradation is lower at the 50 pA and 110 pA currents, and these are the realistic isotope activity (8.45 mCI and 18.6 mCI, respectively) that would be used in an alphavoltaic power source. The damage in GaN device is not permanent. We performed dark IV curves on the device after alpha beam exposure and they showed similar behavior pre and post exposure at even after the 16 nA beam current. These results suggest that GaN is not a good candidate for a direct alphavoltaic power source but it has great self-healing properties. Figure 7.4 shows the visible discoloration spot where alpha beam was focused.

Figure 7.4: 1.4 nA beam exposure mark showing visible discoloration in the GaN device.

7.2.2 INGaP Device

Similarly, we exposed the InGaP device (size = 1 cm^2) under the alpha beam at two different beam currents and generated IV curves. From these IV curves, we calculated the MPP of the device every 30 seconds for both beam current values, as shown in Figure 7.5.

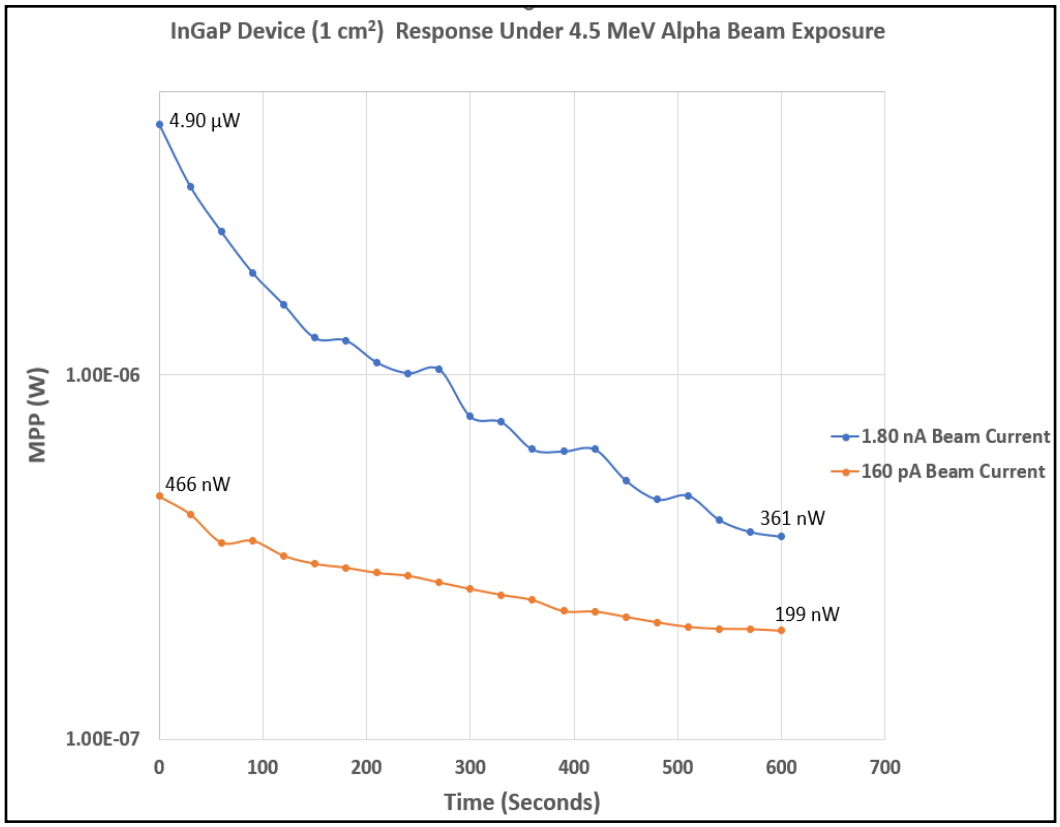

Figure 7.5: MPP of the device at different beam currents. MPP degradation as a function of time (Fluence).

Figure 7.5 shows the degradation in the MPP of the InGaP device over the first 600 s of exposure under two different beam currents. We observed that the degradation in MPP occurs at both beam currents, suggesting that InGaP is also not a good candidate for an alphavoltaic power source.

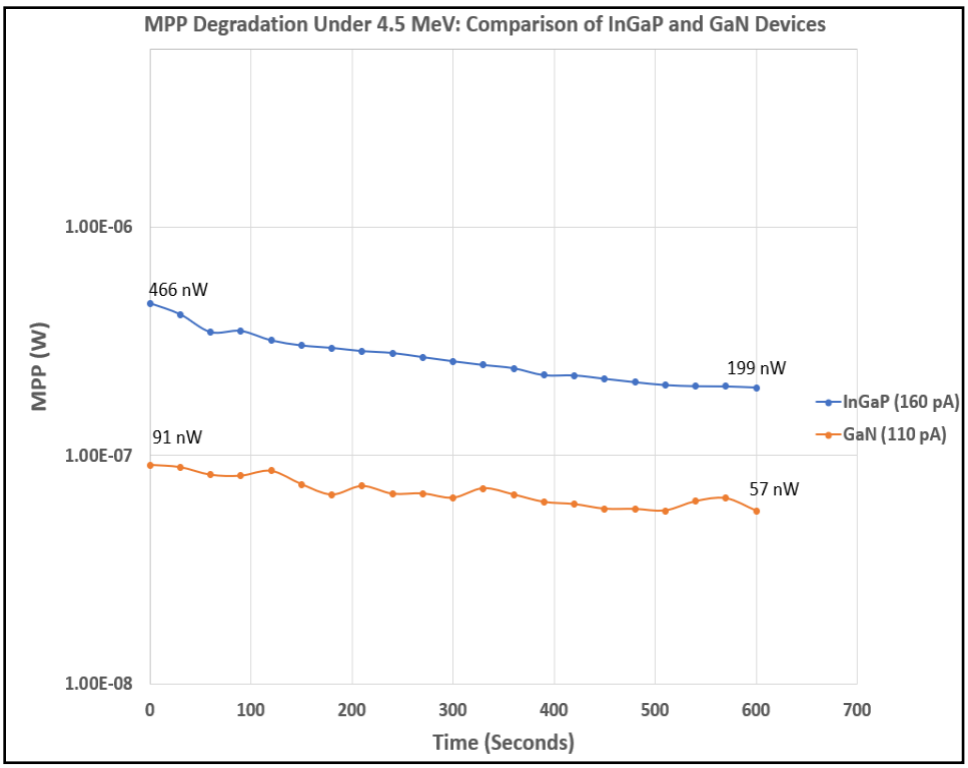

Figure 7.6: MPP Degradation comparison of InGaP and GaN devices under alpha beam.

Figure 7.6 compares the MPP degradation of GaN and InGaP devices for ~ 100 pA beam current. The MPP drops by 58 % in InGaP device compared to a drop of 38 % in GaN device. However, the MPP of an InGaP device (466 nW) is ~ 5 times higher than the MPP of a GaN device (91 nW) at the initial exposure, and still ~ 2 times higher than the initial MPP of GaN device after 600 s of the alpha beam exposure. We believe the MPP in InGaP device is higher because of its larger (1600 nm) charge collection area compared to a charge collection area (650 nm) in AGG GaN device. But the MPP degrades faster in InGaP device compared to a GaN device. This is because GaN (Eg = 3.40 eV) has a wider electronic bandgap than InGaP (Eg = 1.86 eV). The increase in the electronic bandgap energy makes the semiconductor material more radiation resistant, that is the reason ultra-wide bandgap semiconductors such as Diamond (E_g = 5.47 eV) are thought be the ideal candidates for an alphavoltaic power source. Until

ultra-wide bandgap semiconductors are made available, alternative approaches such as alpha photovoltaics (APV) needs to be looked at which is demonstrated in the next section.

7.3 Alpha-photovoltaic Apprach on InGaP Device

Figure 7.7 shows the schematic of an alpha-photovoltaic (APV) device investigated in this study.

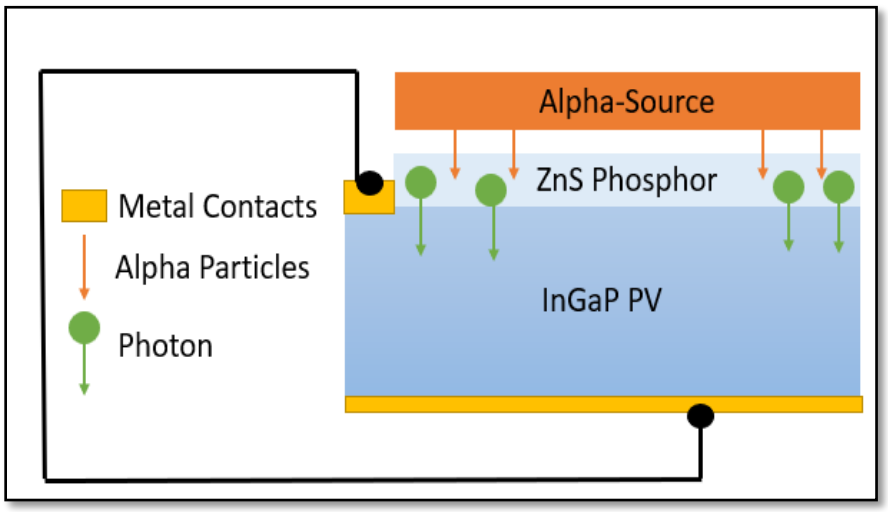

Figure 7.7: Schematic of an APV device in operation. Its working principle is like solar cells –photons come from sunlight in solar cells whereas in alpha-photovoltaic devices, photons are emitted by the ZnS when alpha particles deposit their energy within the phosphor. A ZnS film also prevents radiation damage in semiconductor junction.

We used an InGaP device for this approach because its absorption properties are well matched to photon emission of the ZnS phosphor [95-96]. The bandgap of InGaP is 1.86 eV therefore no photon with lower energy (or wavelength larger than 614 nm) will generate an electron hole pair (EHP) within the material. The energy of the 530 nm photons generated in ZnS phosphor is 2.35 eV. The near match emission of wavelength to InGaP bandgap reduces thermalization losses during energy conversion while maintaining a high degree of energy efficiency (~ 80%) [97].

7.3.1 Methods

We utilized SRIM (stopping range of ions in matter) software to numerically model the energy deposition of 4.5 MeV alpha particles into ZnS to determine the thickness of the ZnS phosphor needed to prevent radiation damage in the InGaP device from alpha particles directly. Figure 7.8 shows our SRIM modeling results.

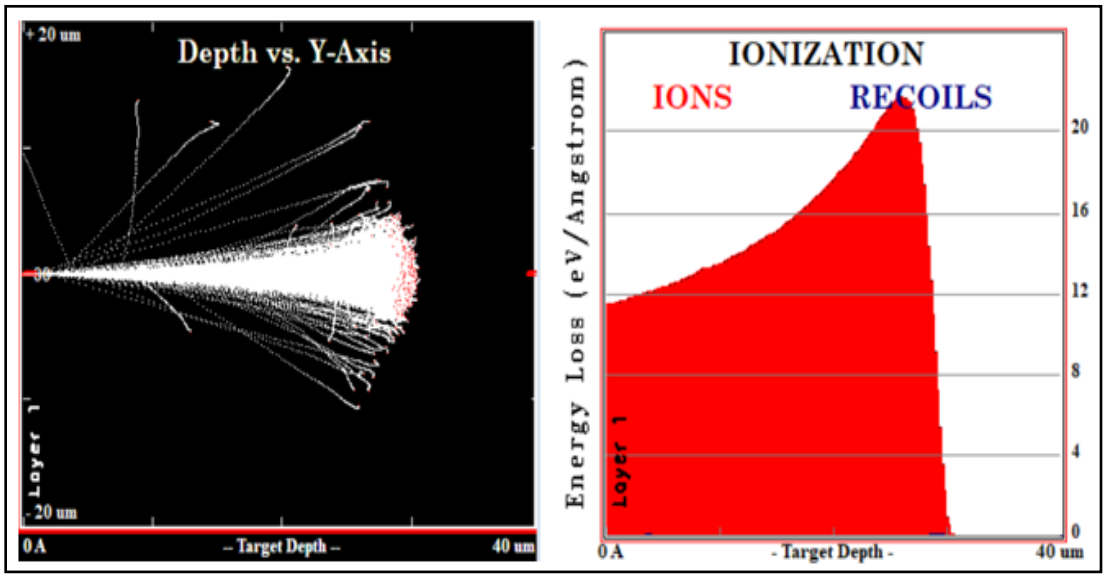

Figure 7.8: Trajectory map of 4.5 MeV alpha particles irradiating a ZnS layer shows a longitudinal penetration of 29 µm and a lateral range of 1.1 µm (left). 97% of the alpha particle energy goes into ionization (right).

The 4.5 MeV beam penetrates ~ 29 µm into the ZnS. Any thickness of ZnS over 29 µm will prevent InGaP device from alpha particles radiation damage. As alpha particles penetrate into ZnS, they create electron hole pairs (EHPs) using ionization and since there is no electric field in ZnS to separate the EHPs, they recombine and generate photons which are emitted in an isotropic manner with a wavelength of 530 nm [98]. It is evident from figure 7.8 that when alpha particles lose energy at the end of their trajectory, the loss mechanism changes from ionization to ballistic scattering with nuclei and vacancy creation within the crystalline structure. Therefore, alpha particles

cause most of the damage towards the end of their penetration range. It is then important to make the ZnS film thicker than the penetration range of alpha particles to make sure alpha particles end up in the ZnS film and not in the InGaP device to prevent radiation damage. At the same time, the ZnS film cannot be made too thick because of the self-absorption of the photons in the ZnS. In our previous work, we measured the self-attenuation constant (1/e) of 530 nm photons in ZnS phosphor which is ~ 150 µm[98].

We deposited a 53 µm thick ZnS film onto InGaP device using an electrophoretic deposition (EPD) process. EPD is a time-controlled method in which voltage is applied in a solution (isopropyl alcohol (IPA), a nitrate salt of Mg $(NO_3)_2 \cdot 6H_2O$, and a ZnS) to create an electric field which moves the charged particles (ZnS in this case) from the solution to form a thin coating onto the device [99-100]. Figure 7.9 shows our InGaP device with ZnS film coating.

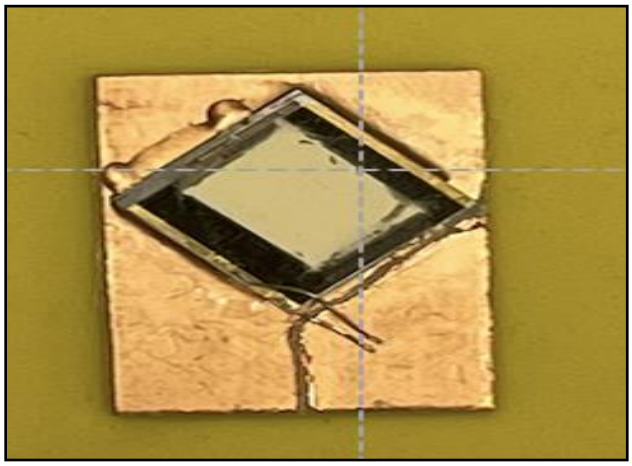

Figure 7.9: InGaP device with ZnS deposited using EPD process. The ZnS phosphor film thickness is 53 µm.

7.3.2 Results and Discussion

The InGaP with ZnS film coating was exposed to 4.5 MeV beam energy with a beam size of 3 mm^2. The current varied in three increments: 100 pA, 1 nA and 10 nA

each with 10-minute exposure times. These IV curves were acquired continuously every 30 seconds during the alpha beam irradiation, as shown in figure 7.9. The maximum power from each IV curve is calculated and plotted as a function of time (fluence) in figure 7.10.

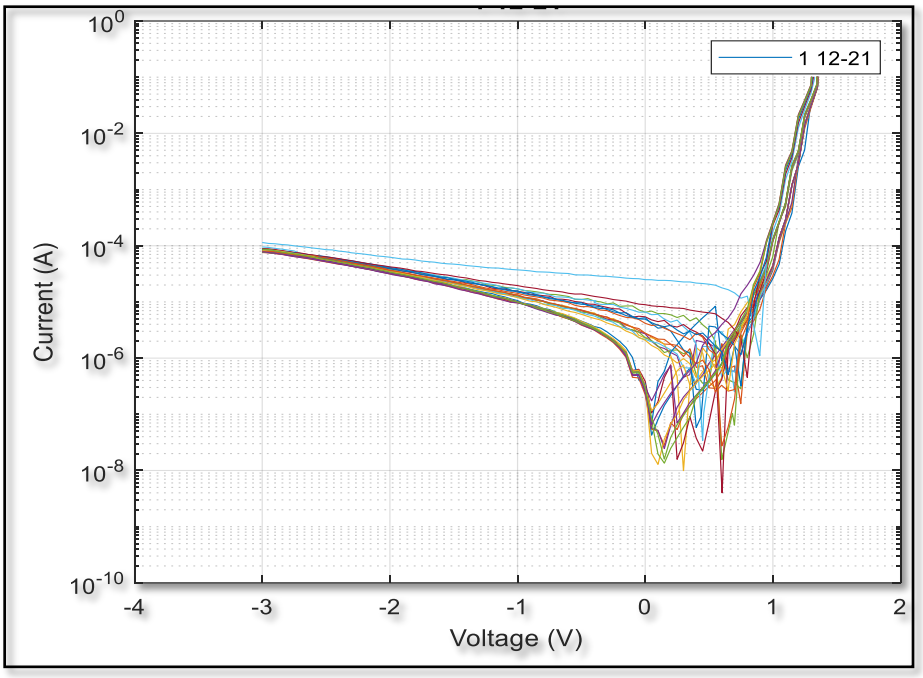

Figure 7.10: The IV curves acquired every 30 seconds during the alpha exposure show the degradation of ZnS photon generation beyond 10^{10} ion fluence.

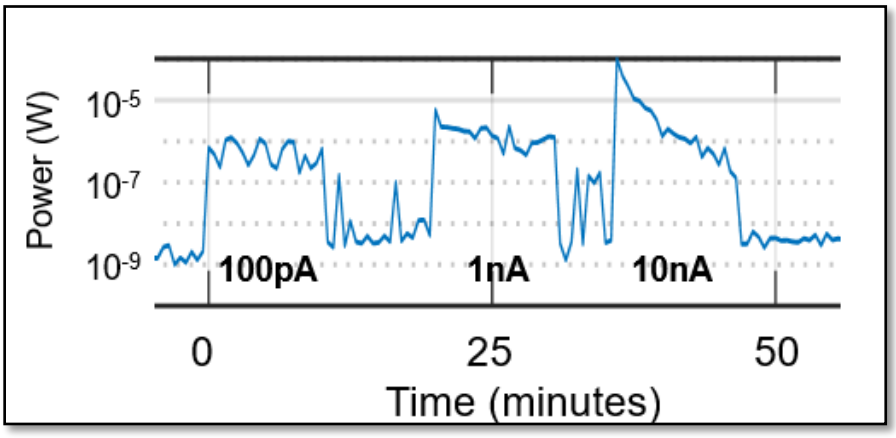

Figure 7.11: Electrical Power measured in the InGaP device varies as alpha beam current is stepped from 100 pA to 1nA to 10nA. The current is delivered over a constant 3mm^2 beam area.

Initial results shown in figure 7.10 indicated that no degradation of the InGaP device's maximum power point (MPP = ~1 µW) during the 100-pA exposure which delivered a fluence of $3.75x10^{11}$ ions. The MPP falls by a factor of 3 during the 1 nA ($x10^{12}$ ions) 10-minute exposure, and the MPP falls by a factor of 100 during the 10 nA (fluence of $3.75x10^{13}$ ions) 10-minute exposure.

The initial IV curves measured for each increment of current (100 pA, 1 nA and 10 nA) are shown in figure 7.12. The V_{oc} increases from 0.7 V to 1 V with the increase of alpha beam current, as a result MPP is also increased.

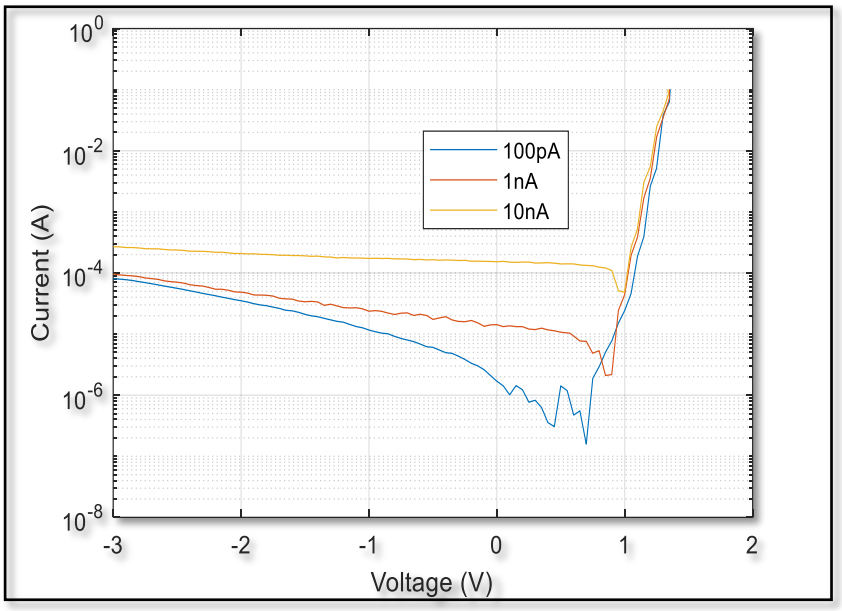

Figure 7.12: IV curve at the beginning of the series for each of the current densities evaluated during alpha beam exposure. The open circuit voltage (V_{oc}) and short circuit current (I_{sc}) increase with alpha beam current.

7.4 Accelerated Testing of InGaP, GaN and ZnS phosphor under Direct Alpha Exposure to determine the Energy Conversion rate of Degradation

Figure 7.13 shows the efficiencies of three different materials under different beam currents as a function of total fluence. Total fluence is calculated by multiplying

the flux (ions/s) over the duration of the exposure. Higher beam currents are used for accelerated testing to determine how long a power source made with each of these materials would last (90 % degradation in efficiency is defined as end of life for power source).

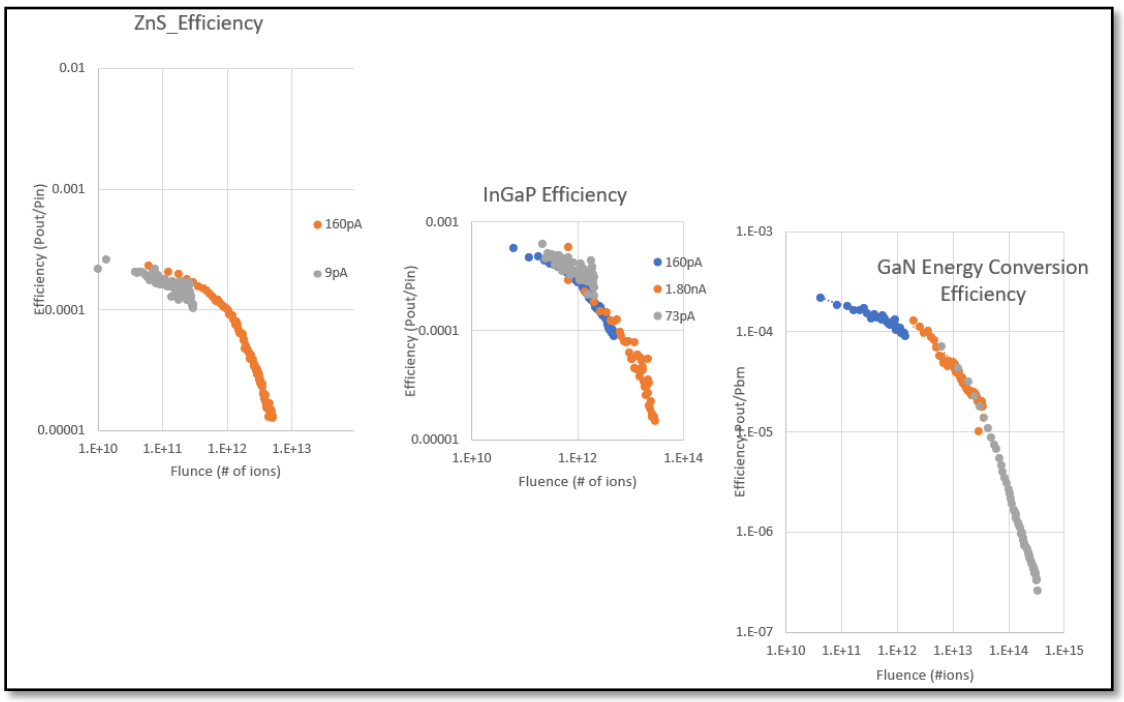

Figure 7.13: The efficiency of ZnS, InGaP and GaN devices under direct exposure to 4.5 MeV alpha beam as a function of total flux.

From figure 7.13, it is evident that the energy conversion rate of degradation follows the same pattern as a function of fluence, even at different beam currents in all three materials (ZnS, InGaP and GaN). From this we can conclude that the radiation damage in these materials is only due to heavy nuclei alpha particles causing radiation damage by displacing atoms in the crystal structure, and not due to any thermal loading (heat generated) effects.

Table 7.13: Lifetime of Power Source calculations based on different materials degradation rate at 100 pA beam current representing ~ 18 mCi of activity

	beam current	flux (ions/s)	Total fluence where 90% degradation happens	Time (s)	Lifetime of Power Source (hours)	Bandgap (eV)
InGaP	1.00E-10	6.25E+08	1.00E+13	1.60E+04	4.4444	1.86
ZnS	1.00E-10	6.25E+08	5.00E+12	8.00E+03	2.2222	3.54
GaN	1.00E-10	6.25E+08	1.80E+13	2.88E+04	8	3.4

Table 7.2 shows that an alphavoltaic power source made with InGaP and GaN semiconductors would only last 4.44 hours and 8 hours, respectively. However, an alpha-photovoltaic power source employing ZnS phosphor as an intermediate layer to prevent radiation damage would only last only 2.22 hours. This is because the degradation rate of ZnS phosphor itself is faster compared to degradation of InGaP under direct alpha exposure. However, the ZnS phosphor degradation rate can be significantly reduced by forming a mixture of alpha source (Am-241) and ZnS phosphor before applying to the InGaP device. This technique would uniformly spread out the radiation damage instead of direct exposure to the same spot on the surface.

Chapter 8: Conclusions and Future Work

8.1 Conclusions

In this study, GaN and InGaP p-i-n devices were developed and evaluated for betavoltaic power sources. GaN devices were fabricated on three different wafers with variations in i-layer thicknesses (600 nm, 700 nm and 1 µm), all grown by MOCVD. Two GaN p-i-n structures were grown on top of a sapphire substrate and the third structure was grown on top of a bulk GaN substrate. InGaP devices were fabricated on an InGaP n-i-p structure grown on top of a gallium arsenide (GaAs) substrate by CCS-MOVPE.

MCNP modeling was utilized to determine the energy deposition profile (# of EHPs generated) of monoenergetic electron beam into GaN and InGaP semiconductors. A monoenergetic electron beam at 6 KeV and 16 KeV represents the average energy emission of ^{3}H and Ni-63 beta isotopes, respectively. TCAD simulations were performed to figure out the effective charge collection area in these structures to determine how much of the deposited energy is collected and contributes to the output power. In a GaN p-i-n structure, the effective charge collection area is mostly made up of the thickness of the i-layer, and thus the structure with a 1 µm i-layer thickness had the largest charge collection area (1.08 µm). The doping concentration of the i-layer determines how thick it can be made and we present here the thickness and doping concentration needed to have a fully depleted i-layer. The InGaP structure has an effective charge collection area of ~ 1.6 µm even though its depletion region thickness is only 10 nm because of large diffusion lengths of minority carriers in InGaP.

Devices were characterized using current - voltage (IV) measurements without illumination (light or beta), using a UV light source, and under an electron beam. Dark IV measurements confirmed good quality diodes with a low series resistance, high shunt resistance, and low leakage currents in both GaN and InGaP structures. A clear photo-response was observed when IV curves were measured under a light source at a wavelength of 365nm (3.40 eV). We tested both sets of devices under an electron beam and evaluated their performance at the average energy of ^{3}H and Ni-63. Of all the three GaN structures, the SGS device with an i-layer thickness of 1 µm had the highest MPP (3.32 $\mu W/cm^2$) and efficiency (13.2%) at 16 KeV due to its wider charge collection area, as predicted by TCAD modeling. InGaP devices also had the highest MPP (3.01 $\mu W/cm^2$) and efficiency (12.63%) at 16 KeV. When comparing the performance of InGaP and GaN devices, we learned that InGaP devices outperformed GaN at 6 KeV (average energy emission of ^{3}H) and had a comparable performance at 16 KeV (average energy emission of Ni-63). Since InGaP devices are 10 X cheaper and are readily available, we concluded that InGaP devices are better suited for a betavoltaic power source at present. But GaN has a huge room for improvement and thus has a greater potential if further optimization can be made in the intrinsic layer dopings and ohmic contact formation as well as improving material quality through growth technology.

Since all three of our GaN devices had different i-layer thicknesses, we couldn't make a fair comparison between GaN/Sapphire and GaN/GaN devices. Based on our results from the IV measurements in the dark, UV and under electron beam stimulus, we learned that GaN/Sapphire devices had a slightly better performance even when factoring in the limitations of GaN/GaN devices (smaller collection area, etc).

We also learned that the GaN p-i-n structure design (i-layer doping and thickness) is more critical than the different substrate growth. Based on the findings from this study, we proposed a multi-junction GaN structure for optimal betavoltaic performance.

To determine the suitability of InGaP and GaN devices for an alphavoltaic power source, we exposed these devices under the 4.5 MeV alpha beam and examined their MPPs over the duration of the exposure. Both InGaP and GaN devices showed degradation as their MPPs declined (58 % for InGaP and 42 % for GaN) over the first 10 minutes of the exposure which showed that they are not good candidates for a direct alphavotaic power source. We also investigated an alpha-photovoltaic approach to limit radiation damage in the semiconductor device by employing ZnS phosphor as an intermediate layer placed between the alpha beam and an InGaP device. However, we learned that the degradation rate of ZnS phosphor is even faster compared to the direct alpha exposure to GaN and InGaP devices. This is the preliminary work in alpha-photovoltaics, and we expect different techniques of applying ZnS phosphor or other radiation tolerant phosphors could be investigated to slow down the degradation rate. For example, by forming a solution of ZnS phosphor and alpha source (Am-241) before applying it to the InGaP device can spread out the radiation damage uniformly and slow down the degradation rate.

8.2. Future Work

1. Need to increase the power output of the betavoltaic devices by improving GaN material properties and/or use other wideband gap semiconductors with better material properties i.e better interfaces, less defects, better ohmic contact technology, and better lattice matched substrates.

2. Need to develop effective modelling tools for betavoltaic and alphavoltaic power sources.
3. Alphavoltaics can in theory generate output powers in the mW range, but radiation damage needs to be fully understood in these materials in order to develop effective direct or indirect alphavoltaic power sources.
4. Development of multijunction devices may significantly improve output powers in both betavoltaic and alphavoltaic devices.

Bibliography

[1]. S. Carrara, "Body Dust: Well Beyond Wearable and Implantable Sensors," in *IEEE Sensors Journal*, vol. 21, no. 11, pp. 12398-12406, 1 June1, 2021, doi: 10.1109/JSEN.2020.3029432.

[2]. Prelas, M., et al., Nuclear Batteries and Radioisotopes. 2016: Springer International Publishing.

[3]. Bower, K.E., et al., Polymers, phosphors, and Voltaics for Radioisotope Microbatteries. 2002: CRC Press.

[4]. Kumar, S., 2015. “Atomic Batteries: Energy from Radioactivity”. Journal of Nuclear Energy Science and Power Generation Technology, 05(01), pp. 1–8.

[5]. Manasse, F., J. Pinajian, and A. Tse, Schottky barrier betavoltaic battery. IEEE Trans. Nucl. Sci, 1976. **23**(1).

[6]. Khan, et.al, “Alpha-photovoltaics for milliwatt applications”. IDETC conference proceedings 2022.

[7]. Tariq R. Alam and Mark A. Pierson, Principles of Betavoltaic Battery Design, Journal of Energy and Power Sources, Vol 2, No. 1, June 30, 2016

[8]. Rajesh Duggirala, Amit Lal, Shankar Radhakrishnan “Radioisotpe Powered Thin Film Microsystem, Springer 2010, page 1-3

[9]. Krane, K.S. "Beta Decay." Introductory Nuclear Physics. New York,NY: Wiley, 1988. 273+. Print.

[10]. Shultis, J. Kenneth., and Richard E. Faw. "Radioactivity." Fundamentals of Nuclear Science and Engineering. Boca Raton: CRC, 2008. 96-100. Print.

[11]. Lutz, Josef. "Pin-Diodes." Semiconductor Power Devices: Physics, Characteristics, Reliability. Berlin: Springer, 2011. 159-66. Print.

[12]. Nuclear Physics PHY303 (PHY303 Nuclear Physics 8) < http://physics-database.group.shef.ac.uk/phy303/phy303-8.html >

[13]. www.nasa.gov, Natl. Aeronaut. Sp. Adm. 2950 (2013).

[14]. Yakubova, G.N., Nuclear Batteries with Tritium and Promethium-147 Radioactive Sources. 2010, University of Illinois.

[15]. Li, H., et al., Self-reciprocating radioisotope-powered cantilever. Journal of Applied Physics, 2002. 92(2): p. 1122-1127.

[16]. Duggirala, R., et al., Radioisotope thin-film fueled microfabricated reciprocating electromechanical power generator. Microelectromechanical Systems, Journal of, 2008. **17**(4): p. 837-849.

[17]. Chandrashekhar, M., et al., Demonstration of a 4H SiC betavoltaic cell. Applied Physics Letters, 2006. **88**: p. 033506.

[18]. Rybicki, G., C. Vargas-Aburto, and R. Uribe. Silicon Carbide Alphavoltaic Battery. 1996.

[19]. Bailey, S.G., et al. Photovoltaic development for alpha voltaic batteries. 2005: IEEE.

[20]. Sychov, M., Kavetsky, A., Yakubova, G., Walter, G., Yousaf, S., Lin, Q., Chan, D., Socarras, H. and Bower, K., 2008. Alpha indirect conversion radioisotope power source. Applied Radiation and Isotopes, 66(2), pp.173-177.

[21]. Sha Xue, Chuting Tan, Praneeth Kandlakunta, Ibrahim Oksuz, Vasil Hlinka, Lei R. Cao, Methods for improving the power conversion efficiency of nuclear-voltaic batteries, Nuclear Instruments and Methods in Physics Research Section A: Accelerators, Spectrometers, Detectors and Associated Equipment, Volume 927, 2019, Pages 133-139

[22]. W. Ehrenber, et al., “The Electron Voltaic Effect” Proc. Rody. Soc. 64, 424 (1951).

[23]. Rappaport, P., The electron-voltaic effect in p-n junctions induced by beta-particle bombardment. Physical Review, 1954. **93**(1): p. 246-247.

[24]. Pfann, W. and W. Van Roosbroeck, Radioactive and Photoelectric pn Junction Power Sources. Journal of Applied Physics, 1954. **25**: p. 1422.

[25]. Vul, B., et al., On the transformation of ß-particle energies to electric energy in germanium crystals with pn junctions. Atomic Energy, 1957. **2**(6): p. 653-657.

[26]. Olsen, L., S. Seeman, and B. Griffin, Betavoltaic nuclear electric power sources. Trans. Amer. Nucl. Soc., 12: 481-2 (Nov. 1969, 1969.

[27]. Ko, W. and J. Hynecek, Implant Evaluation of a Nuclear Power Source-Betacel® Battery. IEEE transactions on Biomedical Engineering, 1974: p. 238-241.

[28]. Huffman, F. and J. Norman, Nuclear-fueled cardiac pacemakers. Chest, 1974. **65**(6): p. 667.

[29]. Wei, L., Parametric studies and optimization of the beta-voltaic cell Solid-State Electronics, 1974. **17**(10): p. 1091-1098.

[30]. Wei, L., Parametric studies and optimization of the beta-voltaic cell-II open-circuit voltage and power efficiencies. Solid-State Electronics, 1975. **18**(1): p. 71-77.

[31]. Guo, H. and A. Lal. Nanopower betavoltaic microbatteries. 2003.

[32]. Eiting, C., et al., Demonstration of a radiation resistant, high efficiency SiC betavoltaic. Applied Physics Letters, 2006. **88**: p. 064101.

[33]. Chandrashekhar, M., et al., Demonstration of a 4H SiC betavoltaic cell. Applied Physics Letters, 2006. **88**: p. 033506.

[34]. L. C. Olsen, P. Cabauy, and B. J. Elkind, Phys. Today, 65, 35 (2012).

[35]. W. Sun, N. P. Kherani, K. D. Hirschman, L. L. Gadeken, and P. M. J. A. M. Fauchet, Adv. Mater., 17, 1230 (2005).

[36]. T. Adams, S. Revankar, P. Cabauy, L. Olsen, B. Elkind, and J. Grant, “Status of betavoltaic power sources for nano and micro power applications.” 45th Power Sources Conference (2012).

[37]. C. Thomas, S. Portnoff, and M.G. Spencer, Appl. Phys. Lett. 108, 1 (2016).

[38]. V.S. Bormashov, S.Y. Troschiev, S.A. Tarelkin, A.P. Volkov, D. V. Teteruk, A. V. Golovanov, M.S. Kuznetsov, N. V. Kornilov, S.A. Terentiev, and V.D. Blank, Diam. Relat. Mater. 84, 41 (2018).

[39]. V. Bormashov, S. Troschiev, A. Volkov, S. Tarelkin, E. Korostylev, A. Golovanov, M. Kuznetsov, D. Teteruk, N. Kornilov, S. Terentiev, S. Buga, and V. Blank, Phys. Status Solidi Appl. Mater. Sci. 212, 2539 (2015).

[40]. M. Lu, G.-g. Zhang, K. Fu, G.-h. Yu, D. Su, and J.-f. Hu, "Gallium Nitride Schottky betavoltaic nuclear batteries," Energy Conversion and Management, vol. 52, pp. 1955- 1958, 2011

[41]. Z. Cheng, H. San, Y. Li, and X. Chen, "The design optimization for GaN-based betavoltaic microbattery," in Nano/Micro Engineered and Molecular Systems (NEMS), 2010 5th IEEE International Conference on, 2010, pp. 582-586. [57] Z. Cheng, H. San, Z. Feng, B. Liu, and X.

[42]. Z. Cheng, Z. Zhao, H. San, and X. Chen, "Demonstration of a GaN betavoltaic microbattery," in Nano/Micro Engineered and Molecular Systems (NEMS), 2011 IEEE International Conference on, 2011, pp. 1036-1039

[43]. Chen, "High open-circuit voltage betavoltaic cell based on GaN pin homojunction," Electronics letters, vol. 47, pp. 720-722, 2011

[44].W. Ray, M. Litz, and J. Russo, US Army Res. Lab ARL-TR-767, (2016).

[45]. W. Ray, M. Litz, J. Russo, and S. Bayne, ARL-TR, 731 (2017).

[46]. M. Litz, ARL-TR-708, (2014).

[47]. Z. Cheng, H. San, Y. Li, and X. Chen, 2010 IEEE 5th Int. Conf. Nano/Micro Eng. Mol. Syst. NEMS 2010 2, 582 (2010).

[48]. Kim, D.-S., Yoon, Y. J., Lee, J. S., Kang, I. M., & Lee, J.-H. (2021). Experimental and simulation study of power performance improvement of gan pin betavoltaic cell. *International Journal of Energy Research*, *45*(12), 17622–17630. https://doi.org/10.1002/er.7011

[49]. Munson CE, Arif M, Streque J, et al. Model of Ni-63 batteri with realistic PIN structure. J Appl Phys. 2015;118:105101.

[50]. Grazanka S, Marona L, Wisniewski P, et al. Highly stable GaNbased betavoltaic structures grown on differenct dislocation density substrates. Solid State Electron. 2020;167:107784.

[51]. Maximenko, S.I., Moore, J.E., Affouda, C.A. *et al.* Optimal Semiconductors for ^{3}H and ^{63}Ni Betavoltaics. *Sci Rep* **9,** 10892 (2019). https://doi.org/10.1038/s41598-019-47371-6

[52]. Kim, D.-S., Yoon, Y. J., Lee, J. S., Kang, I. M., & Lee, J.-H. (2021). Experimental and simulation study of power performance improvement of gan pin betavoltaic cell. *International Journal of Energy Research*, *45*(12), 17622–17630.

[53]. Jaydeep Sarkar, Sputtering Materials for VLSI and Thin Film Devices, William Andrew Publishing, 2014, Pages 1-92, ISBN 9780815515937,

[54]. https://www.pveducation.org/pvcdrom/pn-junctions/semiconductor-materials

[55].https://www.halbleiter.org/en/fundamentals/doping/#:~:text=1.,electrons%20%3D%205%2Dvalent).

[56]. Lutz, Josef. "Pin-Diodes." Semiconductor Power Devices: Physics, Characteristics, Reliability. Berlin: Springer, 2011. 159-66. Print.

[57]. Michael Shur, Physics of Semiconductor Devices, Prentice Hall (1990)

[58]. Neamen, Donald A. "The Pn Junction." Semiconductor Physics and Devices: Basic Principles. Boston: McGraw-Hill, 2003. 241-96. Print.

[59]. Belahsene, S.; Al Saqri, N.A.; Jameel, D.; Mesli, A.; Martinez, A.; De Sanoit, J.; Ougazzaden, A.; Salvestrini, J.P.; Ramdane, A.; Henini, M. Analysis of Deep Level Defects in GaN p-i-n Diodes after Beta Particle Irradiation. *Electronics* **2015**, *4*, 1090-1100. https://doi.org/10.3390/electronics4041090

[60]. C. A. Klein, "Bandgap dependence and related features of radiation ionization energies in semiconductors," Journal of Applied Physics, vol. 39, pp. 2029-2038, 1968.

[61]. H. San, S. Yao, X. Wang, Z. Cheng, and X. Chen, "Design and Simulation of GaN based Schottky Betavoltaic Nuclear Micro-battery," Applied Radiation and Isotopes, 2013.

[62]. M. Chandrashekhar, C. I. Thomas, H. Li, M. G. Spencer, and A. Lal, "Demonstration of a 4H SiC betavoltaic cell," Applied physics letters, vol. 88, pp. 033506-033506-3, 2006.

[63]. Kosteski, T., et al. Tritiated amorphous silicon betavoltaic devices. 2003: IET.

[64]. Blanchard, J., D. Henderson, and A. Lal, Nuclear Microbattery for MEMS Devices. U S. Deportment of Energy Award No. DEFG07-99ID13781. University of Wisconsin-Madison. Madison, WI. **53706**.

[65]. https://www.nndc.bnl.gov/nudat3/

[66]. D.-Y. Qiao, X.-J. Chen, Y. Ren, and W.-Z. Yuan, "A Micro Nuclear Battery Based on SiC Schottky Barrier Diode," Microelectromechanical Systems, Journal of, vol. 20, pp. 685- 690, 2011.

[67]. D.-Y. Qiao, Y. Wei-Zheng, G. Peng, Y. Xian-Wang, Z. Bo, Z. Lin, et al., "Demonstration of a 4H SiC betavoltaic nuclear battery based on Schottky barrier diode," Chinese Physics Letters, vol. 25, p. 3798, 2008.

[68]. https://www.nrc.gov/reading-rm/doc-collections/cfr/part071/part071-appa.html

[69]. Pelowitz D. MCNPX user's manual, 2nd ed. Los Alamos: Los Alamos National Labortory, 2011.

[70]. Billington E, Ehrengerg W. The electron voltaic effects in silicon and selenium elements. Proc Phys Soc. 1961;78(5):845–853.

[71] M. Wu, S. Wang, Y. Ou, and W. Wang, “Optimization design of betavoltaic battery based on titanium tritide and silicon using Monte Carlo code,” Appl. Radiat. Isot. 142, 22–27 (2018).

[72]. Synopsys Sentaurus, Device User Guid. 2009.

[73]. Arora, A., Jain, A. *et al.* Impact of growth conditions on intrinsic carbon doping in GaN layers and its effect on blue and yellow luminescence. *J Mater Sci: Mater Electron* **31,** 14336–14344 (2020). https://doi.org/10.1007/s10854-020-03993-5.

[74]. Kumakura, K. *et al.* (2005) “Minority carrier diffusion length in gan: Dislocation density and doping concentration dependence,” *Applied Physics Letters*, 86(5), p. 052105. Available at: https://doi.org/10.1063/1.1861116.

[75]. Arteev, D.S. *et al.* (2021) “Determination of hole diffusion length in n-Gan,” *Journal of Physics: Conference Series*, 2086(1), p. 012075. Available at: https://doi.org/10.1088/1742-6596/2086/1/012075.

[76]. Jing Wang, Xiaodan Wang, Jiafan Chen, Xiaodong Gao, Xionghui Zeng, Hongmin Mao, Ke Xu, Investigation on minority carrier lifetime, diffusion length and recombination mechanism of Mg-doped GaN grown by MOCVD, Journal of Alloys and Compounds, Volume 870, 2021, 159477, ISSN 0925-8388,https://doi.org/10.1016/j.jallcom.2021.159477.

[77]. Boturchuk I, Walter T, Julsgaard B et al. 2019 Structure and properties of Ta/Al/Ta and Ti/Al/Ti/Au multilayer metal stacks formed as ohmic contacts on n-GaN Journal of Material Science: Materials in Electronics vol 30 p 18144 https://doi.org/10.1007/s10854- 019-02167-

[78]. S. Figge, R. Kroeger, T. Boettcher, P. Ryder, D. Hommel, Appl. Phys. Lett. 2002, 81, 4748.

[79]. L. Romano, M. Kneissl, J. Northrup, C. V. de Walle, D. Treat , Appl. Phys. Lett. 1997, 79, 2734.

[80]. R. J. Nemanich, M.C Benjamin, S.W. King, M. D. Bremser, R.F. Davis, B. Chen, Z. Zhang, J.Bernholc, Mater. Res. Soc. Symp. Proc. 1996 , 395.

[81]. D. K. Schroder, "Contact Resistance and Schottky Barriers," in Semiconductor Material and Device Characterizationed: John Wiley & Sons, Inc., 2005, pp. 127- 184.

[82] J.-K. Ho, C.-S. Jong, C. C. Chiu, C.-N. Huang, K.-K. Shih, L.-C. Chen, F.-R. Chen, and J.-J. Kai, "Low-resistance ohmic contacts to p-type GaN achieved by the oxidation of Ni/Au films," Journal of Applied Physics, vol. 86, pp. 4491-4497, 1999.

[83]. Z. Fan, S. N. Mohammad, W. Kim, Ö. Aktas, A. E. Botchkarev, and H. Morkoç, "Very low resistance multilayer Ohmic contact to n-GaN," Applied Physics Letters, vol. 68, pp. 1672-1674, 1996.

[84]. D.-F. Wang, F. Shiwei, C. Lu, A. Motayed, M. Jah, S. N. Mohammad, K. A. Jones, and L. Salamanca-Riba, "Low-resistance Ti/Al/Ti/Au multilayer ohmic contact to n-GaN," Journal of Applied Physics, vol. 89, pp. 6214-6217, 2001.

[85] J. O. Song, H. Jun-Seok, and T.-Y. Seong, "Ohmic-Contact Technology for GaNBased Light-Emitting Diodes: Role of P-Type Contact," Electron Devices, IEEE Transactions on, vol. 57, pp. 42-59, 2010.

[86] Y. Koide, T. Maeda, T. Kawakami, S. Fujita, T. Uemura, N. Shibata, and M. Murakami, "Effects of annealing in an oxygen ambient on electrical properties of ohmic contacts to p-type GaN," Journal of Electronic Materials, vol. 28, pp. 341- 346, 1999.

[87] D. Mistele, F. Fedler, H. Klausing, T. Rotter, J. Stemmer, O. K. Semchinova, and J. Aderhold, "Investigation of Ni/Au-contacts on p-GaN annealed in different atmospheres," Journal of Crystal Growth, vol. 230, pp. 564-568, 2001.

[88]. Y. Dai, H. Kum, M. A. Slocum, G. T. Nelson and S. M. Hubbard, "High efficiency single-junction InGaP photovoltaic devices under low intensity light illumination," 2017 IEEE 44th Photovoltaic Specialist Conference (PVSC), 2017, pp. 222-225, doi: 10.1109/PVSC.2017.8366547.

[89]. Rybicki, G., Vargas-Aburto, C., and Uribe, R. M., “Silicon carbide alphavoltaic battery,” in Conference Records of the 25th IEEE Photovoltaics Special Conference (1996)

[90]. Oh, K., Prelas, M.A., Lukosi, E.D., Rothenberger, J.B., Schott, R.J., Weaver, C.L., Montenegro, D.E. and Wisniewski, D.A., 2012. Theoretical maximum efficiency for a linearly graded alphavoltaic nuclear battery. Nuclear technology, 179(2), pp.243-249.

[91]. S. G. Bailey, D. M. Wilt, S. L. Castro, C. D. Cress and R. P. Raffaelle, "Photovoltaic development for alpha voltaic batteries," Conference Record of the Thirty-first IEEE Photovoltaic Specialists Conference, 2005., 2005, pp. 106-109, doi: 10.1109/PVSC.2005.1488080.

[92] Sychov, M., Kavetsky, A., Yakubova, G., Walter, G., Yousaf, S., Lin, Q., Chan, D., Socarras, H. and Bower, K., 2008. Alpha indirect conversion radioisotope power source. Applied Radiation and Isotopes, 66(2), pp.173-177.

[93] Sha Xue, Chuting Tan, Praneeth Kandlakunta, Ibrahim Oksuz, Vasil Hlinka, Lei R. Cao, Methods for improving the power conversion efficiency of nuclear-voltaic batteries, Nuclear Instruments and Methods in Physics Research Section A: Accelerators, Spectrometers, Detectors and Associated Equipment, Volume 927, 2019, Pages 133-139

[94] Cory D. Cress, Brian J. Landi, and Ryne P. Raffaelle, David M. Wilt, InGaP alpha voltaic batteries: Synthesis, modeling, and radiation tolerance, J. APPL PHYS 100, 114519, 2006

[95]. J. Russo et al., “Low Light Illumination Study on Commercially Available Homojunction Photovoltaic Cells,” Applied Energy, Feb 2017.

[96]. Fedoseyev, A., Bald, T., Raman, A., Hubbard, S., Forbes, D., Freundlich, A., “Detailed physics based modeling of triple-junction InGaP/GaAs/Ge solar cell,” Proc. SPIE 8981, Physics, Simulation, and Photonic Engineering of PV Devices, 2014.

[97] J. Russo, M. Litz, W. Ray II, B. Smith, and R.Moyers, “A radioluminescent nuclear battery using volumetric configuration: 63Ni solution/ZnS: Cu,Al/InGaP,” Appl. Radiat. Isot., vol. 130, pp. 66–74, 2017.

[98]. J.B Talbot, E. Sluzky, and S.K. Kurinec, “Electrophoretic deposition of monochrome and color phosophor screens for information displayrs,” Journal of Materials Science, 39, 771 (2004).

[99]. L. Besra, “A review on fundamentals and applications of electrophoretic deposition (EPD),” Progress in Materials Science, 52, 1 (2007).

[100]. I. Corni, M. P. Ryan, and A.R. Boccaccian, “Electrophoretic deposition: From traditional ceramics to nanotechnology,” Journal of the European Ceramic Society, 28, 1353 (2008).